HHS Public Access

Author manuscript

Mol Cell. Author manuscript; available in PMC 2026 March 30.

Published in final edited form as:

Mol Cell. 2026 February 19; 86(4): 604–624.e16. doi:10.1016/j.molcel.2026.01.023.

Unbalanced chromatin binding of Polycomb complexes drives neurodevelopmental disorders

Rodrigo L. Borges[1,2,15], **Gretter González-Blanco**[1,2,15], **Harikumar Arigela**[1,2,15], **Yingyu Huang**[1,2], **Lucas D. Caeiro**[1,3], **Nikolai Fattakhov**[1,2], **Stefano Lepore**[1,4], **Liliana Garcia-Martinez**[1,2], **Matea Maurice**[5], **Pushti D. Mehta**[1,2], **Emily J. Park**[6], **Kailynn MacGillivray**[5], **Jevithen Nehru**[5], **Matthew Chau**[7,8], **Maria C. Robayo**[2,9], **Clemer Abad**[2,9], **Alicia Bilbao-Martinez**[1,4], **Fabiola Monteiro**[10], **Xi Luo**[7,8], **Song Tan**[11], **Daniel Bilbao**[1,4], **Simone Sidoli**[12], **Bruno Di Stefano**[6], **Katherina Walz**[2,9,13], **Arneet L. Saltzman**[6], **Ramiro E. Verdun**[1,3,14], **Ramin Shiekhattar**[1,2], **Lluis Morey**[1,2,16,*]

[1]Sylvester Comprehensive Cancer Center, Biomedical Research Building, 1501 NW 10th Avenue, Miami, FL 33136, USA

[2]Department of Human Genetics, University of Miami Miller School of Medicine, Miami, FL 33136, USA

[*]Correspondence: lmorey@med.miami.edu.

AUTHOR CONTRIBUTIONS

R.L.B. performed bioinformatic analyses. G.G.-B. conducted most of the experiments *in vitro*. H.A. generated the HA/FLAG-tagged cell lines and FLAG IPs in the laboratory of R.S. L.D.C. and L.G.-M. performed ATAC-seq and Cut&Run in the laboratories of R.E.V. and L.M. N.F., A.B.-M., and S.L. performed the mouse experiments with the supervision of D.B. and L.M. E.J.P. performed differentiation experiments in the laboratory of B.D.S. K.M., M.M., and J.N. performed experiments in *C. elegans* and AlphaFold modeling in the laboratory of A.L.S. M.C., X.L., and F.M. provided the *RNF2* and *RING1* mutations. Y.H. performed behavioral assays and performed 10× Multiome. P.D.M. performed trajectory analysis for 10× Multiome. M.C.R. and C.A. performed behavioral assays in the laboratory of K.W. S.T. modeled RING1A/B variants *in silico*. S.S. performed LC-MS/MS assays. L.M. coordinated and designed the experimental approach, coordinated the project, interpreted the data, and wrote the manuscript. All authors commented on the manuscript.

RESOURCE AVAILABILITY

Lead contact

Further information and requests for resources and reagents should be directed to and will be fulfilled by the lead contact, Lluis Morey (lmorey@miami.edu).

Materials availability

All plasmids and cell lines generated in this study are available upon reasonable request from the lead contact.

Data and code availability

- All raw and processed NSG data were deposited in the NCBI Gene Expression Omnibus under accession numbers GSE286287 (RNAseq), GSE286288 (ATAC-seq), GSE286289 (ChIP-seq), GSE286290 (Cut&Run), GSE286294 (scRNA-seq), and GSE312572 (10× multiome). Mass spectrophotometry raw files were deposited in the public repository ProteomeXchange with the project accession number PXD059191.
- This paper does not report original code.
- Any additional information required to reanalyze the data reported in this paper is available from the lead contact upon request.

DECLARATION OF INTERESTS

The authors declare no competing interests.

DECLARATION OF GENERATIVE AI AND AI-ASSISTED TECHNOLOGIES IN THE WRITING PROCESS

During the preparation of this work, the authors used ChatGPT in order to improve readability in portions of this manuscript. After using this tool/service, the authors reviewed and edited the content as needed and take full responsibility for the content of the publication.

[3]Division of Hematology, Department of Medicine, University of Miami Miller School of Medicine, Miami, FL 33136, USA

[4]Department of Pathology, University of Miami Miller School of Medicine, Miami, FL 33136, USA

[5]Department of Cell & Systems Biology, University of Toronto, Toronto, ON, Canada

[6]Stem Cells and Regenerative Medicine Center, Baylor College of Medicine, Department of Molecular and Cellular Biology Houston, Houston, TX 77030, USA

[7]Department of Molecular and Human Genetics, Baylor College of Medicine, Houston, TX 77030, USA

[8]Baylor Genetics, Houston, TX 77021, USA

[9]John P. Hussman Institute for Human Genomics, University of Miami Miller School of Medicine, Miami, FL 33136, USA

[10]Mendelics, São Paulo, Brazil

[11]Center for Eukaryotic Gene Regulation, Department of Biochemistry and Molecular Biology, The Pennsylvania State University, University Park, PA 16802, USA

[12]Department of Biochemistry, Albert Einstein College of Medicine, Bronx, NY 10461, USA

[13]Departamento de Ingeniería Biomédica, Facultad de Ingeniería, Universidad Austral, CONICET, Buenos Aires 1428, Argentina

[14]Geriatric Research, Education, and Clinical Center, Miami VA Healthcare System, Miami, FL 33136, USA

[15]These authors contributed equally

[16]Lead contact

SUMMARY

The prevalence of neurodevelopmental disorders (NDDs) in children is increasing, yet their underlying causes remain largely unknown. We identified heterozygous mutations in the Polycomb repressive complex 1 (PRC1) E3 ligases RING1 and RNF2 in individuals with NDDs and revealed distinct mechanisms by which they compromise PRC1 activity. We developed cellular and mouse models carrying the Ring1b^{R70H} variant, which disrupts PRC1/PRC2 recruitment balance and mis-regulates Polycomb target genes. Allele-specific profiling showed that Ring1b^{R70H} preferentially assembles into canonical PRC1 (cPRC1) via the intrinsically disordered region (IDR) of Pcgf2, reducing variant PRC1 (vPRC1) and PRC2.1 binding to chromatin. In *Rnf2*$^{WT/R70H}$ neuroprecursors, Polycomb complexes aberrantly suppress Wnt signaling, diverting neuroprecursors to non-neuronal lineages and halting neurogenesis. *Rnf2*$^{R70H/R70H}$ mice are perinatally lethal, while heterozygotes exhibit altered axonal organization, hippocampal and medial prefrontal cortex (mPFC) neuronal imbalances, reduced sociability, and increased anxiety. Our findings reveal an epigenetic mechanism essential for neurodevelopmental integrity and brain function and demonstrate how mutations in *Rnf2* disrupt PRC1 occupancy at chromatin, contributing to NDDs.

Graphical Abstract

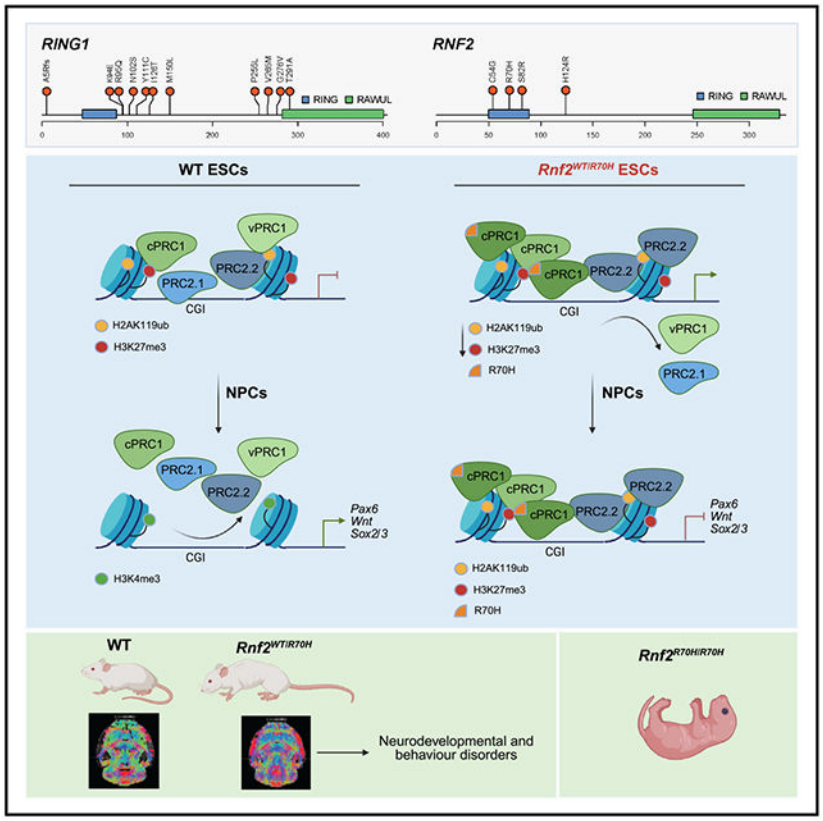

In brief

Borges, González-Blanco, Arigela, et al. report new missense mutations in the PRC1 genes *RNF2* and *RING1* in individuals with neurodevelopmental disorders. Functional dissection of a deleterious variant reveals that balanced co-recruitment of Polycomb complexes to chromatin is essential for proper neurogenesis and for normal brain function and behavior.

INTRODUCTION

Over the last decades, the number of children diagnosed with a developmental disability increased significantly. In the US, 1 in 6 children is affected by one or more developmental disabilities, including autism spectrum disorder and intellectual disability (ID) prevalence.[1-3] This growing population underscores the need to define the genetic mutations driving these conditions and their underlying etiology and pathogenesis to improve long-term outcomes. Multiple neurodevelopmental disorders (NDDs) are genetically linked to mutations in chromatin-modifying enzymes and epigenetic regulators,[4] including Polycomb-group (PcG) genes,[5] but how PcG mutations drive NDDs remains poorly understood.

Cell fate determination and maintenance are crucial biological processes that safeguard proper organismal development and preserve tissue homeostasis throughout adulthood.[6-8] PcG are epigenetic machineries that maintain gene repression to instruct cell fate decisions

and cell identity.[9] PcG are classified into two major complexes based on their enzymatic activities named Polycomb repressive complex 1 and 2 (PRC1 and PRC2).[10,11] PRC1 mono-ubiquitinates histone H2A at lysine 119 (H2AK119ub) via the E3 ligases RING1A and RING1B, which form six biochemically distinct subcomplexes, determined by the specific PCGF protein incorporated (PCGF1–6). These subcomplexes are further categorized into two groups: canonical PRC1 (cPRC1), which assembles with CBX proteins (CBX2, CBX4, and CBX6–CBX8), and variant PRC1 (vPRC1), which assembles with RYBP/YAF2, respectively.[12-14] PRC2 deposits methylation on lysine 27 on histone H3 (H3K27me1/2/3) by EZH1 and EZH2. PRC2 ancillary factors such as Jarid2 and PCL proteins further classify PRC2 into two subcomplexes, PRC2.2 and PRC2.1, respectively.[15-19] This diversity dictates their recruitment mechanisms to specific genetic loci and their roles in gene repression and activation,[20-23] highlighting the immense complexity of PcG in gene regulation.[24] The interplay, co-operation, and mutual regulation activity of these complexes in cell differentiation and in pathological contexts are still not well understood.

Population studies have identified recurrent heterozygous mutations in genes encoding PRC1 and PRC2 subunits in individuals with ID.[25-38] Thus, mutations in the Polycomb system lead to various developmental delays, including microcephaly, macrocephaly, autism, anxiety, mood disorders, and other conditions. Interestingly, while PRC2 mutations are associated with macrocephaly, mutations in PRC1 and PR-DUB[39-41] are linked to microcephaly, suggesting that the balance between H2AK119ub and H3K27me is a critical determinant of proper brain development and growth. However, how single-point mutations in Polycomb-encoding genes disrupt neurodevelopment in individuals with NDDs remains largely unknown.

RING1 (encodes for RING1A) has a higher tolerance to loss-of-function (LOF) variants compared with *RNF2* (encodes for RING1B). This is evidenced by a greater number of LOF variants observed in *RING1*, with a LOF observed/expected upper bound fraction (LOEUF) score of 0.41, compared with an LOEUF score of 0.32 for *RNF2* in healthy populations. Three *de novo* missense mutations in *RING1* and *RNF2* have been shown to be pathogenic and cause IDs. These include *RNF2* c.246T>G;p.S82R and c.209G>A;p.R70H, and *RING1* c.284G>A;p.R95Q.[28,33] In this study, we provide an extended catalog of missense mutations on *RING1* and *RNF2* found in individuals with NDDs. Our findings suggest that disruption of the precise balance of Polycomb complex recruitment to chromatin leads to profound impairments in cell differentiation, brain architecture, and function. Furthermore, we introduce a Polycomb mouse model to advance the study of cognitive impairment and anxiety disorders by epigenetic reprogramming.

RESULTS

RING1 and *RNF2* mutations reveal discrete PRC1 perturbations linked to neuropathologies

To broaden the spectrum of individuals with ID features carrying *de novo* missense mutations in *RNF2* or *RING1*, we interrogate several databases, including ClinVar, gnomAD, OMIM, lovd, decipher, denovo db, Deciphering Developmental Disorders (DDD), and COSMIC. We also analyzed genetic variants from individuals with ID from the Mendelics database and 105 individuals from the Baylor database. These efforts revealed

11 and 4 additional patients with missense mutations of interest on *RING1* and *RNF2*, respectively (Figure 1A; Table S1). While three *RNF2* variants are within the RING catalytic domain, the *RING1* variants are outside the RING domain, and one variant is at the RAWUL domain (Figure 1A). Although most variants are singlets, five of the *RING1* variants were found in patients carrying missense mutations in the vPRC1 genes *AUTS2* and *CSNK2B* and other chromatin-related factors such as *CHD7* and *MECP2* (Table S1), which are strongly linked to NDDs.[42-44] ClinVar revealed multiple variants of uncertain significance. Moreover, numerous uncharacterized variants identified in COSMIC warrant further investigation (Figure 1A).

To assess whether identified variants are likely disease-causing, we annotated REVEL (Rare Exome Variant Ensemble Learner) and CADD (Combined Annotation Dependent Depletion) scores to prioritize candidates for pathogenicity (Table S1). Variants in the RING domain or its surrounding regions are consistently predicted to have deleterious effects. Supporting this, protein tolerance for amino acid changes data revealed that these mutations in RING1A and RING1B are highly constrained (Figure 1A; Table S1). Using ColabFold and the crystal structure of the catalytic module of PRC1 (RING1B and PCGF4) and the E2-ligase UbcH5c bound to a nucleosome,[48] we predicted *in silico* whether the single variants could have an effect on PRC1 activity and architecture. Both K94E and R95Q mutations in RING1A were expected to disrupt its interaction with the histone H2A/B acidic patch, therefore averting PRC1 from depositing H2AK119ub (Figures S1A and S1B). RING1A^{N102A} and RING1B^{R70H} were predicted to disturb the interaction with PCGF proteins (Figures 1B, S1B, and S1C). C54G was predicted to disrupt the folding of RING1B, and S82R to alter the interaction with UbcH5C and the nucleosome (Figures S1A and S1D). To validate these predictions, we generated stable cell lines expressing either wild-type (WT) or RING1A and RING1B variants in RING1A/B double knockout (dKO) cells. Our results confirmed that the RING1A-K94E and R95Q variants are unable to monoubiquitinate histone H2A, likely due to impaired interaction with the nucleosome (Figure 1C). The RING1A^{N102S} variant partially affected PRC1 activity, as it was predicted to disrupt interactions with PCGFs (Figure S1B). Moreover, as anticipated, none of the RING1A variants impaired the assembly of PRC1 (Figure S2A). Regarding the RING1B variants, we confirmed the R70H variant strongly reduced PRC1 activity, C54G disrupted RING1B folding and stabilization, and S82R had only a minor effect on PRC1 activity (Figure 1C). The A73V variant partially affected RING1B activity through an unidentified reason (Figures 1C and S1E). Overall, we propose four distinct mechanisms by which these variants could interfere with PRC1 activity and structure (Figure 1D).

To evaluate whether RING1B point mutations have evolutionarily conserved effects in PRC1 activity, we identified the conserved R70 residue in the *C. elegans* RING1B homolog, SPAT-3 at R181 (Figure 1E). Structural modeling also suggests that SPAT-3-R181 contacts D384 in the PCGF homolog, MIG-32 (Figure S2B). We introduced the R181H point mutation into an HA-tagged allele of *spat-3* (Figure S2C). Histone H2AK119ub levels were reduced by ~40% in *spat-3[R181H]::3xHA* mutants (Figure 1F), indicating that R70H in mammals and R181 in worms are functionally conserved. To investigate the impact of *RING1* and *RNF2* missense mutations on neurodevelopment, we then focused on the pathogenic monoallelic R70H mutation in RING1B as a proof of concept. The R70H

mutation has high CADD and REVEL scores (Table S1) and is deleterious,[33] with a strong impact on PRC1 activity (Figure 1C). Moreover, RING1B^{R70H} binds to chromatin more efficiently than RING1B^{WT} (Figure 1G) and affects PRC2 activity (Figures 1H, S2D, and S2E).

Ring1b^{R70H} disrupts the balance of Polycomb complex co-occupancy, resulting in gene upregulation and accumulation of mut-cPRC1.2 at chromatin

We generated by homologous recombination two heterozygous mouse embryonic stem cell (ESC) lines carrying the R70H mutation (*Rnf2*$^{WT/R70H}$) (Figures 2A and S3A). *Rnf2*$^{WT/R70H}$ ESCs express normal levels of pluripotency factors and proliferate slightly faster than controls (Figures S3B-S3E). The levels of Ring1b and other PRC1 and PRC2 subunits remained unchanged in both mutant lines, and as anticipated, H2AK119ub levels were reduced (Figure S3E). Gene expression analyses in WT and *Rnf2*$^{WT/R70H}$ ESCs revealed upregulation of PcG target genes involved in neurogenesis and body pattern specification (Figures 2B, 2C, and S3F), indicating that a single-point mutation in one allele of *Rnf2* is sufficient to alleviate Polycomb-mediated gene repression.

Chromatin immunoprecipitation sequencing (ChIP-seq) shows that, despite enhanced chromatin recruitment of Ring1b in *Rnf2*$^{WT/R70H}$ ESCs, both H2AK119ub and H3K27me3 levels were reduced by ~50% (Figure 2D). To test whether Ring1b^{R70H} is more efficiently recruited to chromatin in ESCs, as in HEK293T cells (Figure 1E), we generated triple HA- and FLAG-tagged knockin (KI) by CRISPR-Cas9 in WT and *Rnf2*$^{WT/R70H}$ ESCs. FLAG and HA tags were knocked in on each of the *Rnf2* alleles from two WT and two *Rnf2*$^{WT/R70H}$ ESC clones. Therefore, we generated WT ESCs expressing endogenous *Rnf2* tagged with HA on one allele and with FLAG on the other allele (*Rnf2*$^{HA\text{-}WT/FLAG\text{-}WT}$) (Figures 2E and S3G). The same strategy was used to generate *Rnf2*$^{WT/R70H}$ ESCs expressing HA-Ring1b^{WT} and FLAG-Ring1b^{R70H} (*Rnf2*$^{HA\text{-}WT/FLAG\text{-}R70H}$) and vice versa (*Rnf2*$^{FLAG\text{-}WT/HA\text{-}R70H}$) to control for any tag-mediated effects (Figures 2E and S3G). To determine the specific occupancy of WT and Ring1b^{R70H}, we merged HA and FLAG Cut&Run biological replicates after determining that both tags were similarly efficient in Cut&Run (Figures S3H and S3I). Our results determine that the Ring1b^{R70H} is recruited to PcG target genes more efficiently than Ring1b^{WT} (Figure 2F). Additionally, H2AK119ub and H3K27me3 Cut&Run in the HA- and FLAG-edited cells further confirmed their reduction observed in the *Rnf2*$^{WT/R70H}$ cells (Figures 2D, S3J, and S3K).

Our HA/FLAG KI cell lines also allowed us to determine the interactome of endogenous Ring1b^{WT} and Ring1b^{R70H} in the *Rnf2*$^{WT/R70H}$ cells by mass spectrometry. R70H is predicted to disturb the interaction of Ring1b with Pcgf proteins (Figures S1A and S1C). We thus performed FLAG immunoprecipitation (IP) assays in *Rnf2*$^{HA\text{-}WT/FLAG\text{-}WT}$, *Rnf2*$^{HA\text{-}WT/FLAG\text{-}R70H}$, and *Rnf2*$^{FLAG\text{-}WT/HA\text{-}R70H}$ ESCs (Figure 2G). The interaction of multiple subunits associated to vPRC1 complexes, including Pcgf1/5/6,[14] was reduced in FLAG-Ring1b^{R70H}, while the interaction with Pcgf2, which associates with cPRC1,[12] was enhanced (Figures 2G and S3L). This suggests that vPRC1.1/5/6 occupancy containing Ring1b^{R70H} at chromatin is reduced, while cPRC1.2 containing Ring1b^{R70H} (mut-PRC1.2) is aberrantly recruited to chromatin in *Rnf2*$^{WT/R70H}$ ESCs. To test this, we performed ChIP-

seq of specific vPRC1, Rybp, and cPRC1.2 subunits Pcgf2 and Cbx7 in WT and *Rnf2*$^{WT/R70H}$ ESCs. These experiments confirmed that the mut-cPRC1.2 complex is aberrantly recruited to PcG target genes while vPRC1 complexes are evicted (Figures 2H and 2I). Additionally, in *Rnf2*$^{WT/R70H}$ ESCs, Mtf2 (PRC2.1) binding decreased while Jarid2 (PRC2.2) binding increased, indicating that the balance of PRC2 sub-complexes binding to chromatin is also altered (Figures 2H and 2I). Because vPRC1 and PRC2.1 are the major catalytically active PRC1/2 complexes in ESCs, their eviction from chromatin in *Rnf2*$^{WT/R70H}$ cells likely underlies the reduced H2AK119ub and H3K27me3 levels. We propose that Ring1b^{R70H} disrupts the balance of vPRC1, cPRC1, PRC2.1, and PRC2.2 occupancy, which alleviates the repressive function of Polycomb complexes.

We next sought to determine why Ring1b^{R70H} has a preference to associate with the cPRC1. We examined the Pcgf subunits, which contact Ring1a/b via the RING1 domain.[8] Mutabind2 analysis of AlphaFold and ColabFold models predicted that among the six human PCGF paralogs, PCGF2 (followed by PCGF4) has the strongest interaction with RING1B^{R70H}, reflected by the lowest ΔΔG score (lower = more stable). Because PCGF2, PCGF4, and PCGF6 contain intrinsically disordered regions (IDRs; Figures S3M and S3N), we asked whether the IDR contributes to the stabilization of Ring1b^{R70H} with these PCGFs. Indeed, *in silico* deletion of the IDR increased the ΔΔG score for PCGF2 and PCGF4, indicating weaker interactions. To confirm this *in vivo*, we focused on Pcgf2 because *Pcgf4* is not expressed in ESCs.[12] We generated WT and *Rnf2*$^{WT/R70H}$ ESCs expressing HA-Pcgf2^{WT} or HA-Pcgf2$^{\Delta IDR}$ and performed HA coimmunoprecipitations (coIPs). Only in mutant cells expressing HA-PCGF2$^{\Delta IDR}$ was the Ring1b interaction markedly reduced (Figure 2L), indicating that the enhanced cPRC1-Ring1b^{R70H} interaction depends on the IDR domain of Pcgf2 (Figure 2M).

Ring1b^{R70H} skews neural lineage choice via PRC1.2, suppressing neurogenesis

To investigate the impact of Ring1b^{R70H} in early neurogenesis, we performed RNA sequencing (RNA-seq) in WT and *Rnf2*$^{WT/R70H}$ ESCs, NPCs, and differentiated NPCs (Figure 3A).[49] NPCs derived from *Rnf2*$^{WT/R70H}$ ESCs showed a marked decrease in the expression of genes associated with axon guidance and neuronal development (Figure 3B, cluster 12), and differentiated *Rnf2*$^{WT/R70H}$ NPCs showed a profound downregulation of genes essential for the central nervous system, prefrontal cortex, and postsynaptic density (Figures 3B, clusters 1 and 7, and S4A). Notably, upregulated genes in the *Rnf2*$^{WT/R70H}$ differentiated NPCs were associated with postnatal growth retardation and abnormal brain morphology, features commonly observed in individuals with NDDs (Figure 3B, cluster 4). Through immunofluorescence (IF) studies, we confirmed the reduced neuronal differentiation capacity of *Rnf2*$^{WT/R70H}$ cells (Figure 3C).

We then asked how Ring1b^{R70H}-associated PRC1.2 and its abnormal chromatin occupancy affect differentiation of *Rnf2*$^{WT/R70H}$ ESCs into NPCs. Because Pcgf2 stabilizes PRC1.2,[21] we deleted *Pcgf2* by CRISPR-Cas9 in WT and *Rnf2*$^{WT/R70H}$ ESCs (Figure 3D). As expected from Pcgf2's role in mesoderm differentiation,[21] *Pcgf2* loss did not impair NPC generation from WT ESCs. By contrast, *Pcgf2* loss in *Rnf2*$^{WT/R70H}$ ESCs markedly reduced NPC

formation (Figure 3E), indicating that enhanced PRC1.2 recruitment by Ring1b^{R70H} acts as a compensatory mechanism to preserve NPC output.

Next, to delineate the specific structural role that Ring1b^{R70H} has in PRC1 architecture compared with the loss of Ring1b enzymatic activity and to assess whether Ring1a contributes to NPC differentiation defects in cells expressing Ring1b^{R70H}, we used Ring1A$^{-/-}$; Ring1B$^{fl/fl}$; Rosa26::CreERT2 ESCs[50] (PRC1^{cKO}), in which Ring1a is constitutively deleted and Ring1b is conditionally deleted with 4-hydroxy tamoxifen (OHT). PRC1^{cKO} cells were transfected to stably express HA-tagged Ring1B^{WT}, Ring1b^{R70H}, or the catalytic death mutant Ring1bI$^{53A/D56K}$[51] (Figures 3F and 3G). Upon OHT, only cells expressing Ring1b^{WT} differentiated into NPC. Neither the Ring1a/b dKO ESCs nor those expressing RING1b^{R70H} or RING1b$^{I53A/D56K}$ generated NPCs. They showed minimal Pax6 expression and reduced/absent H2AK119ub (Figures 3H and 3I). These results corroborated that both the enzymatic activity[51,52] and structure of PRC1 are key for cell differentiation.

NPCs can generate neurons and glia; therefore, we used single-cell RNA sequencing (scRNA-seq) to validate our bulk RNAseq and resolve all NPC-derived cell types. We confirmed that the neuronal population was significantly reduced in the differentiated *Rnf2*$^{WT/R70H}$ NPCs, while glial cells, including astrocytes, Schwann cells, and glial-like tanycytes, were enriched. Additionally, microglial cells were also enriched in the differentiated *Rnf2*$^{WT/R70H}$ NPCs (Figures 3J, 3K, S4B, and S4C). These results demonstrate that the Ring1b^{R70H} reduces the capacity of ESCs to produce functional NPCs, thereby hindering neural development while promoting differentiation into non-neuronal cells. The differentiation defect in *Rnf2*$^{WT/R70H}$ ESCs appears to be specific to the neuronal lineage, as primitive endoderm differentiation remains unaffected (Figure S4D).

Activation of Wnt signaling promotes proliferation and differentiation of NPCs into neurons,[53] while its inhibition can lead to the generation of glial cells.[54-56] We found that *Rnf2*$^{WT/R70H}$ NPCs exhibited a decrease in the Wnt signaling pathway activity (Figure 3L), suggesting that repression of Wnt may underlie the observed impaired neuronal differentiation. Because Wnt signaling is rapidly downregulated during NPC differentiation (Figure S4E), we tested whether transient Wnt activation could rescue neuronal defects. RT-qPCR showed no rescue of neuronal differentiation defects (Figure S4F), suggesting that *Rnf2*$^{WT/R70H}$ NPCs are irreversibly biased toward glial fates. Notably, the inflammation-linked non-obese diabetic (NOD)-like receptor pathway[57] is uniquely upregulated in mutant NPCs (Figure S4G), potentially contributing to microglia accumulation.

Overall, these results indicate that Ring1b^{R70H} leads to significant impairments in gene expression and pathways critical for neural development. Also, they highlight the consequences of *Rnf2* dysfunction in NDDs by providing insights into the molecular mechanisms underpinning these effects.

WT and mut-PcG complexes are retained at key neuronal genes in *Rnf2*$^{WT/R70H}$ NPCs to block neuronal differentiation and enhance glial differentiation

To investigate the mechanism preventing Wnt activation and promoting differentiation into non-neuronal cells in mutant NPCs, we utilized the HA and FLAG-tagged edited cell

lines and performed Cut&Run assays using anti-HA, FLAG, H2AK119ub, and H3K27me3 antibodies. These experiments enabled us to track PRC1 and PRC2 occupancy dynamics from ESCs to NPCs in an allele-specific manner. Analysis of genome-wide signal of Ring1b in WT and mutant NPCs revealed a significantly higher occupancy of total Ring1b in *Rnf2*$^{WT/R70H}$ NPCs (Figure 4A). Moreover, in contrast to the binding pattern of WT and mutant Ring1b in ESCs, we observed a lower binding to chromatin of Ring1b^{R70H} compared with Ring1b^{WT} in NPCs (Figures 4A and S5A). Importantly, the aberrant accumulation of Ring1b^{WT} can explain why H2AK119ub and H3K27me3 are elevated in mutant NPCs (Figures 4B and S5A). Furthermore, both WT and Ring1b^{R70H} were strongly associated with chromatin at sites where PRC1 binding is typically lost during ESC differentiation (Figures 4C and S5B). We next tested whether the Ring1b^{R70H}-PRC1 interactome was also altered in *Rnf2*$^{WT/R70H}$ NPCs. FLAG IP followed by liquid chromatography-tandem mass spectrometry (LC-MS/MS) showed that Ring1b^{R70H} again preferentially associates with cPRC1, with multiple vPRC1 components depleted from its interactome (Figures 4D, 4E, and S5C). The expression of PRC1 genes is dynamically regulated during differentiation[12] (Figure S5D), which is impaired in differentiated *Rnf2*$^{WT/R70H}$ NPCs (Figure S5D), indicating a loss of normal differentiation-dependent regulation of PRC1 expression. 1,356 genes upregulated in WT NPCs compared with ESCs were markedly silenced in mutant *Rnf2*$^{WT/R70H}$ NPCs by both WT and mut-PRC1 and PRC2 (Figures 4F-4I and S5E). KEGG and Gene Ontology (GO) analyses indicated that these genes were associated with axon guidance, the Wnt pathway, neuron projection, and autism, among other neuronal-related functions (Figures 4F, 4H, and 4I). Finally, chromatin accessibility by assay for transposase-accessible chromatin using sequencing (ATAC-seq) showed reduced accessibility at silenced genes that retain Polycomb occupancy in *Rnf2*$^{WT/R70H}$ NPCs, providing a mechanistic explanation for their repression (Figure 4J).

Aberrant Polycomb occupancy rewires the chromatin accessibility landscape in NPCs to favor glial differentiation

cPRC1 compacts chromatin and regulates 3D chromatin organization via the PHC subunit.[58,59] Since we found an aberrant accumulation of WT and mut-PRC1 complexes in *Rnf2*$^{WT/R70H}$ NPCs, we hypothesize a dual mechanism of repression of key neuronal genes mediated by both H2AK119ub/H3K27me3 and chromatin compaction. ATAC-seq identified thousands of ESC- and NPC-specific accessible sites in WT cells (Figures S6A and S6B). Principal-component analysis (PCA) indicated that Ring1b^{R70H} had no major effects on chromatin accessibility in ESCs but a profound effect in NPCs with a more general chromatin compaction (Figures 5A and S6C). For instance, we found strong chromatin compaction at key early neuronal differentiation and NPC-specific genes (e.g., *Pax6*, *Wnt*, *Nrp1*, and *Sox1*) (Figures 5B and S6D) concomitantly with their transcriptional silencing (Figures 5C and 5D). Differential ATAC-seq analyses also revealed discrete chromatin-accessible sites in WT and *Rnf2*$^{WT/R70H}$ NPCs. Thousands of ATAC peaks were either lost or aberrantly open in *Rnf2*$^{WT/R70H}$ NPCs. Transcription factor (TF) binding analysis at perversely closed chromatin regions in *Rnf2*$^{WT/R70H}$ NPCs revealed that these regions contain Sox2 and Sox3 binding sites (Figure 5E), are transcriptionally silenced (Figure 5F), and are critical in forebrain development, axonogenesis, and nervous system development (Figure S6E). By contrast, chromatin regions that are specifically open in *Rnf2*$^{WT/R70H}$

NPCs are decorated by AP-1 TF-binding sites, concomitantly expressed (Figures 5G and 5H), and associated with cell migration and inflammation (Figures S6F and S6G).

Sox2 is a key factor in pluripotent cells and NPCs, while Sox3 is silenced in stem cells but induced in NPCs to cooperate with Sox2 in driving NPC transcriptional programs.[60-64] Using publicly available Sox2 and Sox3 binding profiles in NPCs, we demonstrate that their binding sites are closed in *Rnf2*$^{WT/R70H}$ NPCs, resulting in the silencing of their target genes (Figure 5I). Notably, both Ring1b^{WT} and Ring1b^{R70H} bind to *Sox2* and *Sox3* promoters to repress their expression (Figures 5J and S6H), providing an explanation for the lack of activation of Sox2/3 targets. Finally, we collected genes whose promoters are inaccessible and contain WT and mutant Ring1b, along with PRC2, specifically in *Rnf2*$^{WT/R70H}$ NPCs, confirming their transcriptional silencing and involvement in neuron generation, organization, and projection (Figures 5K and S6I).

Homozygous *Rnf2*^{R70H} mice are perinatally lethal, and heterozygous mice display brain architectural deficits associated with NDDs

Rnf2 null mice exhibit embryonic lethality at E7.5 due to gastrulation arrest, underscoring the critical role of *Rnf2* in early development.[65] However, mice carrying the *Rnf2*$^{I53A/I53A}$ mutation, which results in ~80% reduction of H2AK119ub levels, survive until E15.5.[66] To elucidate the impact of the R70H variant in Ring1b on mouse development and neurodevelopment, we generated KI mice expressing either one (*Rnf2*$^{WT/R70H}$) or two (*Rnf2*$^{R70H/R70H}$) copies of the Ring1b^{R70H} allele. *Rnf2*$^{R70H/R70H}$ mice develop but succumb to perinatal lethality due to incomplete formation of the alveolar lumina, whereas *Rnf2*$^{WT/R70H}$ mice are viable and fertile. Neither the heterozygous nor homozygous mice display skeletal transformations (Figures 6A, 6B, and S8A-S8F). Heterozygous mice gain less weight across life than WT, in both sexes, with a stronger effect in males, suggesting a postnatal growth retardation and metabolic or hormonal defects with sex-specific modulation (Figure S8G).

Our *in vitro* data suggested defects in axon guidance, postsynaptic density, and brain morphology linked to NDDs (Figure 3), so we tested these *in vivo* by MRI tractography and brain-volume measurements in WT and *Rnf2*$^{WT/R70H}$ mice. Tractography uses diffusion MRI to model and visualize 3D nerve tracts, estimating axonal organization and long-range brain connectivity. We observed that differences in brain volume approached significance (Figure S8H). Notably, *Rnf2*$^{WT/R70H}$ brains show notable differences in the density, integrity, and orientation of neuronal tracts compared with the WT brain (Figure 6C; Table S2). This result indicates that the R70H mutation affects axonal organization. Moreover, we observed an increased number of axonal tracks projecting from the medial prefrontal cortex (mPFC), which is important for cognitive, emotional, and social functions[67] (Figures 6D and 6E; Videos S1 and S2; Table S2). Additionally, we found a reduction in the neuronal tracks projecting from the basolateral amygdalar nucleus, which plays a central role in integrating sensory information and modulating emotional responses[68] (Figures 6F and S8I; Videos S3 and S4; Table S2). These changes could reflect the impact of RING1B^{R70H} on human neurodevelopment and contribute to IDs and other neurological deficits, such as depression, impulsive behaviors, and abnormal social and emotional responses.

Individuals with PRC1 variants show severe learning/memory deficits and anxiety, implicating hippocampal dysfunction. We found a significant increase in the axonal interactions between the CA3 and dentate gyrus (DG) regions of the hippocampus (Figures 6G-6I; Videos S5 and S6; Table S3). Although this could signify enhanced hippocampal functionality for memory and learning, it has also been linked to anxiety.[69,70] Moreover, increased axonal interactions might indicate compensatory changes due to structural or functional deficits observed in the brain. Our *in vitro* results also indicate that generation of neurons is partially impaired in $Rnf2^{WT/R70H}$ NPCs. Thus, we interrogated the neuronal density in several regions in the brain and found increased and reduced numbers of neurons at the CA3c subregion of the hippocampus and suprapyramidal blade of the DG (spDG), respectively, in $Rnf2^{WT/R70H}$ mice compared with $Rnf2^{WT/WT}$ mice (Figures 6J and 6K). The combined effects of these changes could lead to imbalanced hippocampal processing, and disruption to this balance may underlie cognitive deficits or behavioral changes, such as impaired spatial memory, increased anxiety, or susceptibility to stress-related disorders. Finally, we observed a marked decrease in the neuronal density in the anterior cingulate cortex (ACC) of the mPFC (Figures 6L and 6M), which is associated with emotional processing.[71] In conclusion, our findings are in line with the impact of Polycomb mutations on human neurodevelopment and revealed the R70H impairs the hippocampal and mPFC development.

Ring1b^{R70H} aberrantly compacts chromatin and diverts developmental trajectories across the hippocampus and mPFC

We next performed single-nucleus RNA-seq (snRNA-seq) and ATAC-seq in WT and $Rnf2^{WT/R70H}$ hippocampus and mPFC to determine (1) whether defects in neurogenesis *in vitro* could be recapitulated in adult brains from $Rnf2^{WT/R70H}$ mice, and (2) to generate a comprehensive map of changes in chromatin accessibility at a single-cell level mediated by Ring1b^{R70H}. Uniform manifold approximation and projection (UMAP) analysis combining snRNA-seq and single-nucleus ATAC sequencing (snATAC-seq) data identified 17 cell clusters in both brain regions (Figures S8A-S8D). Single-nucleus trajectory analysis revealed genotype-specific lineage dynamics in both the hippocampus and mPFC (Figures 7A and 7B). In the hippocampus, WT cells progressed from progenitor/glial states toward late excitatory neuronal identities (pyramidal/VGlut2 and CA1-CA3 principals) (Figure 7A), whereas $Rnf2^{WT/R70H}$ cells showed a marked depletion of these terminal neuronal states and an expansion of glial lineages (astrocytes, oligodendrocytes, and microglia) (Figures 7B and 7C). Along pseudotime, mutant “immature granule cells (DGs)” persisted into later positions, indicative of delayed maturation, while astrocytes were overrepresented at earlier to mid positions, consistent with a gliogenic shift in the hippocampus (Figures 7B and 7C, left). In the mPFC, $Rnf2^{WT/R70H}$ similarly underrepresented late excitatory neurons, particularly deep-layer corticothalamic (CT) and extratelencephalic (ET) fates (L6 CT and L5 ET), with reciprocal enrichment of glial populations across the trajectory (Figures 7B and 7C, right). Together, these data demonstrate that Ring1b^{R70H} disrupts both *in vitro* (Figure 3) and *in vivo* normal neuronal differentiation and maturation, diverting trajectories toward glial and inflammatory lineages and causing persistence of immature neuronal states.

snATAC-seq indicates two principal findings: (1) widespread chromatin hyper-compaction across cell types in both hippocampus and mPFC and (2) cell-type-specific rewiring of TF programs in the *Rnf2*$^{WT/R70H}$ brain (Figures 7D, S8E, and S8F). Consistent with the *in vitro* transcriptional data in NPCs and differentiated neurons, snATAC-seq revealed recurrent enrichment of axon-guidance terms in both hippocampus and mPFC, indicating a shared connectivity defect (Figures 7E and 7F). The R70H allele also drives subtype-specific chromatin compaction. For instance, in the hippocampus, it preferentially closes regions controlling plasticity and synaptic programs in immature granule cells and signal-transduction pathways in CA2 neurons, in line with impaired circuit maturation. Immature granule cells also show strengthened repression at Polycomb targets, consistent with reinforced Polycomb-mediated silencing during aberrant maturation (Figure 7E). In the mPFC, repression is layer-selective—L5 ET neurons show closure across activity-dependent signaling and neuromodulatory pathways, whereas L6 CT neurons exhibit compaction of adhesion and axon-guidance modules—yet both layers converge on reduced accessibility at excitatory synaptic genes, pointing to weakened cortical output and CT development (Figure 7F). Analysis of the differential TFBS enriched and depleted in the hippocampus and mPFC in the mutant brains revealed a widespread reprogramming of the transcriptional circuits (Figures S8E and S8F). For instance, in CA2 principal neurons from *Rnf2*$^{WT/R70H}$, there was more accessibility of proneural basic helix-loop-helix (bHLH) motifs (Ascl1, Neurog2, NeuroD1, and Atoh1/7)[72] and bHLH motifs (SCL/Tal1 and MyoG/Twist2) that are important in other lineages, as well as Tcf4/12 and Tfe3 motifs, suggesting a worse functional state of these cells and weakening identity.

Impaired social novelty preference and increased anxiety-like behavior in *Rnf2*$^{WT/R70H}$ mice

Finally, we sought to determine whether the R70H variant produces neurobehavioral consequences. We performed a battery of behavioral assays to assess social interaction, anxiety-like behaviors, and learning and memory. In the sociability three-chamber assay, WT animals significantly interacted more with a novel mouse over a novel object, in contrast to *Rnf2*$^{WT/R70H}$ mice that do not display a significant preference for the novel mouse over the novel object (Figure 7G). Moreover, when testing for preference to social novelty, WT mice showed the expected significant social novelty preference, whereas *Rnf2*$^{WT/R70H}$ mice did not, indicating impaired recognition of a novel conspecific. Open-field testing revealed a reduced inner/outer zone ratio in *Rnf2*$^{WT/R70H}$ mice, consistent with increased anxiety-like behavior (Figures 7H and 7I). By contrast, spatial learning in the Barnes maze improved similarly across training days in both genotypes, and contextual and cued fear conditioning showed no genotype differences at short- or long-term retention (Figures S8G-S8I). Thus, the R70H allele affects sociability and the preference for social novelty and elevates anxiety-like behavior.

DISCUSSION

Despite growing evidence that missense mutations in PRC1 subunits contribute to NDDs, defining their mechanisms and impact on brain development has been difficult, largely due to a lack of suitable model systems. While our work focuses on *RING1* and *RNF2*

variants identified as singlets, we also uncovered variants that co-occur with mutations in other genes strongly associated with NDDs.[42-44,73] Notably, these co-mutated genes are epigenetic regulators, including two PcG genes (*AUTS2* and *CSNK2B*)[14] that co-mutate with *RING1*. To our knowledge, a potential digenic disorder involving two PcG genes has not been reported. This raises the intriguing question of whether *RING1* and *RNF2* variants have a synergistic effect in NDDs, leading to more severe cognitive and developmental phenotypes than mutations in either gene alone. Further investigation is warranted to explore this possibility.

Here, we provide evidence that variants in *RING1* and *RNF2* disrupt H2AK119ub through distinct molecular mechanisms, underscoring the fundamental importance of these amino acid changes in Polycomb biology and gene regulation. In ESCs, cPRC1 and multiple vPRC1 complexes bind developmental genes co-occupied by PRC2.1 and PRC2.2. Genetic deletion of Pcgf subunits or PRC2.1/PRC2.2 defining factors reveals an intricate, overlapping PcG network that ensures proper repression.[10] However, how deleterious variants alter PcG chromatin binding remains unexplored. By comprehensively analyzing the impact of the R70H variant in Ring1b, we have discovered a principle governing the maintenance of gene repression by Polycomb complexes. We provide evidence that disrupting the delicate balance of Polycomb complex occupancy leads to profound consequences in gene regulation and chromatin organization, neurodevelopment, and brain architecture.

Mechanistically, Ring1b^{R70H} associates with the IDR of Pcgf2, weakening interactions with vPRC1 Pcgf proteins. This shifts recruitment toward cPRC1 while reducing vPRC1 recruitment and activity. Reduced H3K27me3 coincides with PRC2.1 eviction and increased PRC2.2. Together, these data suggest (1) H2AK119ub is decremental of full cPRC1 binding to chromatin[74] in disease variants, (2) cPRC1 recruitment involves mechanisms beyond H3K27me3, and (3) PRC2.2 recruitment involves mechanisms beyond H2AK119ub. Consistent with this, Jarid2 promotes Cbx7 recruitment despite only modest effects on H3K27me3,[75] and Jarid2 recruitment increases in *Rnf2*$^{WT/R70H}$ cells even as H2AK119ub decreases. Why Ring1b^{R70H} shows diminished interaction with vPRC1 Pcgfs remains unclear but may reflect altered mutant PRC1 structure on chromatin that disrupts Rybp-Ring1b interactions and lowers H2AK119ub. Supporting this, recent crystal structures of vPRC1 bound to nucleosomes revealed a role for Rybp in propagating H2AK119ub.[76] These findings align with our observation that Ring1b^{R70H} reduces H2AK119ub by impairing vPRC1 recruitment, highlighting a critical mechanism by which Polycomb variants disrupt gene regulation through unbalancing Polycomb complexes' interaction with chromatin.

Mutant and WT PcG complexes remain bound to chromatin during ESC differentiation, causing aberrant compaction and repression of neurodevelopmental regulators such as *Pax6*, *Sox2/3*, and *Wnt* genes. In NPCs, Pax6 antagonizes Sox2/3 to promote differentiation, while Wnt signaling supports progenitor identity by boosting Sox2/3 expression[60,64,77,78]—an interconnected network disrupted in Ring1b^{R70H} NPCs. Our findings provide evidence that the R70H mutation in Ring1b disrupts neurodevelopmental processes *in vivo*, linking structural and functional brain deficits to behavioral and cognitive abnormalities. The perinatal lethality of homozygous *Rnf2*^{R70H} mice highlights the critical developmental

role of the R70 residue, while the viability of heterozygous *Rnf2*$^{WT/R70H}$ mice aligns with observations of heterozygosity in human cases with Polycomb missense mutations. The observed architectural brain deficits, including altered axonal tract organization, strongly indicate that Polycomb proteins are key regulators of axon guidance and synaptic organization. Notably, the increase in axonal interactions between the CA3 and DG regions in the hippocampus mirrors patterns described in models of anxiety. Furthermore, the reduced ACC neuronal density and altered hippocampal neuronal balance likely underlie emotional and cognitive dysregulation, consistent with Polycomb-mutant phenotypes affecting memory, social behavior, and emotional responses.

Single-nuclei trajectory analyses indicate that Ring1b^{R70H} diverts developmental trajectories away from late excitatory neuronal identities toward glial and inflammatory lineages in both the hippocampus and mPFC, with persistent immature granule cell states and underrepresentation of deep-layer CT/ET neurons. This aligns with the established role of Polycomb complexes in gating neurogenic vs. gliogenic competence and in timing neuronal maturation.[5] Maturation delays of granule cells are well-known to disrupt dentate gating and hippocampal circuit integration[79]; therefore, our results position a PRC1 variant as a driver of such delayed transitions.

These results build on evidence that PRC1 is essential for neurogenesis[80-82] and show that a single-point mutation on a PRC1 gene can selectively disrupt axonal connectivity, transcriptional circuits, and lineage decisions in key brain regions. By positioning *Rnf2* and *Ring1* mutations within established NDD frameworks, our study advances mechanistic understanding of ID and underscores how precise control of repressive histone marks is indispensable for normal development, cognition, and a healthy life.

Limitations of the study

In this manuscript, we propose that missense mutations in RING1A and RING1B affect PRC1 activity and structural changes by at least four mechanisms. Our comprehensive analysis of the R70H variant indicates that the recruitment of Polycomb complexes is altered. Whether this is a general mechanism by other variants needs to be addressed. Mechanistically, it remains to be determined what the factors and mechanisms are involved in the retention of Polycomb complexes in mutant NPCs.

STAR★METHODS

EXPERIMENTAL MODEL AND STUDY PARTICIPANT DETAILS

Cell lines: HEK293T dKO RING1A/B cells were a gift from Dr. Moazed.[96] Ring1A$^{-/-}$; Ring1B$^{fl/fl}$; Rosa26::CreERT2 cells were a gift from Dr. Koseki. Cells were cultured in Dulbecco's modified Eagle's medium with 10% fetal bovine serum (FBS, BenchMark 100-106) and supplemented with 1x Penicillin/Streptomycin (10,000 U/ml, Thermo Fisher Scientific 15140-122). Wild-type, two *Rnf2*$^{WT/R70H}$ HF4 clones and Ring1A$^{-/-}$; Ring1B$^{fl/fl}$; Rosa26::CreERT2 ESCs were expanded in feeder-free culture on plates coated with 0.1% gelatin (Millipore, ES-006-B) and 2i/LIF culture medium. Coating was completed by incubating plates with gelatin at 37°C for at least 10 min. 2i/LIF medium: DMEM high

glucose supplemented with GlutaMAX (Gibco), 15% fetal bovine serum (FBS), 1:100 leukemia inhibitory factor (LIF, 10^3 U/ml), 0.5 mM β-mercaptoethanol, glutamax, MEM non-essential amino acids, penicillin-streptomycin, and 2i inhibitors (1 μM PD0325901 and 3 μM CHIR99021). Cells were maintained in an incubator at 37°C with 5% CO2 and passaged every 2–3 days using trypsin-EDTA.

Generation of heterozygous mouse ESCs carrying the R70H mutation (Rnf2$^{WT/R70H}$): ESC-*Rnf2*$^{WT/R70H}$ were generated by Ingenious Targeting Laboratory using standard homologous recombination techniques, under a fee-for-service contract. Targeting Vector Design and Construction: A 9 kb genomic region encompassing the *Rnf2* gene was subcloned from a positively identified C57BL/6 BAC clone (RP23-41F24) using homologous recombination-based techniques. The targeting vector was designed to introduce the *Rnf2*^{R70H} mutation into exon 4. A targeting vector with wild-type exon 4 (*Rnf2*^{WT}) was used as control. An FRT-flanked neomycin selection marker (Neo) was inserted upstream of exon 4 within intron 3-4. The vector design included a 2.4 kb 5′ short homology arm (SA) and a 6.1 kb 3′ long homology arm (LA). To ensure accuracy, the targeting vector was validated at each step using restriction analysis and sequencing. Mutation-specific primer RRNF SQ1 was used to confirm the R70H mutation, and the FRT sequences flanking the Neo cassette were verified using primers iNeoN2 and IVNeoN3. Sequencing primers SEQ5′ and SEQ3′ were used to confirm the homology boundaries. The BAC subclone was inserted into an iTL cloning vector (~3 kb), derived from a pBR322 backbone with an ampicillin selection cassette for transformation. The final targeting construct, including the vector backbone (~15 kb), was linearized with AscI prior to electroporation.

Electroporation and ESC Selection: The linearized targeting construct (10 μg) was electroporated into FLP 129/SvEv x C57BL/6 hybrid embryonic stem cells (HF4). Transfected cells were selected using G418 antibiotic. Clones surviving selection were expanded and screened using PCR with the following primers: qA1 (5′ - GAG GTC TCT CTG GTC TGC TCT AGC –3′); RNEOGT: (5′ - GAA AGT ATA GGA ACT TCG CGA CAC GGA C –3′); NEOGT: (5′ - GTC CGT GTC GCG AAG TTC CTA TAC TTT C –3′); SQ1: (5′ - GAC AGG TAG GAC ACT CTT TGT TGC –3′); SC1: (5′ - TGA ACA TGG CGA CTT GGG TG –3′). The qA1 primer was located upstream of the SA, outside the 5′ targeting region. PCR reactions using qA1 and RNEOGT amplified a 2.58 kb fragment, identifying positive clones. Positive clones were further expanded, reconfirmed for SA integration, and the Neo cassette was excised during clone expansion. Control ESCs carrying a WT copy of exon 4 of *Rnf2* were generated in parallel as controls. These ESCs underwent the same homologous recombination procedures as the mutant ESCs, except that the *Rnf2*^{R70H} mutation was not introduced.

Generation of Rnf2$^{WT/R70H}$ knock-in mice: Blastocyst Injection and Chimera Generation: Recombinant HF4 ESCs were microinjected into CD-1 blastocysts. Resulting blastocysts were implanted into pseudo pregnant CD-1 females. Chimeric mice were identified based on coat color, and high-percentage agouti chimeras were bred with C57BL/6N wild-type (WT) mice to produce germline-transmitted offspring.

Genotyping and Identification of F1 Heterozygous Mice: Tail DNA was extracted from F1 offspring with agouti or black coat color. PCR analysis was performed using primers RNEOGT (inside the Neo cassette) and qA1 (upstream of the SA) to amplify a 2.58 kb fragment, confirming the presence of the targeted allele. Wild-type DNA and a no-template PCR reaction served as negative controls, while DNA from an initial positive clone served as a positive control.

Establishing the Transgenic Mouse Line: F1 heterozygous mice carrying the *Rnf2*^{R70H} mutation were intercrossed or backcrossed with C57BL/6N WT mice to establish the mutant line. Neo-deleted mutant lines were confirmed through additional PCR screening and Sanger sequencing. Transgenic mice were maintained on a mixed 129/SvEv x C57BL/6 genetic background.

All procedures involving experimental procedures with mice were approved by the Institutional Animal Care and Use Committees (protocol number 20-170 LF). Newborn and up to 4 month-old male and female mice were used.

C. elegans growth and genome editing: Strains were maintained on nematode growth medium (NGM) agar with *E. coli* OP50-1 as a food source as described[97] at 21°C. The N2 (Bristol) strain was used as wild-type.[98] To obtain synchronized populations of gravid adults, embryos were isolated by standard alkaline hypochlorite treatment, allowed to develop without food to arrest at L1 diapause, and then grown in the presence of food for 70–76 hours.[97] The SPAT-3::3xHA strain was generated by CRISPR essentially as described.[99,100] Templates for single guide RNAs (sgRNAs) were generated by PCR amplification and *in vitro*-transcribed using the HiScribe T7 Quick High Yield RNA Synthesis Kit (NEB). The repair template included the homology arms, selection cassette flanked by loxP sites within a synthetic intron, exon 19 of *spat-3*, and the AID, Bio and 3xHA tags. The SPAT-3-R181H mutation was introduced into the SPAT-3::3xHA strain by Co-CRISPR essentially as described[101] with the following modifications. The sgRNAs were prepared as described above and the injection mix was as follows: 0.25 μg/uL Alt-R S.p. Cas9 Nuclease V3 (ID Technology), 50 ng/µL sgRNAs,13.75 ng/µL *dpy-10* single-stranded DNA repair template, 110 ng/µL SPAT-3-R181H single-stranded DNA repair template, 25 mM KCl, and 7.5 mM HEPES-NaOH pH 7.4. Alleles were verified by Sanger sequencing.

METHOD DETAILS

Variants landscape Plots: Variants that were ever confirmed somatic in COSMIC database (https://cancer.sanger.ac.uk/cosmic) and SNVs in clinvar (https://www.ncbi.nlm.nih.gov/clinvar/) were downloaded from the user interface and loaded into R (v4.4.0) along with the mutations from Mendelics and plots created with loliplot in TrackViewer package (https://doi.org/10.18129/B9.bioc.trackViewer). Protein mutation tolerance images were downloaded from Metadome (https://doi.org/10.1002/humu.23798).

Characterization of Rnf2$^{WT/R70H}$ mice: A full necropsy was performed in adult male and female *Rnf2*$^{WT/R70H}$ mice with no significant morphological findings on H&E stained tissue examination by a veterinary pathologist.

Generation of C-terminus HA and Flag-tagged *Rnf2* in WT and *Rnf2*$^{WT/R70H}$ ESCs: WT and *Rnf2*$^{WT/R70H}$ ESCs were co-transfected with PX458-Rnf2-sgRNA (ACTTTATTATGCACCCACCA), along with FLAG and HA homologous recombination vectors (pBluescript II-3X FLAG-EGFP and pBluescript II-3X HA-Puromycin). After 48hrs cells were double sorted for the expression of GFP and selected with puromycin. Individual colonies were screened with specific RT-PCR primers (Rnf2-FWD: CTGTGCAGACAAATGGAACT; Puro-RVS: GCGCGCTCGGCCGCCTCCAC; EGFP-RVS: TCGTCCATGCCGAGAGTGATC), followed by Sanger sequencing of PCR products, to confirm the allele specific insertion of HA or FLAG tags at the C-terminus of *Rnf2*. Genotypes: *Rnf2*$^{HA\text{-}WT/FLAG\text{-}WT}$, *Rnf2*$^{HA\text{-}WT/FLAG\text{-}R70H}$ and *Rnf2*$^{HA\text{-}R70H/FLAG\text{-}WT}$. Two clones for each genotype were used for Cut&Run experiments in two biological duplicates.

Sanger Sequencing confirmation:

A. *Rnf2*$^{HA\text{-}WT/FLAG\text{-}WT}$ -Clone1_ WT allele1-3xHA/ WT allele2-3xFLAG

Rnf2$^{HA\text{-}WT/FLAG\text{-}WT}$ -clone 1: allele1-3xHA tag confirmation (in reverse orientation)

NNNNNNNGNNGNGNGCGTACGGCCCTGGGGNNGTCGTCGCGGGTGGCGAGGCG
CACCGTGGGCTTGTACTCGGTCATTCC
GCTTCCAGGTCCAGGGTTCTCCTCCACGTCTCCAGCCTGCTTCAGCAGGCTGAAG
TTAGTAGC**AGCGTAATCTGGAACATCGTA**
TGGGTAAGCGTAATCTGGAACATCGTATGGGTAAGCGTAATCTGGAACATCG
TATGGGTATGATCCGCCGCCACCCGACCCA
CCTCCGCCCGAGCCTCCGCCACCAGATTTGTGCTCTTTTGTTGGTGCATAATAAAG
TTCCATGGGTTTGTTCACTTTCCAGTATTTC
TCACTGACCAATTCCAAAGAAAAGGAGCCATTTAAAACCTAAAACAAAAAGAGG
CAAGATTATGAAAATGCATGGTGCTCAGTAAC
AGTGAGACTAAATAAACAAAAGGCCACAGGATCCCGTGCACAGCAGGAGAGATA
AAGGGCATCACGGAGTCATTAATCTGCGGC
TTTGCTTCGTGGGCCTCAGGGCTCCCCCCCTACCAGACCCACCCAGACCACTAGC
CAAGGAGCTCAACAGGCATTGACAAATAC
TCACGGTGAACTGGCCACTGGCTGTGGCTATGTAAATGGTGTACTGCTTCTCACTG
GCTGTATCCAGGTTCATCTGGTTTGATTCT
CCTTTGCTTCGAAGTTCTTCTAAAGCTAACCTCACAGCCAGATACTTGGATAAGTG
ATCAACAG

Rnf2$^{HA\text{-}WT/FLAG\text{-}WT}$ -clone 1: allele2-3xFLAG tag confirmation (in reverse orientation)

NNNNNNNNNCNCNCNCGCCGGACACGCTGAACTTGTGGCCGTTTACGTCGCCGT
CCAGCTCGACCAGGATGGGCACCACCC
CGGTGAACAGCTCCTCGCCCTTGCTCACCATTCCGCTTCCAGGTCCAGGGTTCTC
CTCCACGTCTCCAGCCTGCTTCAGCAGGC
TGAAGTTAGTAGC**CTTGTCATCGTCATCCTTGTAATCGATGTCATGATCTTTAT**
AATCACCGTCATGGTCTTTGTAGTCTGATCC
GCCGCCACCCGACCCACCTCCGCCCGAGCCTCCGCCACCAGATTTGTGCTCTTTT

GTTGGTGCATAATAAAGTTCCATGGGTTTG
TTCACTTTCCAGTATTTCTCACTGACCAATTCCAAAGAAAAGGAGCCATTTAAAAC
CTAAAACAAAAAGAGGCAAGATTATGAAAAT
GCATGGTGCTCAGTAACAGTGAGACTAAATAAACAAAAGGCCACAGGATCCCGTG
CACAGCAGGAGAGATAAAGGGCATCACGG
AGTCATTAATCTGCGGCTTTGCTTCGTGGGCCTCAGGGCTCCCCCCCCCCACCAN
ACCCAC

B. *Rnf2*$^{HA\text{-}WT/FLAG\text{-}WT}$ -Clone2_ WT allele1-3xHA/ WT allele2-3xFLAG

Rnf2$^{HA\text{-}WT/FLAG\text{-}WT}$ -clone 2: allele1-3xHA tag confirmation (in reverse orientation)

NNNNNNNNNNNNNNNGTGCGTACGGCCCTGGGGACGTCGTCGCGGGTGGCGA
GGCGCACCGTGGGCTTGTACTCGGTCA
TTCCGCTTCCAGGTCCAGGGTTCTCCTCCACGTCTCCAGCCTGCTTCAGCAGGCT
GAAGTTAGTAGC**AGCGTAATCTGGAACAT**
CGTATGGGTAAGCGTAATCTGGAACATCGTATGGGTAAGCGTAATCTGGAAC
ATCGTATGGGTATGATCCGCCGCCACCCGA
CCCACCTCCGCCCGAGCCTCCGCCACCAGATTTGTGCTCTTTTGTTGGTGCATAAT
AAAGTTCCATGGGTTTGTTCACTTTCCAGT
ATTTCTCACTGACCAATTCCAAAGAAAAGGAGCCATTTAAAACCTAAAACAAAAA
GAGGCAAGATTATGAAAATGCATGGTGCTCA
GTAACAGTGAGACTAAATAAACAAAAGGCCACAGGATCCCGTGCACAGCAGGAG
AGATAAAGGGCATCACGGAGTCATTAATCT
GCGGCTTTGCTTCGTGGGCCTCAGGGCTCCCCCCCCTACCAGACCCACCCAGACCA
CTAGCCAAGGAGCTCAACAGGCATTGAC
AAATACTCACGGTGAACTGGCCACTGGCTGTGGCTATGTAAATGGTGTACTGCTTC
TCACTGGCTGTATCCAGGTTCATCTGGTTT
GATTCTCCTTTGCTTCGAAGTTCTTCTAAAGCTAACCTCACAGCCAGATACTTGGA
TAAGTGATCAACAGTGGCATTGCCTGAA

Rnf2$^{HA\text{-}WT/FLAG\text{-}WT}$ -clone 2: allele2-3xFLAG tag confirmation (in reverse orientation)

GNNNNNNNNNNCNCGCCGGANNCGCTGAACTTGTGGCCGTTTACGTCGCCGTC
CAGCTCGACCAGGATGGGCACCACCCC
GGTGAACAGCTCCTCGCCCTTGCTCACCATTCCGCTTCCAGGTCCAGGGTTCTCC
TCCACGTCTCCAGCCTGCTTCAGCAGGCT
GAAGTTAGTAGC**CTTGTCATCGTCATCCTTGTAATCGATGTCATGATCTTTATA**
ATCACCGTCATGGTCTTTGTAGTCTGATCCG
CCGCCACCCGACCCACCTCCGCCCGAGCCTCCGCCACCAGATTTGTGCTCTTTTG
TTGGTGCATAATAAAGTTCCATGGGTTTGT
TCACTTTCCAGTATTTCTCACTGACCAATTCCAAAGAAAAGGAGCCATTTAAAACC
TAAAACAAAAAGAGGCAAGATTATGAAAATG
CATGGTGCTCAGTAACAGTGAGACTAAATAAACAAAAGGCCACAGGATCCCGTGC
ACAGCAGGAGAGATAAAGGGCATCACGGA
GTCATTAATCTGCGGCTTTGCTTCGTGGGCCTCAGGGCTCCCCCCCCTACCAGACCC

ACCCAGACCACTAGCCAAGGAGCTCAAC
AGGCATTGACAAATACTCACGGTGAACTGGCCACTGGCTGTGGCTATGTAAATGG
TGTACTGCTTCTCACTGGCTGTATCCAGGT
TCATCTGGTTTGATTCTCCTTTGCTTCGAAGTTCTTCTAAAGCTAACCTCACAGCC
AGATACTTGGATAAGTGATCAACAGTGGCAT
TGCCTGAAGTCTTTATGTATCTAAAAGAATAATG

C. Clone #1 Rnf2$^{WT/R70H}$ _Clone 1_ mutant allele1-3xHA/ WT allele2-3xFLAG

Clone #1 *Rnf2$^{WT/R70H}$ -clone 1: allele1-3xHA tag confirmation* (in reverse orientation)

NNNNNNNNNNNNNGGTGCGTACGGCCCTGGGGNCGTCGTCGCGGGTGGCGAG
GCGCACCGTGGGCTTGTACTCGGTCAT
TCCGCTTCCAGGTCCAGGGTTCTCCTCCACGTCTCCAGCCTGCTTCAGCAGGCTG
AAGTTAGTAGC**AGCGTAATCTGGAACATC**
GTATGGGTAAGCGTAATCTGGAACATCGTATGGGTAAGCGTAATCTGGAACAT
CGTATGGGTATGATCCGCCGCCACCCGAC
CCACCTCCGCCCGAGCCTCCGCCACCAGATTTGTGCTCTTTTGTTGGTGCATAATA
AAGTTCCATGGGTTTGTTCACTTTCCAGTA
TTTCTCACTGACCAATTCCAAAGAAAAGGAGCCATTTAAAACCTAAAACAAAAAG
AGGCAAGATTATGAAAATGCATGGTGCTCAGT
AACAGTGAGACTAAATAAACAAAAGGCCACAGGATCCCGTGCACAGCAGGAGAG
ATAAAGGGCATCACGGAGTCATTAATCTGCG
GCTTTGCTTCGTGGGCCTCAGGGCTCCCCCCCCCCACCACACCCACCCACACCAC
T

Clone #1 *Rnf2$^{WT/R70H}$ -clone 1: allele2-3xFLAG tag confirmation* (in reverse orientation)

NNNNNNNNNNNNCNCNNCTCGCCGGACACGCTGAACTTGTGGCCGTTTACGTCG
CCGTCCAGCTCGACCAGGATGGGCACC
ACCCCGGTGAACAGCTCCTCGCCCTTGCTCACCATTCCGCTTCCAGGTCCAGGGT
TCTCCTCCACGTCTCCAGCCTGCTTCAGC
AGGCTGAAGTTAGTAGC**CTTGTCATCGTCATCCTTGTAATCGATGTCATGATCT**
TTATAATCACCGTCATGGTCTTTGTAGTCTG
ATCCGCCGCCACCCGACCCACCTCCGCCCGAGCCTCCGCCACCAGATTTGTGCTC
TTTTGTTGGTGCATAATAAAGTTCCATGGG
TTTGTTCACTTTCCAGTATTTCTCACTGACCAATTCCAAAGAAAAGGAGCCATTTA
AAACCTAAAACAAAAAGAGGCAAGATTATGAA
AATGCATGGTGCTCAGTAACAGTGAGACTAAATAAACAAAAGGCCACAGGATCCC
GTGCACAGCAGGAGAGATAAAGGGCATCAC
GGAGTCATTAATCTGCGGCTTTGCTTCGTGGGCCTCAGGGCTCCCCCCCTACCAG
ACCCACCCAGACCACTAGCCAAGGAGCTC
AACAGGCATTGACAAATACTCACGGTGAACTGGCCACTGGCTGTGGCT

D. Clone #1 *Rnf2$^{WT/R70H}$* _Clone 2_ *mutant allele1-3xHA/ WT allele2-3xFLAG*

Clone #1 Rnf2$^{WT/R70H}$ -clone 2: mutant allele1-3xHA tag confirmation (in reverse orientation)

CNNNNNNNNNGNNNNNGCGTACGGCCCTGGGGACGTCGTCGCGGGTGGCGAGG
CGCACCGTGGGCTTGTACTCGGTCATT
CCGCTTCCAGGTCCAGGGTTCTCCTCCACGTCTCCAGCCTGCTTCAGCAGGCTGA
AGTTAGTAGC**AGCGTAATCTGGAACATCG**
TATGGGTAAGCGTAATCTGGAACATCGTATGGGTAAGCGTAATCTGGAACATC
GTATGGGTATGATCCGCCGCCACCCGACC
CACCTCCGCCCGAGCCTCCGCCACCAGATTTGTGCTCTTTTGTTGGTGCATAATAA
AGTTCCATGGGTTTGTTCACTTTCCAGTAT
TTCTCACTGACCAATTCCAAAGAAAAGGAGCCATTTAAAACCTAAAACAAAAAG
AGGCAAGATTATGAAAATGCATGGTGCTCAGTA
ACAGTGAGACTAAATAAACAAAAGGCCACAGGATCCCGTGCACAGCAGGAGAGA
TAAAGGG

Clone #1 Rnf2$^{WT/R70H}$ -clone 2: allele2-3xFLAG tag confirmation (in reverse orientation)

NNNNNNNNNNNNCNNNCCTCGCCGGACNCGCTGAACTTGTGGCCGTTTACGTCG
CCGTCCAGCTCGACCAGGATGGGCACC
ACCCCGGTGAACAGCTCCTCGCCCTTGCTCACCATTCCGCTTCCAGGTCCAGGGT
TCTCCTCCACGTCTCCAGCCTGCTTCAGC
AGGCTGAAGTTAGTAGC**CTTGTCATCGTCATCCTTGTAATCGATGTCATGATCT**
TTATAATCACCGTCATGGTCTTTGTAGTCTG
ATCCGCCGCCACCCGACCCACCTCCGCCCGAGCCTCCGCCACCAGATTTGTGCTC
TTTTGTTGGTGCATAATAAAGTTCCATGG
GTTTGTTCACTTTCCAGTATTTCTCACTGACCAATTCCAAAGAAAAGGAGCCATTT
AAAACCTAAAACAAAAAGAGGCAAGATTATG
AAAATGCATGGTGCTCAGTAACAGTGAGACTAAATAAACAAAAGGCCACAGGATC
CCGT

E. Clone #1 *Rnf2$^{WT/R70H}$* _Clone3_ *WT allele1-3xHA/ mutant allele2-3xFLAG*

Clone #1 *Rnf2$^{WT/R70H}$ -clone 3: WT allele1-3xHA tag confirmation* (in reverse orientation)

NNNNNNNNNNNNNNGTGCGTACGGCCCTGGGGACGTCGTCGCGGGTGGCGAG
GCGCACCGTGGGCTTGTACTCGGTCAT
TCCGCTTCCAGGTCCAGGGTTCTCCTCCACGTCTCCAGCCTGCTTCAGCAGGCTG
AAGTTAGTAGC**AGCGTAATCTGGAACATC**
GTATGGGTAAGCGTAATCTGGAACATCGTATGGGTAAGCGTAATCTGGAACAT
CGTATGGGTATGATCCGCCGCCACCCGAC
CCACCTCCGCCCGAGCCTCCGCCACCAGATTTGTGCTCTTTTGTTGGTGCATAATA
AAGTTCCATGGGTTTGTTCACTTTCCAGTA
TTTCTCACTGACCAATTCCAAAGAAAAGGAGCCATTTAAAACCTAAAACAAAAAG
AGGCAAGATTATGAAAATGCATGGTGCTCAG
TAACAGTGAGACTAAATAAACAAAAGGCCACAGGATCCCGTGCACAGCAGGAGA
GATAAAGGGCATCACGGAGTCATTAATCTGC

GGCTTTGCTTCGTGGGCCTCAGGGCTCCCCCCCCCCACCAGACCCACCCAGACCA
CTAGCCAAGGAGCTCAACAGGCATTGAC
AAATACTCACGGTGAACTGGCCACTGGCTGTGGCTATGTAAATGGTGTACTGCTTC
TCACTGGCTGTATCCAGGTTCATCTGGTTT
GATTCTCCTTTGCTTCNAAGTTCTTCTAAAGCTAACCTCACAGCCAGA

Clone #1 Rnf2$^{WT/R70H}$ -clone 3: mutant allele2-3xFLAG tag confirmation (in reverse orientation)

NNNNNNNNNNNNNCNCGCCGGANNCGCTGANTTGTGGCCGTTTACGTCGCCGT
CCAGCTCGACCAGGATGGGCACCACCC
CGGTGAACAGCTCCTCGCCCTTGCTCACCATTCCGCTTCCAGGTCCAGGGTTCTC
CTCCACGTCTCCAGCCTGCTTCAGCAGGC
TGAAGTTAGTAGC**CTTGTCATCGTCATCCTTGTAATCGATGTCATGATCTTTAT**
AATCACCGTCATGGTCTTTGTAGTCTGATCC
GCCGCCACCCGACCCACCTCCGCCCGAGCCTCCGCCACCAGATTTGTGCTCTTTT
GTTGGTGCATAATAAAGTTCCATGGGTTTG
TTCACTTTCCAGTATTTCTCACTGACCAATTCCAAAGAAAAGGAGCCATTTAAAAC
CTAAAACAAAAAGAGGCAAGATTATGAAAAT
CATGGTGCTCAGTAACAGTGAGACTAAATAAACAAAAGGCCACAGGATCCCGTGC
ACAGCAGGAGAGATAAAGGGCATCACGG
AGTCATTAATCTGCGGCTTTGCTTCGTGGGCCTCAGGGCTCCCCCCCTACCAGACC
CACCCAGACCACTAGCCAAGGAGCTCAA
CAGGCATTGACAAATACTCACGGTGAACTGGCCACTGGCTGTGGCTATGT

F. Clone #1 *Rnf2$^{WT/R70H}$* _Clone 4 *WT allele1-3xHA/ mutant allele2-3xFLAG*

Clone #1 Rnf2$^{WT/R70H}$ -clone 4: WT allele1-3xHA tag confirmation (in reverse orientation)

NNNNNNNNNNNNGTGCGTACGGCCCTGGGGACGTCGTCGCGGGTGGCGAGGCG
CACCGTGGGCTTGTACTCGGTCATTCC
GCTTCCAGGTCCAGGGTTCTCCTCCACGTCTCCAGCCTGCTTCAGCAGGCTGAAG
TTAGTAGC**AGCGTAATCTGGAACATCGTA**
TGGGTAAGCGTAATCTGGAACATCGTATGGGTAAGCGTAATCTGGAACATCG
TATGGGTATGATCCGCCGCCACCCGACCCA
CCTCCGCCCGAGCCTCCGCCACCAGATTTGTGCTCTTTTGTTGGTGCATAATAAAG
TTCCATGGGTTTGTTCACTTTCCAGTATTTC
TCACTGACCAATTCCAAAGAAAAGGAGCCATTTAAAACCTAAAACAAAAAGAGG
CAAGATTATGAAAATGCATGGTGCTCAGTAAC
AGTGAGACTAAATAAACAAAAGGCCACAGGATCCCGTGCACAGCAGGAGAGATA
AAGGGCATCACGGAGTCATTAATCTGCGGC
TTTGCTTCGTGGGCCTCAGGGCTCCCCCCCCCCACCAGACCCACCCAGACCACTA
GCCAAGGAGCTCAACAGGCATTGACAAAT
ACTCACGGTGAACTGGCCACTGGCTGTGGCTATGTAAATGGTGTACTGCTTCT

Clone #1 *Rnf2$^{WT/R70H}$ -clone 4: mutant allele2-3xFLAG tag confirmation* (in reverse orientation)

NNNNNNNNNCNCNNCNCNCCGGANNCGCTGACTTGTGGCCGTTTACGTCGCCGT
CCAGCTCGACCAGGATGGGCACCACCC
CGGTGAACAGCTCCTCGCCCTTGCTCACCATTCCGCTTCCAGGTCCAGGGTTCTC
CTCCACGTCTCCAGCCTGCTTCAGCAGGC
TGAAGTTAGTAGC**CTTGTCATCGTCATCCTTGTAATCGATGTCATGATCTTTAT**
AATCACCGTCATGGTCTTTGTAGTCTGATCC
GCCGCCACCCGACCCACCTCCGCCCGAGCCTCCGCCACCAGATTTGTGCTCTTTT
GTTGGTGCATAATAAAGTTCCATGGGTTTG
TTCACTTTCCAGTATTTCTCACTGACCAATTCCAAAGAAAAGGAGCCATTTAAAAC
CTAAAACAAAAAGAGGCAAGATTATGAAAAT
GCATGGTGCTCAGTAACAGTGAGACTAAATAAACAAAAGGCCACAGGATCCCGTG
CACAGCAGGAGAGATAAAGGGCATCACGG
AGTCATTAATCTGCGGCTTTGCTTCGTGGGCCTCAGGGCTCCCCCCCTACCAGACC
CACCCAGACCACTAGCCAAGGAGCTCAA
CAGGCATTGACAAATACTCACGGTGAACTGGCCACTGGCTGTGGCTATGT

Alkaline phosphatase assay and growth curves: Alkaline phosphatase assays were performed according to manufacturer's instructions (Vector Red Substrate Kit, Alkaline Phosphatase, SK-5100). Growth curves were performed after seeding $50x10^3$ ESCs in 6-well plates and counted every 36h for 7 days.

Generation of stable cell lines expressing WT RING1A/B and RING1A/B variants: The cDNAs of WT RING1A/B and RING1A/B variants were cloned into the PiggyBac-based transposon vector plasmid PB713B-1. 0.5×10^6 HEK293T-dKO RING1A/B cells were seeded into each well of a 6-well-plate 1 day prior to transfection. For each well, 0.5 μg of each PB713B-1 plasmid containing the cDNA of WT RING1A/B or RING1A/B variants were transfected using PureFection Transfection Reagent (Cat #LV750A-5) and the PiggyBac transposase vector following manufacturer's instructions (System Biosciences, SBI; PB210PA-1). Two days post transfection, the puromycin (1μg/ml Biogems, #5855822) was added into the medium for 2 weeks.

Generation of stable cell lines expressing HA-Ring1b^{WT}, HA-Ring1b^{R70H}, HA-Ring1b$^{I53A/D56K}$, HA-Pcgf2^{WT} and HA-Pcgf2-ΔIDR: The cDNAs of HA-Ring1b^{WT}, HA-Ring1b^{R70H} and HA-Ring1b$^{I53A/D56K}$ were cloned into the PiggyBac-based transposon vector plasmid pPB[Exp]-EF1A>EGFP/Puro. HA-Pcgf2^{WT} and HA-Pcgf2$^{\Delta IDR}$ cDNAs were clones into the pPB[Exp]-EF1A plasmid. Cells were transfected with 0.5 μg of pPB[Exp]-EF1A>EGFP/Puro constructs, together with 0.5 μg of the PiggyBac transposase vector (System Biosciences, Cat# PB210PA-1) using PureFection Transfection Reagent (System Biosciences, # LV750A-5) following the manufacturer's protocol. Two days post-transfection, cells were replated in medium containing 1 μg/ml puromycin (Biogems, Cat# 5855822) and maintained under selection for two weeks to establish stable lines.

Pcgf2 knockout cell lines: CRISPR/Cas9-mediated knockout of PCGF2 was performed using the lentiCRISPR v2 vector. The target sequences 5′ -CACCTCATGTGTGCCCTCTG-3′ and 5′-CTCCGTGATTTTAATCCGTG-3′

(targeting PCGF2), and 5′-GCGAGGTATTCGGCTCCGCG-3′ and 5′-ATTGTTCGACCGTCTACGGG-3′ (control), were cloned into the vector following the manufacturer's instructions. Lentiviral particles were produced in HEK293T cells (ATCC CRL-3216) by co-transfection with packaging plasmids. Viral supernatants were collected and used to transduce target cells, which were subsequently selected with 2 μg/ml puromycin for five days. Surviving colonies were expanded and maintained as stable *Pcgf2*-KO lines.

Identification of RING1 and RNF2 variants: Whole Exome Sequencing was performed at Mendelics Genomic Analysis facilities using Illumina NovaSeq 6000. Sequencing library is built with Illumina Nextera Flex and for capture of target regions Customized Exome Kit from Twist Biosciences is used. Sequencing of sample results in paired 101 bp sequences that are mapped to hg38 reference using BWA MEM software (http://bio-bwa.sourceforge.net/). Resulting BAM files are genotyped using Broad Institute best practices with GATK and obtained VCF files are processed using Mendelics in-house pipeline for annotation and filtering. "In silico" pathogenicity evaluation is performed using VSA, a Mendelics proprietary machine-learning based software. Aligned BAM files are also processed by ExomeDepth (an R package, see https://cran.r-project.org/web/packages/ExomeDepth/index.html) in order to identify CNVs.

The entire Mendelics Genomic Analysis database of sequenced whole exomes was searched for ultra rare variants (gnomAD browser v2.1.1 and v3.1.2 MAF=0) in *RING1* and *RNF2* and for all individuals found to harbour those variants, subsequently clinical data was revised in order to identify those patients with neurodevelopmental disorders. Potentially relevant variants were then selected from this group considering multiple "in silico" metaprediction tools and evolutionary conservation.

Western blotting: Cells were lysed with high-salt buffer (300nM NaCl, 50mM tris-HCl pH 8, 10% glycerol, and 0.2% NP-40) supplemented with protease inhibitors (Thermo Scientific, A32965 #ZC4200412) and them were sonicated 10min at 4°C with a Bioruptor in 30sec ON/OFF cycles and centrifuged at 16,000 × g for 15min. Soluble material was quantified by Bradford assay (Bio-Rad, #5000006). Western blotting was performed using standard protocols, 40μg were loaded onto SDS-PAGE gel and transferred onto a nitrocellulose blotting membrane (BIO-RAD, #1620167). Non-specific binding was blocked with 5% skim milk in Tris-buffered saline with 0.1% Tween-20 (TBS-T), followed by overnight incubation with primary antibodies. Secondary antibodies: IRDye 800CW donkey anti-mouse IgG (LI-COR, #926-32212) and IRDye 800CW donkey anti-rabbit IgG (LI-COR, #926-32213) were used at a 1:10,000 dilution. WBs were imaged on an Odyssey CLx imaging system (LI-COR) and various exposures within the linear range captured using ImageStudioLite software (Li-COR, v5.2.5). Images were rotated, resized and cropped using Adobe Photoshop 2024 and assembled into figures using in Adobe Illustrator 2024.

Acid histone extraction: Freshly harvested cells ($3.5x10^6$) were washed with cold PBS. Cells were resuspended in pH 6.5 lysis buffer (10 mM tris-HCl pH8, 50 mM sodium bisulfite,1% Triton X-100, 10 mM MgCl2, 8.6% sucrose, and 10 mM sodium butyrate) and then were centrifuged at 15,000 rpm for 1 min at 4°C. After discarding the supernatant,

the pellets were resuspended in lysis buffer shown above and centrifuged at 15,000 rpm for 1 min at 4°C. This step was repeated. Then, the pellet was washed with pH 7.4 wash buffer (10mM Tris and 13mM EDTA). After centrifugation at 15,000 rpm for 1 min at 4°C, supernatant was discarded, and pellets were dissolved in 0.4M H2SO4. After 1 h kept on ice, cells were centrifuged at 15,000 rpm for 10 min. In a new microtube, the supernatant was collected into a new tube including acetone and were incubated overnight at −20°C. Next day, samples were centrifuged at 15,000 rpm for 10 min and the supernatant was discarded. The pellets were air-dried and resuspended in water. Histone concentration was estimated after by measuring absorbance with Bradford reagent. For western blotting, 3μg of histone extractions were loaded in a 15% SDS-Page gel.

Treatment with PRC2 inhibitor: 3.5×10^6 cells were seeded into 150mm dishes. Cells were treated with 1μM of the PRC2 inhibitor GSK343 (Sigma-Aldrich, # SML0766) or DMSO as vehicle control for 2 days followed by western blotting and Cut&Run experiments.

Sample preparation for LC-MS/MS

On beads protein digestion: The proteins immunoprecipitated on the beads were digested by resuspending them in 20 μL of 5 mM DTT and 50 mM ammonium bicarbonate (pH = 8) and left on the bench for about 1 hour for disulfide bond reduction. Samples were then alkylated with 20 mM iodoacetamide in the dark for 30 minutes. Afterward, 500 ng of trypsin were added for overnight digestion.

Sample desalting: Prior to mass spectrometry analysis, samples were desalted using a 96-well plate filter (Orochem) packed with 1 mg of Oasis HLB C-18 resin (Waters). Briefly, the samples were resuspended in 100 μl of 0.1% TFA and loaded onto the HLB resin, which was previously equilibrated using 100 μl of the same buffer. After washing with 100 μl of 0.1% TFA, the samples were eluted with a buffer containing 70 μl of 60% acetonitrile and 0.1% TFA and then dried in a vacuum centrifuge.

LC-MS/MS Acquisition and Analysis: Samples were resuspended in 10 μl of 0.1% TFA and loaded onto a Dionex RSLC Ultimate 300 (Thermo Scientific), coupled online with an Orbitrap Fusion Lumos (Thermo Scientific). Chromatographic separation was performed with a two-column system, consisting of a C-18 trap cartridge (300 μm ID, 5 mm length) and a picofrit analytical column (75 μm ID, 25 cm length) packed in-house with reversed-phase Repro-Sil Pur C18-AQ 3 μm resin. Peptides were separated using a 90 min gradient from 4-30% buffer B (buffer A: 0.1% formic acid, buffer B: 80% acetonitrile + 0.1% formic acid) at a flow rate of 300 nl/min. The mass spectrometer was set to acquire spectra in a data-dependent acquisition (DDA) mode. Briefly, the full MS scan was set to 300-1200 m/z in the orbitrap with a resolution of 120,000 (at 200 m/z) and an AGC target of 5x10e5. MS/MS was performed in the ion trap using the top speed mode (2 secs), an AGC target of 1x10e4 and an HCD collision energy of 35. Proteome raw files were searched using Proteome Discoverer software (v2.5, Thermo Scientific) using SEQUEST search engine and the SwissProt mouse database (updated April 2023). The search for total proteome included variable modification of N-terminal acetylation, and fixed modification of carbamidomethyl

cysteine. Trypsin was specified as the digestive enzyme with up to 2 missed cleavages allowed. Mass tolerance was set to 10 pm for precursor ions and 0.2 Da for product ions. Peptide and protein false discovery rate was set to 1%. Following the search, the relative quantification was performed by dividing the intensity of each identified protein by the reference bait protein (*Rnf2*). Statistical regulation was assessed using heteroscedastic T-test (if p-value < 0.05). Data distribution was assumed to be normal, but this was not formally tested.

Immunofluorescence (IF) staining of neurons: Cells were washed and subsequently fixed with 4% paraformaldehyde (PFA) for 10 minutes at room temperature (RT). Following fixation, cells were permeabilized and blocked using blocking buffer composed of 0.1% Triton X-100 and 3% donkey serum in PBS for 1 hour at RT. Primary antibodies (Tuj1 and MAP2) diluted in blocking solution were applied to the cells and incubated overnight at 4°C. After primary antibody incubation, cells were washed three times with PBS for 5 minutes each. Alexa Fluor-conjugated donkey secondary antibodies (1:1000) were then applied and incubated with the cells for 1 hour at RT. This was followed by two 5-minute washes with PBS. During the third wash, DAPI was included, followed by an additional wash without DAPI. Images were acquired using a Leica THUNDER Imager with a 20x objective.

RNA extraction, library preparation, RNA-seq analysis: Total RNA was isolated from frozen cell pellets using TRIzol reagent (Thermo Fisher Scientific cat# 15596018) according to manufacturer's instructions. Library preparation was performed on DNAse-treated RNA using the Illumina TruSeq Stranded Total RNA Library Prep Gold (Illumina 20020598). TruSeq RNA UD Indexes (Illumina 20022371) were used for the adapter ligation step. Samples were normalized to a concentration of ranging from 100-250ng for input, and 1µl of ERCC spike-in Mix 1 (Thermo Fisher 4456740) diluted 1:200 was added to the samples. RNA-seq fastq files were processed for adapter and quality trimming, alignment and quantification with nf-core rnaseq (https://github.com/nf-core/rnaseq/tree/3.10.1) with the default parameters plus '–extra_trimgalore_args –nextseq 30' using mm10 genome reference and refseq transcripts for annotation and expression quantification of genes. DESeq2 (1.38.3) was used to check for differential expression using the results from rna-seq pipeline in R (v4.4.0). Filtering of q-values, fold-change and tests applied are specified in the figure's legends. Gene Set Enrichment Analysis and Gene Ontology were done with R package ClusterProfiler (v 4.12.6) with p-value adjustment method "BH" and a p-value cutoff < 0.05. Heatmaps for expression was done with package "Pretty Heatmaps" (pheatmap v.1.0.12), for MA and volcano plots packages ggpubr (v0.6.0) and EnhancedVolcano (v1.22.0) were used, respectively.

Cut&Run: CUT&RUN was performed with the CUTANATM ChIC/CUT&RUN kit according to the manufacturer's protocol (EpiCypher, 14-1048). Libraries were generated using the CUTANA™ CUT&RUN Library Prep Kit (14-1001). HEK293T-dKO RING1A/B, HEK293T-dKO RING1A/B + RING1B^{WT} and HEK293T-dKO RING1A/B + RING1B^{R70H} cells were treated with 1µM the PRC2 inhibitor GSK343 (Sigma-Aldrich, # SML0766) for 48h. 500,000 cells were collected for Cut&Run kit (CUTANATM ChIC/CUT&RUN) according to the manufacturer's protocol (EpiCypher, 14-1048). Anti-H3K27me3

(EpiCypher, 13-0055) and anti-IgG (EpiCypher, 13-0042K) were used for CUT&RUN. Libraries were generated using the CUTANATM Library Prep Kit Primer Set 2 (EpiCypher, 14-1002, lot: 23317004-01) according to manufacturer's instructions and sequenced on an Illumina NovaSeq X Plus.

ChIP-seq: For each sample, 10×10^6 ESC were subjected to cross-linking with 1% formaldehyde for 10 minutes. The cross-linking reaction was quenched using 0.125 M glycine. Subsequently, cells were lysed in 1 mL of HEPES buffer (0.3% SDS, 1% Triton X-100, 0.15 M NaCl, 1 mM EDTA, 0.5 mM EGTA, 20 mM HEPES). Chromatin fragmentation was achieved using a Bioruptor (Diagenode) set to High, with 10 cycles of 30 seconds ON/30 seconds OFF, yielding DNA fragments averaging 300 bp in size. The fragmented chromatin was diluted to 0.15% SDS and incubated overnight at 4°C with specific antibodies and 20 μL of protein A/G magnetic beads (Upstate). The bead-chromatin complexes were washed at 4°C using wash buffer 1 (0.1% SDS, 0.1% deoxycholate, 1% Triton X-100, 0.15 M NaCl, 1 mM EDTA, 0.5 mM EGTA, 20 mM HEPES), wash buffer 2 (0.1% SDS, 0.1% sodium deoxycholate, 1% Triton X-100, 0.5 M NaCl, 1 mM EDTA, 0.5 mM EGTA, 20 mM HEPES), and wash buffer 3 (0.25 M LiCl, 0.5% sodium deoxycholate, 0.5% NP-40, 1 mM EDTA, 0.5 mM EGTA, 20 mM HEPES). Final washes were performed twice with Tris-EDTA buffer. Chromatin elution was carried out using 1% SDS and 0.1 M $NaHCO_3$. Cross-link reversal was achieved by incubation at 65°C for 5 hours with 200 mM NaCl, followed by phenol-chloroform extraction and ethanol precipitation. The resulting immunoprecipitated DNA served as input material for library preparation using the NEBNext® Ultra™ II DNA Library Prep Kit (NEB) and sequenced on an Illumina NovaSeq X Plus.

RNA extraction and RT-qPCR: Total RNA was isolated from frozen cell pellets using TRIzol reagent (Thermo Fisher Scientific cat# 15596018) according to manufacturer's instructions and extracted using the RNeasy Mini Kit (Qiagen). mRNA was quantified with NanoDrop, and equal amounts of mRNA were retro-transcribed using oligo(dT) and SuperscriptIII (Invitrogen). cDNAs were normalized for the expression of *GAPDH*. RT-qPCR was performed using the C1000 Touch Thermal Cycler CFX96-Real-Time System (BIO-RAD), CFX Manager Software Version 3.1 and the iTaq Universal SYBR Green Supermix reagents (#1725124, BIO-RAD). Differences between samples and controls were calculated based on the $2^{-\Delta\Delta CP}$ method.

Generation of NPCs and differentiation of NPCs: NPCs and differentiated NPCs were generated following the protocol from Bibel and colleagues.[49] Briefly, ESCs were cultured on 0.2% gelatin-coated plates in ES medium supplemented with the MEK inhibitor PD0325901 and the GSK3 inhibitor CHIR99021 (2i) and LIF and passaged every two days for 2–3 passages. Cells were subsequently maintained for two passages in ESC medium supplemented with 15% FBS/LIF. For NPC formation, ESCs were dissociated and 4×10^6 cells were cultured in suspension in embryoid body (EB) medium without LIF. EB medium was changed every two days, and on day 4, the medium was replaced with EB medium supplemented with 5 μM of retinoic acid (RA). Medium changes with RA were repeated every two days until day 8. NPCs were collected on day 8, and their identity was confirmed

by expression of NPC markers. Rescue experiments were performed by adding 3 μg of CHIR99021 at day 6 of ESC differentiation with retinoic acid and 10% FBS. Samples for RT-qPCR were collected at day 14 of differentiation.

Differentiation of ESC into primitive endoderm: Differentiation was performed as in Anderson and colleagues[102] with minor modifications. ESCs were differentiated by plating 1×10^6 cells onto gelatinized 10 cm plates in 2i/LIF medium. After 24h, 2i/LIF medium was replaced by endoderm medium (RPMI 1640 medium with Glutamax (Gibco), supplemented with B27 minus insulin (Gibco A1895601), Activin A (4 ng ml) and CHI99021 (3 μM). The medium was changed every 24h for 10 days.

ATAC-seq, Cut&Run and ChIP-seq common data processing overview: Sequenced reads (FASTQ files) were processed with nf-core pipelines[87] for adapter trimming, QC (FASTQC),[90] alignment (bowtie2),[91] read filtering for not primary alignment and duplicated reads (SAMtools). Nf-core/chipseq v2.2.0 (https://github.com/nf-core/chipseq/tree/2.0.0), nf-core/atacseq v2.1.2 (https://github.com/nf-core/atacseq/tree/2.1.2) and nf-core/cutandrun v3.2.2 (https://github.com/nf-core/cutandrun/tree/3.2.2) were used for the respective experiment using default parameters and additional '–aligner bowtie2 –read_length 150 –trim_nextseq 20 –blacklist [BED]'. A list of references of the software, tools and its versions used are documented in their respective repositories. For *Mus Musculus* samples genome reference mm10 was used with encode excludable regions bed file (https://www.encodeproject.org/files/ENCFF547MET/) and for human cell lines and human spike-ins for some ChIP-seq samples, the genome refence used washg38 and excludable regions from Encode (https://www.encodeproject.org/files/ENCFF356LFX/) while For E.coli spike-in of Cut&Run protocol, the genome reference used was Escherichia_coli_K_12_MG1655.

Cut&Run data processing: Reads were first aligned to the spike-in genome (with additional bowtie2 args –un-conc <prefix> and –end-to-end), the resulting unaligned fastqs were aligned with the target reference Normalized bigWig files were generated using a scaling factor calculated by a constant of 10,000 divided by the number of spike-in reads.

ChIP-seq data processing: Reads were further (besides the described in seq common data processing overview) filtered to exclude those containing more than four mismatches, as identified using SAMtools,[89] read pairs with an insert size exceeding 2 kilobases, pairs mapping to different chromosomes, or those not in FR orientation. Furthermore, read pairs were discarded if only one mate failed any of the mentioned criteria (pySAM). For ChIP-seq without spike-in, alignment files (BAMs, from nf-core described previously) were processed using the ENCODE Pipeline 2 (v2.2.1). The pipeline was configured to down sample reads to 30M and then normalizes read counts to adjust for differences in sequencing depth (in case of final filtered reads not reaching 30M), followed by background correction using input controls in MACS2 callpeak function (using the flag –SPMR). Log10 fold of p-values based on a Poisson distribution over input lambda was then computed for each nucleotide across the genome using the bdgcmp function. Peak calling consistency between replicates was assessed using Irreproducible Discovery Rate (IDR)

(https://www.encodeproject.org/publications/8312fc0c-b241-4cb2-9b01-1438910550ad), as described in ENCODE publication. For ChIP-seq experiments with spike-in, reads were first aligned with spike-in reference and subsequently removed for further alignment with target reference. Scale factors were calculated by antibody group by first selecting the sample with the lowest number of spike-in reads then dividing it by the total number of reads aligned in target reference for each sample.

ATAC-seq data processing: Reads were further (besides the described in seq common data processing overview) filtered to exclude those containing more than four mismatches, as identified using bamtools, read pairs with an insert size exceeding 2 kilobases, pairs mapping to different chromosomes, or those not in FR orientation and soft-clipped reads. Furthermore, read pairs were discarded if only one mate failed any of the mentioned criteria (pySAM). Normalized coverage tracks were generated in bigWig format. Read coverage was first calculated with bedtools genomecov, converted to bedGraph, and normalized to 1 million mapped reads prior to conversion with bedGraph-ToBigWig (kent tools). Peak calling was performed using MACS2, applying broad peak calling and consensus peaks between replicates were identified using bedtools.[93]

Cut&Run, ATAC-seq and ChIP-seq profile plots, heatmaps, boxplots and statistical analysis: For visualization in UCSC genome browser, heatmaps and profile plots ChIP-seq and Cut&Run replicates were merged using bigwigAverage '-bs 2' (deepTools v 3.5.5),[88] this step was not required for ATAC-seq once the pipeline provides the merged replicates bigwigs. GNU parallel (https://doi.org/10.5281/zenodo.11247979) was used to process the data efficiently in several steps as well as singularity[103] for containerization in nf-core and encode pipelines. Signal profile plots and heatmaps were generated with deepTools (deepTools v3.5.5) with sub-commands plotHeatmap or plotProfile. Boxplots and violin plots were calculated from bigwigs averaged for every 2 bases of the region of interest using multiBigwigSummary (deepTools) with default parameters except for the resolution '-bs 2' and '–outRawCount' generating a tab-separated file to be loaded in R v4.4.0 and plots with the signal of samples and statistical tests were created using ggplot2 (v 3.5.1) with ggsignif and ggprism (v1.0.5). MultibigwigSummary result data was manipulated with libraries dplyr (1.1.4) and reshape2 (v1.4.4). Homer v5 was used for motifs and peak annotation and signal over chromosomes arms were created with karyoploteR (v1.30.0).

Single cell RNA-seq: About 10,000 WT, clone #1 and #2 of *Rnf2*$^{WT/R70H}$ 16-days old differentiated NPC cells after QC filter were used for downstream analyses. Merged replicates paired-end fastq files demultiplexing, barcode processing, gene counting and aggregation were made using Cell ranger software v7.2.0 and the results were loaded in R with the Read10X function from Seurat package[94] (v5.1.0) with parameters 'min.cells = 3, min.features = 200', additional filtering for minimum of 2000 and maximum of 12000 genes detected per cell and mitochondrial percentage of reads <20%, doublets were inferred using pK optimization in DoubletFinder.[104] For cluster annotation scType[105] with PanglaoDB[106] database was used with a custom (perl) script to make panglaodb files compatible with scType. Speckle[107] was used to generate proportions of cells.

Single cell nuclei RNA-seq and ATAC-seq: Data Processing and Quality Control (QC): FASTQ files generated from snATAC+RNA profiling of mouse hippocampus (mHC) and prefrontal cortex (mPFC) were processed using Cell Ranger ARC v2.0.2 (count function) with the mm39 reference genome. This pipeline performed read alignment, barcode filtering, peak calling, and quantification of both ATAC and gene expression (GEX) features. The resulting output was imported into R (v4.4.0) using the Read10X function from Seurat (v5.3.0), creating a Seurat object. Chromatin accessibility data were incorporated using CreateChromatinAssay from the Signac package[95] (v1.14.0). Initial QC was conducted by inspection of key metrics, including mitochondrial content (percent.mt ≤ 3%), RNA feature counts (nFeature_RNA ≥ 1000 and ≤ 15,000), ATAC fragment counts (nCount_ATAC ≥ 1000), RNA molecule counts (nCount_RNA ≤ 30,000), and transcription start site (TSS) enrichment (≥ 0.5). Doublets were identified and removed using DoubletFinder, with optimal pK values determined via parameter sweep and bimodality coefficient analysis.

snRNA-seq and snATAC-seq clustering, annotation and downstream analysis: Samples were merged by condition (WT or R70H mutant) and integrated into a single Seurat object. Dimensionality reduction was performed using Uniform Manifold Approximation and Projection (UMAP) based on 19 principal components (PCs), selected after evaluating elbow plots. RNA data were normalized using SCTransform, while ATAC data were normalized using term frequency–inverse document frequency (TF-IDF). A weighted nearest neighbor (WNN) graph was constructed to integrate RNA and ATAC modalities for downstream analysis. Cell type annotation was performed using scType (https://doi.org/10.1038/s41467-022-28803-w) with the Panglao database “Brain”tissue[106] and for mPFC, a manual curated list of markers of mPFC.[108,109] A custom Perl script was used to adapt markers lists for compatibility with scType. Cell-type proportions were calculated using Speckle’s (R package) get-TransformedProps function where variance stabilizing transformation on the proportions was applied (parameter transform=“logit”). FindMarkers (Seurat) was used to find peaks with differential accessibility and were annotated by ClosestFeature (Signac), ClusterProfiler[92] 4.12.6 (R package) was used to explore the pathways affected. To refine peaks for each cluster and condition (WT and R70H), CallPeaks (Signac, NMACS3) was used with parameters shift=100 and extsize=200 to call peaks, then only stronger peaks were selected by keeping peaks in which −Log10(qvalue) was above the median of the −Log10(qvalue) for each cluster and condition. After filtering, counts in peaks were normalized using RunTFIDF (Signac) and global average accessibility by cluster was calculated. Resulting peak files were processed using Homer v585 to find enriched motifs, p-values were transformed to zscore and the scale was changed to binary color to facilitate visualization of the heatmaps constructed using pheatmap (R). Trajectory construction and pseudotime analysis were conducted separately for WT and R70H conditions using Slingshot (v2.12.0), which infers lineages and orders cells in pseudotime within a reduced-dimensional embedding. Slingshot was chosen because it can automatically determine an appropriate start points for trajectories based on data topology, which suited the exploratory nature of these datasets. Pseudotime values were assigned to each cell along its lineage to represent its progression through the trajectory. Lineages and trajectories were visualized with cells colored by cluster identity and lineage paths overlaid,

and pseudotime distributions were compared across lineages between WT and R70H cells. For visualization, pseudotime values from all inferred lineages were combined to generate comprehensive pseudotime plots for each condition. For the mHC dataset, the start cluster for the R70H condition was set to “Astrocytes” to correspond with the start cluster used for WT, ensuring comparability between conditions. In the mPFC dataset, both conditions shared the same start cluster by default. Using identical start clusters across conditions was essential to maintain consistency in downstream comparisons.

3D Protein modeling and mutation effects predictions: 3D protein structures were created using ColabFold in COSMIC2 with default parameters and the resulting PDB with ranking of 001 file was loaded in PyMol (v3.0.4) with variables h_bond_cutoff_edge and h_bond_cutoff_center set to 3.2 and 3.6, respectively. Mutations and amino-acid changes were visualized with PyMol Wizard->Mutagenesis function, hydrogen bonds and salt bridges were calculated with with dist() function mode=2 and mode=10, respectively. Custom scripts were created to calculate the interface interactions and to create images in the same position/angle before and after the mutation was applied.

Immunoprecipitation (IP): IPs in HEK293T: 50µl/sample of Dynabeads Protein G (Thermo Fisher Scientific; 10004D lot:3095287) and Anti-HA Magnetic Beads (Thermo Scientific, #88836) were washed three times with 1ml cold IP Buffer (300nM NaCl, 50mM tris-HCl pH 8, 10% glycerol, and 0.2% NP-40) supplemented with protease inhibitors (Thermo Scientific, A32965 #ZC4200412). Beads were resuspended in 1ml total volume cold IP Buffer containing rabbit IgG (EMD Millipore Corp; 12-370) or rabbit anti-HA antibody (C29F4; Cell Signaling Technology), 10µg/sample, and rotated at 4°C overnight. Flag and HA IPs in ESCs and NPCs were performed using Anti-FLAG M2 Magnetic Beads (Sigma Aldrich) or Pierce™ Anti-HA Magnetic Beads (Thermo Fisher). IPs were performed using nuclear fraction. Cells were lysed on ice for 10 min with Buffer A (10 mM HEPES, 1.5 mM MgCl2, 10 mM KCl, 0.5 mM DTT, 0.05% NP40, pH 7.9) followed by centrifugation at 2,300g for 5 min. Supernatant was discarded and the procedure was repeated. The cell pellet was dissolved in IP300 (half of the volume used for Buffer A) and processed as described in the WB section. 1mg of protein was used for each IP and 500μg of nuclear extract as the input material. IP material was washed three times with high-salt buffer (500nM NaCl, 50mM tris-HCl pH 8, 10% glycerol, and 0.2% NP-40), eluted with Laemmli buffer and loaded onto SDS-PAGE.

Subcellular fractionation: 80% confluent HEK293T cells were collected with a cell scraper and washed 1x with PBS, then centrifuged for 5min at 400×g. Cell pellet was resuspended 1:5 (w:v) in Buffer A (10mM HEPES [pH 7.9], 1.5mM $MgCl_2$, 10mM KCl, 0.05% NP-40) supplemented with protease inhibitors and 0.5mM DTT. After 10min on ice, cells were centrifuged for 5min at 400×g. The supernatant, representing the cytosolic fraction, was collected and stored at 4°C. The remaining nuclear pellet was resuspended in ¾ of the initial volume with Buffer B (5mM HEPES [pH 7.9], 1.5mM $MgCl_2$, 0.2mM EDTA, 26% glycerol) supplemented with protease inhibitors and 0.5mM DTT, and homogenized with 20 strokes in a Dounce homogenizer fitted with pestle A. After 20min on ice, extracts were centrifuged for 20min at 16,000×g. The supernatant, representing

the soluble nuclei fraction, was collected and stored at 4°C. The remaining pellet was resuspended in ½ of the original volume with high-salt buffer (300mM NaCl, 50mM Tris-HCl [pH 8], 10% glycerol, and 0.2% NP-40) supplemented with protease inhibitors and sonicated with a Bioruptor for 5min in 30” ON-OFF cycles. After centrifugation at 16,000×g for 20min, the supernatant, representing the soluble chromatin fraction, was stored at 4°C. The remaining pellet, representing the insoluble chromatin fraction, was resuspended in volume equal to original volume with 2x Laemmli buffer and sonicated with a Bioruptor for 10min in 30” ON-OFF cycles. Protein concentration of cytosolic, soluble nuclei and soluble chromatin fractions were determined by Bradford assay, and 20μg of protein and 1/5 of the insoluble chromatin fraction material were loaded onto SDS-PAGE gels followed by western blotting.

Order of behavioral tests: At 8 weeks of age mice were subjected to a battery of tests with 0-2 days between tests in the following order: (i) Barnes maze, (ii) Open field, and (iii) Pavlovian conditioned fear. Sociability and social novelty were performed at different days with different mice. For each test, the number of mice tested was 10, all males, unless specified in the figure legend.

Barnes maze test: The Barnes maze task was conducted on a circular PVC platform (100 cm in diameter) with 18 holes (hole diameter: 5.5 cm) along the perimeter. A black plexiglass escape box was located under one of the holes, the hole above the escape box represented the target.

The test consisted of 4 consecutive days. Days 1and 2-3 where for habituation (pre-training trial) and reference memory (training trial). On day 4 the test trial was performed. On the habituation trial, mice were placed in the center of the maze covered by a black cylinder, after 10 sec mice were released, guided to the escape box and allowed to remain there for 2 min. Following the pre-training trial, the training trials started. At the beginning of each trial, mice were placed in the same position (center of the platform) and covered with the black cylinder for 10 sec followed by release and allowing them to explore the maze. The trial ended when the mice entered the escape box or after 3 min. The animal was allowed to stay in the box for 1 min. Mice were trained three trials per day/2 days. On day 4, a probe test was conducted without the escape box, to assess memory based on distal environmental room cues. Latency to reach the target hole was recorded and data were analyzed. Behavioral data was performed utilizing the two-tailed Student’s t-test. P-value ≤ 0.05 was considered statistically significant.

Open field: Mice were placed in the center of a clear plexiglass (40 x 40 x 30 cm) open field arena, and allowed to explore for 30 min. Exploratory behavior and general activity in the open filed is quantitated by a computer-operated activity monitor software (DOC-102, Med Associates). Behavioral data was performed utilizing the two-tailed Student’s t-test. P-value ≤ 0.05 was considered statistically significant.

Pavlovian conditioned fear: Mouse was first placed into a chamber for 5 min (pre-context) to allow exploration. The fear-conditioning training consisted of a 3 min acclimation period followed by an 80 dB (2.8 kHz) white noise that was presented for 30 sec

as a conditional stimulus (CS) followed by a mild foot-shock (2 sec, 0.75 mA), which served as the unconditioned stimulus (US). After 2 min another CS-US pair was presented. Two minutes later the animal is placed in their home cage. After 24h (long term memory) or 2hrs (short term memory), mice were placed again in the same chamber to test their contextual memory ability, which consist of exploration for 5 minutes in the same chamber that was used the day before. Cue testing is performed after one hour of the context testing, mice were put in the chamber, but the environmental cue, contextual cue, and odor were changed; for this purpose, black triangular plexiglass was inserted to alter the shape and spatial cues, red house lights replaced the white house lights, the wire grid floor was covered with white plexiglass, and 5 % acetic acid was used to alter the smell. Two phases of the CS test were recorded, in the first phase (pre-sound cue) freezing time was recorded for 3 min, then a 30-sec tone without foot-shock was presented, finally, immediately after the tone occurred, the second phase for another 3 min was recorded to evaluate the mouse memory ability (post-sound). Mouse freezing software (Medpc-IV, Med Associates) was used to analyze the freezing time during the test. Behavioral data was performed utilizing the two-tailed Student's t-test. P value ≤ 0.05 was considered statistically significant.

Sociability and social novelty Test: Social behavior was assessed using a rectangular three-chambered polycarbonate apparatus.[110,111] Retractable doors in the dividing walls permitted access between chambers. All sessions were video recorded for analysis. The test comprised three 10-minute phases: 1. Habituation: The test mouse was placed in the central chamber and allowed to explore the entire apparatus while its position was recorded. 2. Sociability: After habituation, the mouse was briefly returned to its home cage. An unfamiliar mouse (Stranger 1) was enclosed in a perforated container (allowing visual/olfactory cues but preventing contact) in one side chamber, while an identical empty container was placed in the opposite chamber. The test mouse was reintroduced, and its position recorded for 10 minutes. 3. social novelty: The test mouse was again returned to its home cage, and a second unfamiliar mouse (Stranger 2) replaced the empty container. The test mouse's exploration was recorded for a final 10 minutes. Data were analyzed as the percentage of total time spent in each chamber per phase. A subset of wild-type mice failed to exhibit the expected social discrimination, showing no preference for Stranger 1 over the empty chamber during the sociability phase or for Stranger 2 over Stranger 1 during the novelty phase. We excluded outliers defined as data points with |Z-score| > 3 (standard deviations from the mean) in sociability or social novelty indices.[112] Specifically, 2 out of 7 wild-type mice were excluded in the sociability phase, while 1 out of 7 was excluded for outliers in the novelty phase. Importantly, outlier identification was performed prior to group comparisons to prevent bias in the interpretation of results.

MRI tractography

Image acquisition: A 2.5% isoflurane in oxygen flow was used to induce anesthesia and then the mouse was transferred to the cradle and the head secured. Anesthesia was maintained for the reminder of the experiment with a 1.2-1.5% isoflurane in oxygen. The mouse cradle was placed in the middle of a 9.4 tesla spectrometer (Bruker, BioSpec 94/20). Animal temperature was kept at 37 °C by forced warm air and respiration was monitored remotely (SAII, USA). A combination of a transmitter volume coil and a receiver array

surface coil was used for image acquisition. A B0 map was acquired and a localized shimming on the head was performed to reduce B0 inhomogeneity. For the diffusion tensor imaging (DTI) experiment a 4-shots, spin echo, echo planar imaging sequence was used (TR/TE 2100/28ms, Δ9ms, δ2.8). Five b0 (b value = 0s/mm2) images and 1 reverse phase image were acquired before the acquisition of 2-shells (b value = 800s/mm2 and b value = 1600s/mm2 respectively) diffusion weighted images with diffusion encoded gradients applied to 30 even-spaced directions (automatically calculated by the acquisition software, ParaVision 360 V3.5). Images were acquired with a matrix size of 114 (read) x 80 (phase), field of view of 18.2 x 12.2mm, resulting in an in-plane resolution of 160 x 160μm and 40 contiguous 320μm thick coronal slices. The number of averages was 4. For the anatomical images a T2-weighted rapid-relaxation-with-enhancement (RARE) spin echo sequence was used (TR/TE 3500/33ms, RARE factor = 8). The resolution was the same as for the diffusion experiment, the number of averages was 10.

DTI analysis: Analysis of the Diffusion imaging dataset is based on MRtrix3 software package.[113] Briefly, after a denoising and unringing step the images were corrected for motion and distortion. Response functions for white matter, gray matter and cerebrospinal fluid were obtained and, after upsampling the diffusion images, a white matter fiber orientation distribution function (FOD) was extracted using multi-shell multi-tissue constrained spherical deconvolution. After the creation of a FOD population study-specific template, all subject FODs were registered and warped to the template space. A whole-brain fiber tractography was created and possible biases in tractogram densities were reduced. An adapted version of the Allen mouse brain atlas (atlas.brain-map.org) was registered to the population template for subsequent atlas-based fiber analysis using as target a mean b0 template generated with the averaged b0 images of each subject warped to the FOD template space.

Statistical analysis: Three littermate pairs were used for the analysis of the DTI datasets. Two-tailed t test were performed using GraphPad Prism. $P < 0.05$ was considered statistically significant.

Brain volume analysis: Anatomical images of the brain were bias field corrected, and their brain was automatically extracted using FSL (FMRIB Software Library, University of Oxford, UK) bet tool[114] and then manually cleaned. A study specific minimum deformation template was then generated, and all animal brains were registered to it using a rigid registration method (ANTs). Brain volume was then calculated using FSL fslstats tool. Five littermate pairs were used for the brain volume analysis. Two-tailed t test were performed using GraphPad Prism. $p < 0.05$ was considered statistically significant.

Computed Tomography imaging: All mice were CT imaged on the MILabs Vector 6 PET/SPECT/CT using the following imaging parameters: whole-body scan, accurate scan mode, step angle: 0.500, projections per step: 1, binning: 1 × 1, tube voltage: 50 kV, tube current: 0.21 mA, exposure time: 75 ms, imaging time: 2 min 40 sec, dose estimate: 70 mGy. Images were subsequently reconstructed using the MILabs reconstruction software.

All image analysis was generated using Imalytics Preclinical 2.1 software. Representative 3D images were generated with a threshold of 2,500 HU.

C. elegans protein sequence alignment and structure prediction: Protein sequences were aligned with Clustal Omega using default settings.[115] The accessions for the full protein sequences are *D. melanogaster* SCE NP_477509.1, *C. elegans* SPAT-3 NP_001024904.2, *M. musculus* RING1A NP_033092.3, *M. musculus* RING1B NP_001407870.1, *H. sapiens* RING1A NP_002922.2, and *H. sapiens* RING1B NP_009143.1. The AlphaFold2[83]-predicted structure of MIG-32(303-393) and SPAT-3(104-247) was generated with ColabFold (v1.5.5)[85] and visualized with PyMOL (v3.0.4) (Schrödinger, LLC.). The complex structures were predicted using AlphaFold3[84] and ColabFold (v1.5.5).[85] The effect of point mutations on the binding affinity of the predicted complexes or the PDB 2H0D heterodimer structure were calculated using MutaBind2.[86] Alphfold3 output CIF files were converted to PDB using Gemmi.

Immunoblots from C. elegans extracts: For each strain, an equal number of gravid adults were obtained and NuPAGE LDS sample buffer (Invitrogen) and dithiothreitol were added to final concentrations of 1X and 100 mM, respectively. Samples were snap-frozen and thawed twice and then heated at 95°C for 5 minutes and vortexed twice. The lysates were centrifuged (16,000*g*, 2 min.) and the supernatant was transferred to a new tube. Lysates were resolved on a 3-8% Tris-Acetate or 4-12% Bis-Tris NuPAGE gel (Invitrogen) and transferred to nitrocellulose. Blots were probed with the following antibodies: anti-HA (1:1000, C29F4 #3724; Cell Signaling Technology), anti-actin (1:3000, A2066; Sigma-Aldrich), anti-H2AK119ub (1:2000, D27C4 #8240; Cell Signaling Technology), anti-histone H3 (1:6000, ab1791; Abcam). The secondary antibody was HRP-conjugated goat anti-rabbit IgG (1:3000, #7074; Cell Signaling Technology). Chemiluminescent signal was visualized using a ChemiDoc MP (Bio-Rad) and densitometry was performed in FIJI.[116]

Mouse H&E: Mouse brain tissue samples were dissected and fixed in 4% paraformaldehyde at room temperature. Following fixation, the tissues were processed overnight using the Leica ASP 300S Processor (Leica Biosystems, GmbH, Germany) and subsequently embedded in paraffin. Slides were sectioned at 5 μm and stained with hematoxylin and eosin (H&E) using the Leica Bond RXm automated research stainer (Leica Biosystems, GmbH, Germany).

Quantitative analysis of histology images: Visiopharm software was used to automate the quantification of the IHC and H&E-stained images. For image analysis, three coronal brain sections spanning rostral to caudal regions were selected per animal, matched based on gross anatomical landmarks. For cell counts within 20 × 20 μm regions of interest (ROIs) in the mouse mPFC subregions, precise anatomical alignment within the anterior cingulate cortex (ACC), prelimbic cortex (PL), and infralimbic cortex (IL) was established using the Allen Mouse Brain Atlas.

Nuclei detection was performed using the Visiopharm app #10167 Nuclei Detection, AI (Brightfield). The detection model was further trained on whole-slide images (WSI) from the dataset to enhance performance. Positive cells were identified with threshold parameters

in the post processing. A positive cell is any object having a mean intensity below 200 for the DAB feature based on the 50% darkest (most expression) pixels in each cell. Results were quality controlled by two researchers independently. Quantified IHC and H&E data was graphed and analyzed in Prism 10.3.1 software (GraphPad Software, Inc., La Jolla, CA, USA).

QUANTIFICATION AND STATISTICAL ANALYSIS

The number of independent replicates, statistical tests, exact value of n and what n represents for each experiment is always defined in the legend. Statistical analyses were performed using GraphPad Prism (Version 8, GraphPad Software).

Supplementary Material

Refer to Web version on PubMed Central for supplementary material.

ACKNOWLEDGMENTS

We are indebted to members of the Morey laboratory for discussions and the Oncogenomics Core Facility (RRID: SCR022502) and Cancer Modeling Shared Resource (RRID: SCR_022891) at the Sylvester Comprehensive Cancer Center (SCCC). We thank Dr. Koseki and Dr. Moazed for sharing Ring1A$^{-/-}$; Ring1B$^{fl/fl}$; Rosa26::CreERT2 ESCs and HEK293T-dKO RING1A/B, respectively. This work was supported by SCCC funds and R01GM141349 and R01GM146409 from the National Institute of General Medical Sciences (NIGMS) to L.M. R.E.V. was supported by SCCC funds and R01GM146409 from NIGMS. B.D.S. is a Cancer Prevention and Research Institute of Texas (CPRIT) Scholar and supported by the CPRIT Recruitment of First-Time, Tenure-Track Faculty Member award RR200079 and 1R35GM147126-01. E.J.P. is supported by NIH 1F30HD114315. A.L.S. is supported by NSERC Discovery grant # RGPIN-2019-06843. S.T. is supported by R35GM127034 from NIGMS. Research in this publication was also supported by the National Cancer Institute of the National Institutes of Health under award number P30CA240139. The content is solely the responsibility of the authors and does not necessarily represent the official views of the National Institutes of Health.

REFERENCES

1. Boyle CA, Boulet S, Schieve LA, Cohen RA, Blumberg SJ, Yeargin-Allsopp M, Visser S, and Kogan MD (2011). Trends in the prevalence of developmental disabilities in US children, 1997–2008. Pediatrics 127, 1034–1042. 10.1542/peds.2010-2989. [PubMed: 21606152]
2. Zablotsky B, Black LI, Maenner MJ, Schieve LA, Danielson ML, Bitsko RH, Blumberg SJ, Kogan MD, and Boyle CA (2019). Prevalence and Trends of Developmental Disabilities among Children in the United States: 2009–2017. Pediatrics 144, e20190811. 10.1542/peds.2019-0811. [PubMed: 31558576]
3. Li Q, Li Y, Zheng J, Yan X, Huang J, Xu Y, Zeng X, Shen T, Xing X, Chen Q, et al. (2023). Prevalence and trends of developmental disabilities among US children and adolescents aged 3 to 17 years, 2018–2021. Sci. Rep 13, 17254. 10.1038/s41598-023-44472-1. [PubMed: 37828147]
4. Jakovcevski M, and Akbarian S (2012). Epigenetic mechanisms in neurological disease. Nat. Med 18, 1194–1204. 10.1038/nm.2828. [PubMed: 22869198]
5. Bölicke N, and Albert M (2022). Polycomb-mediated gene regulation in human brain development and neurodevelopmental disorders. Dev. Neurobiol 82, 345–363. 10.1002/dneu.22876. [PubMed: 35384339]
6. Moris N, Pina C, and Arias AM (2016). Transition states and cell fate decisions in epigenetic landscapes. Nat. Rev. Genet 17, 693–703. 10.1038/nrg.2016.98. [PubMed: 27616569]
7. Waldron D (2016). Development: A colourful map of cell fate. Nat. Rev. Genet 17, 252. 10.1038/nrg.2016.48. [PubMed: 27040485]

8. Morey L, Santanach A, and Di Croce L (2015). Pluripotency and Epigenetic Factors in Mouse Embryonic Stem Cell Fate Regulation. Mol. Cell. Biol 35, 2716–2728. 10.1128/MCB.00266-15. [PubMed: 26031336]

9. Kim JJ, and Kingston RE (2022). Context-specific Polycomb mechanisms in development. Nat. Rev. Genet 23, 680–695. 10.1038/s41576-022-00499-0. [PubMed: 35681061]

10. Tamburri S, Rustichelli S, Amato S, and Pasini D (2024). Navigating the complexity of Polycomb repression: Enzymatic cores and regulatory modules. Mol. Cell 84, 3381–3405. 10.1016/j.molcel.2024.07.030. [PubMed: 39178860]

11. Blackledge NP, and Klose RJ (2021). The molecular principles of gene regulation by Polycomb repressive complexes. Nat. Rev. Mol. Cell Biol 22, 815–833. 10.1038/s41580-021-00398-y. [PubMed: 34400841]

12. Morey L, Pascual G, Cozzuto L, Roma G, Wutz A, Benitah SA, and Di Croce L (2012). Nonoverlapping functions of the Polycomb group Cbx family of proteins in embryonic stem cells. Cell Stem Cell 10, 47–62. 10.1016/j.stem.2011.12.006. [PubMed: 22226355]

13. Morey L, Aloia L, Cozzuto L, Benitah SA, and Di Croce L (2013). RYBP and Cbx7 define specific biological functions of polycomb complexes in mouse embryonic stem cells. Cell Rep. 3, 60–69. 10.1016/j.celrep.2012.11.026. [PubMed: 23273917]

14. Gao Z, Zhang J, Bonasio R, Strino F, Sawai A, Parisi F, Kluger Y, and Reinberg D (2012). PCGF homologs, CBX proteins, and RYBP define functionally distinct PRC1 family complexes. Mol. Cell 45, 344–356. 10.1016/j.molcel.2012.01.002. [PubMed: 22325352]

15. Fischer S, Weber LM, and Liefke R (2022). Evolutionary adaptation of the Polycomb repressive complex 2. Epigenetics Chromatin 15, 7. 10.1186/s13072-022-00439-6. [PubMed: 35193659]

16. Macrae TA, Fothergill-Robinson J, and Ramalho-Santos M (2023). Regulation, functions and transmission of bivalent chromatin during mammalian development. Nat. Rev. Mol. Cell Biol 24, 6–26. 10.1038/s41580-022-00518-2. [PubMed: 36028557]

17. Condemi L, Mocavini I, Aranda S, and Di Croce L (2024). Polycomb function in early mouse development. Cell Death Differ. 32, 90–99. 10.1038/s41418-024-01340-3. [PubMed: 38997437]

18. Piunti A, and Shilatifard A (2021). The roles of Polycomb repressive complexes in mammalian development and cancer. Nat. Rev. Mol. Cell Biol 22, 326–345. 10.1038/s41580-021-00341-1. [PubMed: 33723438]

19. Doyle EJ, Morey L, and Conway E (2022). Know when to fold 'em: Polycomb complexes in oncogenic 3D genome regulation. Front. Cell Dev. Biol 10, 986319. 10.3389/fcell.2022.986319. [PubMed: 36105358]

20. Chan HL, Beckedorff F, Zhang Y, Garcia-Huidobro J, Jiang H, Colaprico A, Bilbao D, Figueroa ME, LaCava J, Shiekhattar R, et al. (2018). Polycomb complexes associate with enhancers and promote oncogenic transcriptional programs in cancer through multiple mechanisms. Nat. Commun 9, 1–16. 10.1038/s41467-018-05728-x. [PubMed: 29317637]

21. Morey L, Santanach A, Blanco E, Aloia L, Nora EP, Bruneau BG, and Di Croce L (2015). Polycomb Regulates Mesoderm Cell Fate-Specification in Embryonic Stem Cells through Activation and Repression Mechanisms. Cell Stem Cell 17, 300–315. 10.1016/j.stem.2015.08.009. [PubMed: 26340528]

22. Zhang Y, Chan HL, Garcia-Martinez L, Karl DL, Weich N, Slingerland JM, Verdun RE, and Morey L (2020). Estrogen induces dynamic ERα and RING1B recruitment to control gene and enhancer activities in luminal breast cancer. Sci. Adv 6, eaaz7249. 10.1126/sciadv.aaz7249. [PubMed: 32548262]

23. Zhang Y, Liu T, Yuan F, Garcia-Martinez L, Lee KD, Stransky S, Sidoli S, Verdun RE, Zhang Y, Wang Z, et al. (2021). The Polycomb protein RING1B enables estrogen-mediated gene expression by promoting enhancer-promoter interaction and R-loop formation. Nucleic Acids Res. 49, 9768–9782. 10.1093/nar/gkab723. [PubMed: 34428304]

24. Chan HL, and Morey L (2019). Emerging Roles for Polycomb-Group Proteins in Stem Cells and Cancer. Trends Biochem. Sci 44, 688–700. 10.1016/j.tibs.2019.04.005. [PubMed: 31085088]

25. Jangam SV, Briere LC, Jay KL, Andrews JC, Walker MA, Rodan LH, High FA, Undiagnosed Diseases, Network, Yamamoto S, Sweetser DA, and Wangler (2023). A de novo missense

variant in EZH1 associated with developmental delay exhibits functional deficits in *Drosophila melanogaster*. Genetics 224. 10.1093/genetics/iyad110.

26. Cyrus SS, Cohen ASA, Agbahovbe R, Avela K, Yeung KS, Chung BHY, Luk HM, Tkachenko N, Choufani S, Weksberg R, et al. (2019). Rare SUZ12 variants commonly cause an overgrowth phenotype. Am. J. Med. Genet, C 181, 532–547. 10.1002/ajmg.c.31748.
27. Turnpenny PD, Wright MJ, Sloman M, Caswell R, van Essen AJ, Gerkes E, Pfundt R, White SM, Shaul-Lotan N, Carpenter L, et al. (2018). Missense Mutations of the Pro65 Residue of PCGF2 Cause a Recognizable Syndrome Associated with Craniofacial, Neurological, Cardiovascular, and Skeletal Features. Am. J. Hum. Genet 103, 786–793. 10.1016/j.ajhg.2018.09.012. [PubMed: 30343942]
28. Pierce SB, Stewart MD, Gulsuner S, Walsh T, Dhall A, McClellan JM, Klevit RE, and King MC (2018). De novo mutation in RING1 with epigenetic effects on neurodevelopment. Proc. Natl. Acad. Sci. USA 115, 1558–1563. 10.1073/pnas.1721290115. [PubMed: 29386386]
29. Lui JC, Barnes KM, Dong L, Yue S, Graber E, Rapaport R, Dauber A, Nilsson O, and Baron J (2018). Ezh2 Mutations Found in the Weaver Overgrowth Syndrome Cause a Partial Loss of H3K27 Histone Methyltransferase Activity. J. Clin. Endocrinol. Metab 103, 1470–1478. 10.1210/jc.2017-01948. [PubMed: 29244146]
30. Beunders G, van de Kamp J, Vasudevan P, Morton J, Smets K, Kleefstra T, de Munnik SA, Schuurs-Hoeijmakers J, Ceulemans B, Zollino M, et al. (2016). A detailed clinical analysis of 13 patients with AUTS2 syndrome further delineates the phenotypic spectrum and underscores the behavioural phenotype. J. Med. Genet 53, 523–532. 10.1136/jmedgenet-2015-103601. [PubMed: 27075013]
31. Cohen ASA, Tuysuz B, Shen Y, Bhalla SK, Jones SJM, and Gibson WT (2015). A novel mutation in EED associated with overgrowth. J. Hum. Genet 60, 339–342. 10.1038/jhg.2015.26. [PubMed: 25787343]
32. Kalscheuer VM, FitzPatrick D, Tommerup N, Bugge M, Niebuhr E, Neumann LM, Tzschach A, Shoichet SA, Menzel C, Erdogan F, et al. (2007). Mutations in autism susceptibility candidate 2 (AUTS2) in patients with mental retardation. Hum. Genet 121, 501–509. 10.1007/s00439-006-0284-0. [PubMed: 17211639]
33. Luo X, Schoch K, Jangam SV, Bhavana VH, Graves HK, Kansagra S, Jasien JM, Stong N, Keren B, Mignot C, et al. (2021). Rare deleterious de novo missense variants in Rnf2/Ring2 are associated with a neurodevelopmental disorder with unique clinical features. Hum. Mol. Genet 30, 1283–1292. 10.1093/hmg/ddab110. [PubMed: 33864376]
34. Imagawa E, Albuquerque EVA, Isidor B, Mitsuhashi S, Mizuguchi T, Miyatake S, Takata A, Miyake N, Boguszewski MCS, Boguszewski CL, et al. (2018). Novel SUZ12 mutations in Weaver-like syndrome. Clin. Genet 94, 461–466. 10.1111/cge.13415. [PubMed: 30019515]
35. Griffiths S, Loveday C, Zachariou A, Behan LA, Chandler K, Cole T, D'Arrigo S, Dieckmann A, Foster A, Gibney J, et al. (2019). EED and EZH2 constitutive variants: A study to expand the Cohen-Gibson syndrome phenotype and contrast it with Weaver syndrome. Am. J. Med. Genet., A 179, 588–594. 10.1002/ajmg.a.61066. [PubMed: 30793471]
36. Awad S, Al-Dosari MS, Al-Yacoub N, Colak D, Salih MA, Alkuraya FS, and Poizat C (2013). Mutation in PHC1 implicates chromatin remodeling in primary microcephaly pathogenesis. Hum. Mol. Genet 22, 2200–2213. 10.1093/hmg/ddt072. [PubMed: 23418308]
37. Ufartes R, Berger H, Till K, Salinas G, Sturm M, Altmüller J, Nürnberg P, Thiele H, Funke R, Apeshiotis N, et al. (2020). De novo mutations in FBRSL1 cause a novel recognizable malformation and intellectual disability syndrome. Hum. Genet 139, 1363–1379. 10.1007/s00439-020-02175-x. [PubMed: 32424618]
38. Akahira-Azuma M, Tsurusaki Y, Enomoto Y, Mitsui J, and Kurosawa K (2018). Refining the clinical phenotype of Okur-Chung neurodevelopmental syndrome. Hum. Genome Var 5, 18011. 10.1038/hgv.2018.11. [PubMed: 29619237]
39. Russell B, Tan WH, and Graham JM Jr. (1993). Bohring-Opitz Syndrome. In GeneReviews((R)), Adam MP, Feldman J, Mirzaa GM, Pagon RA, Wallace SE, and Amemiya A, eds.
40. Porter JM, Pena LDM, Spillmann RC, Johnson A, and Shashi V (1993). Shashi-Pena Syndrome. In GeneReviews((R)), Adam MP, Feldman J, Mirzaa GM, Pagon RA, Wallace SE, and Amemiya A, eds.

41. Balasubramanian M, and Schirwani S (1993). ASXL3-Related Disorder. In GeneReviews((R)), Adam MP, Feldman J, Mirzaa GM, Pagon RA, Wallace SE, and Amemiya A, eds.
42. Hori K, Shimaoka K, and Hoshino M (2021). AUTS2 Gene: Keys to Understanding the Pathogenesis of Neurodevelopmental Disorders. Cells 11, 11. 10.3390/cells11010011. [PubMed: 35011572]
43. Nakashima M, Tohyama J, Nakagawa E, Watanabe Y, Siew CG, Kwong CS, Yamoto K, Hiraide T, Fukuda T, Kaname T, et al. (2019). Identification of de novo CSNK2A1 and CSNK2B variants in cases of global developmental delay with seizures. J. Hum. Genet 64, 313–322. 10.1038/s10038-018-0559-z. [PubMed: 30655572]
44. Whittaker DE, Riegman KLH, Kasah S, Mohan C, Yu T, Pijuan-Sala B, Hebaishi H, Caruso A, Marques AC, Michetti C, et al. (2017). The chromatin remodeling factor CHD7 controls cerebellar development by regulating reelin expression. J. Clin. Investig 127, 874–887. 10.1172/JCI83408. [PubMed: 28165338]
45. Buchwald G, van der Stoop P, Weichenrieder O, Perrakis A, van Lohuizen M, and Sixma TK (2006). Structure and E3-ligase activity of the Ring-Ring complex of polycomb proteins Bmi1 and Ring1b. EMBO J. 25, 2465–2474. 10.1038/sj.emboj.7601144. [PubMed: 16710298]
46. Bentley ML, Corn JE, Dong KC, Phung Q, Cheung TK, and Cochran AG (2011). Recognition of UbcH5c and the nucleosome by the Bmi1/Ring1b ubiquitin ligase complex. EMBO J. 30, 3285–3297. 10.1038/emboj.2011.243. [PubMed: 21772249]
47. Li Z, Cao R, Wang M, Myers MP, Zhang Y, and Xu RM (2006). Structure of a Bmi-1-Ring1B polycomb group ubiquitin ligase complex. J. Biol. Chem 281, 20643–20649. 10.1074/jbc.M602461200. [PubMed: 16714294]
48. McGinty RK, Henrici RC, and Tan S (2014). Crystal structure of the PRC1 ubiquitylation module bound to the nucleosome. Nature 514, 591–596. 10.1038/nature13890. [PubMed: 25355358]
49. Bibel M, Richter J, Lacroix E, and Barde YA (2007). Generation of a defined and uniform population of CNS progenitors and neurons from mouse embryonic stem cells. Nat. Protoc 2, 1034–1043. 10.1038/nprot.2007.147. [PubMed: 17546008]
50. Endoh M, Endo TA, Endoh T, Fujimura Y, Ohara O, Toyoda T, Otte AP, Okano M, Brockdorff N, Vidal M, et al. (2008). Polycomb group proteins Ring1A/B are functionally linked to the core transcriptional regulatory circuitry to maintain ES cell identity. Development 135, 1513–1524. 10.1242/dev.014340. [PubMed: 18339675]
51. Blackledge NP, Fursova NA, Kelley JR, Huseyin MK, Feldmann A, and Klose RJ (2020). PRC1 Catalytic Activity Is Central to Polycomb System Function. Mol. Cell 77, 857–874.e9. 10.1016/j.molcel.2019.12.001. [PubMed: 31883950]
52. Tamburri S, Lavarone E, Fernández-Pérez D, Conway E, Zanotti M, Manganaro D, and Pasini D (2019). Histone H2AK119 Mono-Ubiquitination Is Essential for Polycomb-Mediated Transcriptional Repression. Mol. Cell 77, 840–856.e845. 10.1016/j.molcel.2019.11.021. [PubMed: 31883952]
53. Hur EM, and Zhou FQ (2010). GSK3 signalling in neural development. Nat. Rev. Neurosci 11, 539–551. 10.1038/nrn2870. [PubMed: 20648061]
54. Guillemot F (2007). Spatial and temporal specification of neural fates by transcription factor codes. Development 134, 3771–3780. 10.1242/dev.006379. [PubMed: 17898002]
55. Israsena N, Hu M, Fu W, Kan L, and Kessler JA (2004). The presence of FGF2 signaling determines whether beta-catenin exerts effects on proliferation or neuronal differentiation of neural stem cells. Dev. Biol 268, 220–231. 10.1016/j.ydbio.2003.12.024. [PubMed: 15031118]
56. Qian X, Shen Q, Goderie SK, He W, Capela A, Davis AA, and Temple S (2000). Timing of CNS cell generation: a programmed sequence of neuron and glial cell production from isolated murine cortical stem cells. Neuron 28, 69–80. 10.1016/s0896-6273(00)00086-6. [PubMed: 11086984]
57. Chen G, Shaw MH, Kim YG, and Nuñez G (2009). NOD-like receptors: role in innate immunity and inflammatory disease. Annu. Rev. Pathol 4, 365–398. 10.1146/annurev.pathol.4.110807.092239. [PubMed: 18928408]
58. Isono K, Endo TA, Ku M, Yamada D, Suzuki R, Sharif J, Ishikura T, Toyoda T, Bernstein BE, and Koseki H (2013). SAM domain polymerization links subnuclear clustering of PRC1 to gene silencing. Dev. Cell 26, 565–577. 10.1016/j.devcel.2013.08.016. [PubMed: 24091011]

59. Wani AH, Boettiger AN, Schorderet P, Ergun A, Münger C, Sadreyev RI, Zhuang X, Kingston RE, and Francis NJ (2016). Chromatin topology is coupled to Polycomb group protein subnuclear organization. Nat. Commun 7, 10291. 10.1038/ncomms10291. [PubMed: 26759081]

60. Bergsland M, Ramsköld D, Zaouter C, Klum S, Sandberg R, and Muhr J (2011). Sequentially acting Sox transcription factors in neural lineage development. Genes Dev. 25, 2453–2464. 10.1101/gad.176008.111. [PubMed: 22085726]

61. Episkopou V. (2005). SOX2 functions in adult neural stem cells. Trends Neurosci. 28, 219–221. 10.1016/j.tins.2005.03.003. [PubMed: 15866195]

62. Okumura-Nakanishi S, Saito M, Niwa H, and Ishikawa F (2005). Oct-3/4 and Sox2 regulate Oct-3/4 gene in embryonic stem cells. J. Biol. Chem 280, 5307–5317. 10.1074/jbc.M410015200. [PubMed: 15557334]

63. Masui S, Nakatake Y, Toyooka Y, Shimosato D, Yagi R, Takahashi K, Okochi H, Okuda A, Matoba R, Sharov AA, et al. (2007). Pluripotency governed by Sox2 via regulation of Oct3/4 expression in mouse embryonic stem cells. Nat. Cell Biol 9, 625–635. 10.1038/ncb1589. [PubMed: 17515932]

64. Sarkar A, and Hochedlinger K (2013). The sox family of transcription factors: versatile regulators of stem and progenitor cell fate. Cell Stem Cell 12, 15–30. 10.1016/j.stem.2012.12.007. [PubMed: 23290134]

65. Voncken JW, Roelen BAJ, Roefs M, de Vries S, Verhoeven E, Marino S, Deschamps J, and van Lohuizen M (2003). Rnf2 (Ring1b) deficiency causes gastrulation arrest and cell cycle inhibition. Proc. Natl. Acad. Sci. USA 100, 2468–2473. 10.1073/pnas.0434312100. [PubMed: 12589020]

66. Illingworth RS, Moffat M, Mann AR, Read D, Hunter CJ, Pradeepa MM, Adams IR, and Bickmore WA (2015). The E3 ubiquitin ligase activity of RING1B is not essential for early mouse development. Genes Dev. 29, 1897–1902. 10.1101/gad.268151.115. [PubMed: 26385961]

67. Euston DR, Gruber AJ, and McNaughton BL (2012). The role of medial prefrontal cortex in memory and decision making. Neuron 76, 1057–1070. 10.1016/j.neuron.2012.12.002. [PubMed: 23259943]

68. Yang Y, and Wang JZ (2017). From Structure to Behavior in Basolateral Amygdala-Hippocampus Circuits. Front. Neural Circuits 11, 86. 10.3389/fncir.2017.00086. [PubMed: 29163066]

69. Herrmann L, Ionescu IA, Henes K, Golub Y, Wang NXR, Buell DR, Holsboer F, Wotjak CT, and Schmidt U (2012). Long-lasting hippocampal synaptic protein loss in a mouse model of posttraumatic stress disorder. PLoS One 7, e42603. 10.1371/journal.pone.0042603. [PubMed: 22900032]

70. Ghasemi M, Navidhamidi M, Rezaei F, Azizikia A, and Mehranfard N (2022). Anxiety and hippocampal neuronal activity: Relationship and potential mechanisms. Cogn. Affect. Behav. Neurosci 22, 431–449. 10.3758/s13415-021-00973-y. [PubMed: 34873665]

71. Etkin A, Egner T, and Kalisch R (2011). Emotional processing in anterior cingulate and medial prefrontal cortex. Trends Cogn. Sci 15, 85–93. 10.1016/j.tics.2010.11.004. [PubMed: 21167765]

72. Dennis DJ, Han S, and Schuurmans C (2019). bHLH transcription factors in neural development, disease, and reprogramming. Brain Res. 1705, 48–65. 10.1016/j.brainres.2018.03.013. [PubMed: 29544733]

73. Chahrour M, Jung SY, Shaw C, Zhou X, Wong STC, Qin J, and Zoghbi HY (2008). MeCP2, a key contributor to neurological disease, activates and represses transcription. Science 320, 1224–1229. 10.1126/science.1153252. [PubMed: 18511691]

74. Zhao J, Lan J, Wang M, Liu C, Fang Z, Song A, Zhang T, Wang L, Zhu B, Chen P, et al. (2024). H2AK119ub1 differentially fine-tunes gene expression by modulating canonical PRC1- and H1-dependent chromatin compaction. Mol. Cell 84, 1191–1205.e7. 10.1016/j.molcel.2024.02.017. [PubMed: 38458202]

75. Glancy E, Wang C, Tuck E, Healy E, Amato S, Neikes HK, Mariani A, Mucha M, Vermeulen M, Pasini D, et al. (2023). PRC2.1- and PRC2.2-specific accessory proteins drive recruitment of different forms of canonical PRC1. Mol. Cell 83, 1393–1411.e7. 10.1016/j.molcel.2023.03.018. [PubMed: 37030288]

76. López VG, Valencia-Sánchez MI, Abini-Agbomson S, Thomas JF, Lee R, De Ioannes P, Sosa BA, Armache JP, and Armache KJ (2024). Read-write mechanisms of H2A ubiquitination by

Polycomb repressive complex 1. Nature 636, 755–761. 10.1038/s41586-024-08183-5. [PubMed: 39537923]

77. Sansom SN, Griffiths DS, Faedo A, Kleinjan DJ, Ruan Y, Smith J, van Heyningen V, Rubenstein JL, and Livesey FJ (2009). The level of the transcription factor Pax6 is essential for controlling the balance between neural stem cell self-renewal and neurogenesis. PLoS Genet. 5, e1000511. 10.1371/journal.pgen.1000511. [PubMed: 19521500]
78. Nusse R. (2008). Wnt signaling and stem cell control. Cell Res. 18, 523–527. 10.1038/cr.2008.47. [PubMed: 18392048]
79. Borzello M, Ramirez S, Treves A, Lee I, Scharfman H, Stark C, Knierim JJ, and Rangel LM (2023). Assessments of dentate gyrus function: discoveries and debates. Nat. Rev. Neurosci 24, 502–517. 10.1038/s41583-023-00710-z. [PubMed: 37316588]
80. Eto H, Kishi Y, Yakushiji-Kaminatsui N, Sugishita H, Utsunomiya S, Koseki H, and Gotoh Y (2020). The Polycomb group protein Ring1 regulates dorsoventral patterning of the mouse telencephalon. Nat. Commun 11, 5709. 10.1038/s41467-020-19556-5. [PubMed: 33177537]
81. Tsuboi M, Kishi Y, Yokozeki W, Koseki H, Hirabayashi Y, and Gotoh Y (2018). Ubiquitination-Independent Repression of PRC1 Targets during Neuronal Fate Restriction in the Developing Mouse Neocortex. Dev. Cell 47, 758–772.e5. 10.1016/j.devcel.2018.11.018. [PubMed: 30562514]
82. Morimoto-Suzki N, Hirabayashi Y, Tyssowski K, Shinga J, Vidal M, Koseki H, and Gotoh Y (2014). The polycomb component Ring1B regulates the timed termination of subcerebral projection neuron production during mouse neocortical development. Development 141, 4343–4353. 10.1242/dev.112276. [PubMed: 25344075]
83. Jumper J, Evans R, Pritzel A, Green T, Figurnov M, Ronneberger O, Tunyasuvunakool K, Bates R, Žídek A, Potapenko A, et al. (2021). Highly accurate protein structure prediction with AlphaFold. Nature 596, 583–589. 10.1038/s41586-021-03819-2. [PubMed: 34265844]
84. Abramson J, Adler J, Dunger J, Evans R, Green T, Pritzel A, Ronneberger O, Willmore L, Ballard AJ, Bambrick J, et al. (2024). Accurate structure prediction of biomolecular interactions with AlphaFold 3. Nature 630, 493–500. 10.1038/s41586-024-07487-w. [PubMed: 38718835]
85. Mirdita M, Schütze K, Moriwaki Y, Heo L, Ovchinnikov S, and Steinegger M (2022). ColabFold: making protein folding accessible to all. Nat. Methods 19, 679–682. 10.1038/s41592-022-01488-1. [PubMed: 35637307]
86. Zhang N, Chen Y, Lu H, Zhao F, Alvarez RV, Goncearenco A, Panchenko AR, and Li M (2020). MutaBind2: Predicting the Impacts of Single and Multiple Mutations on Protein-Protein Interactions. iScience 23, 100939. 10.1016/j.isci.2020.100939. [PubMed: 32169820]
87. Ewels PA, Peltzer A, Fillinger S, Patel H, Alneberg J, Wilm A, Garcia MU, Di Tommaso P, and Nahnsen S (2020). The nf-core framework for community-curated bioinformatics pipelines. Nat. Biotechnol 38, 276–278. 10.1038/s41587-020-0439-x. [PubMed: 32055031]
88. Ramírez F, Dündar F, Diehl S, Grüning BA, and Manke T (2014). deepTools: a flexible platform for exploring deep-sequencing data. Nucleic Acids Res. 42, W187–W191. 10.1093/nar/gku365. [PubMed: 24799436]
89. Li H, Handsaker B, Wysoker A, Fennell T, Ruan J, Homer N, Marth G, Abecasis G, and Durbin R; 1000 Genome Project Data Processing Subgroup (2009). The Sequence Alignment/Map format and SAMtools. Bioinformatics 25, 2078–2079. 10.1093/bioinformatics/btp352. [PubMed: 19505943]
90. Ewels P, Magnusson M, Lundin S, and Käller M (2016). MultiQC: summarize analysis results for multiple tools and samples in a single report. Bioinformatics 32, 3047–3048. 10.1093/bioinformatics/btw354. [PubMed: 27312411]
91. Langmead B, and Salzberg SL (2012). Fast gapped-read alignment with Bowtie 2. Nat. Methods 9, 357–359. 10.1038/nmeth.1923. [PubMed: 22388286]
92. Xu S, Hu E, Cai Y, Xie Z, Luo X, Zhan L, Tang W, Wang Q, Liu B, Wang R, et al. (2024). Using clusterProfiler to characterize multiomics data. Nat. Protoc 19, 3292–3320. 10.1038/s41596-024-01020-z. [PubMed: 39019974]
93. Quinlan AR, and Hall IM (2010). BEDTools: a flexible suite of utilities for comparing genomic features. Bioinformatics 26, 841–842. 10.1093/bioinformatics/btq033. [PubMed: 20110278]

94. Satija R, Farrell JA, Gennert D, Schier AF, and Regev A (2015). Spatial reconstruction of single-cell gene expression data. Nat. Biotechnol 33, 495–502. 10.1038/nbt.3192. [PubMed: 25867923]
95. Stuart T, Srivastava A, Madad S, Lareau CA, and Satija R (2021). Single-cell chromatin state analysis with Signac. Nat. Methods 18, 1333–1341. 10.1038/s41592-021-01282-5. [PubMed: 34725479]
96. Zhou H, Stein CB, Shafiq TA, Shipkovenska G, Kalocsay M, Paulo JA, Zhang J, Luo Z, Gygi SP, Adelman K, et al. (2022). Rixosomal RNA degradation contributes to silencing of Polycomb target genes. Nature 604, 167–174. 10.1038/s41586-022-04598-0. [PubMed: 35355014]
97. Stiernagle T. (2006). Maintenance of C. elegans. WormBook, 1–11. 10.1895/wormbook.1.101.1.
98. Brenner S. (1974). The genetics of Caenorhabditis elegans. Genetics 77, 71–94. 10.1093/genetics/77.1.71. [PubMed: 4366476]
99. Norris AD, Kim HM, Colaiácovo MP, and Calarco JA (2015). Efficient Genome Editing in Caenorhabditis elegans with a Toolkit of Dual-Marker Selection Cassettes. Genetics 201, 449–458. 10.1534/genetics.115.180679. [PubMed: 26232410]
100. Martin CJ, and Calarco JA (2022). Approaches for CRISPR/Cas9 Genome Editing in C. elegans. Methods Mol. Biol 2468, 215–237. 10.1007/978-1-0716-2181-3_11. [PubMed: 35320567]
101. Paix A, Folkmann A, Rasoloson D, and Seydoux G (2015). High Efficiency, Homology-Directed Genome Editing in Caenorhabditis elegans Using CRISPR-Cas9 Ribonucleoprotein Complexes. Genetics 201, 47–54. 10.1534/genetics.115.179382. [PubMed: 26187122]
102. Anderson KGV, Hamilton WB, Roske FV, Azad A, Knudsen TE, Canham MA, Forrester LM, and Brickman JM (2017). Insulin fine-tunes self-renewal pathways governing naive pluripotency and extra-embryonic endoderm. Nat. Cell Biol 19, 1164–1177. 10.1038/ncb3617. [PubMed: 28945231]
103. Kurtzer GM, Sochat V, and Bauer MW (2017). Singularity: Scientific containers for mobility of compute. PLoS One 12, e0177459. 10.1371/journal.pone.0177459. [PubMed: 28494014]
104. McGinnis CS, Murrow LM, and Gartner ZJ (2019). DoubletFinder: Doublet Detection in Single-Cell RNA Sequencing Data Using Artificial Nearest Neighbors. Cell Syst. 8, 329–337.e4. 10.1016/j.cels.2019.03.003. [PubMed: 30954475]
105. Ianevski A, Giri AK, and Aittokallio T (2022). Fully-automated and ultra-fast cell-type identification using specific marker combinations from single-cell transcriptomic data. Nat. Commun 13, 1246. 10.1038/s41467-022-28803-w. [PubMed: 35273156]
106. Franzen O, Gan LM, and Bjorkegren JLM (2019). PanglaoDB: a web server for exploration of mouse and human single-cell RNA sequencing data. Database. 10.1093/database/baz046.
107. Phipson B, Sim CB, Porrello ER, Hewitt AW, Powell J, and Oshlack A (2022). propeller: testing for differences in cell type proportions in single cell data. Bioinformatics 38, 4720–4726. 10.1093/bioinformatics/btac582. [PubMed: 36005887]
108. Bhattacherjee A, Zhang C, Watson BR, Djekidel MN, Moffitt JR, and Zhang Y (2023). Spatial transcriptomics reveals the distinct organization of mouse prefrontal cortex and neuronal subtypes regulating chronic pain. Nat. Neurosci 26, 1880–1893. 10.1038/s41593-023-01455-9. [PubMed: 37845544]
109. Bhattacherjee A, Djekidel MN, Chen R, Chen W, Tuesta LM, and Zhang Y (2019). Cell type-specific transcriptional programs in mouse prefrontal cortex during adolescence and addiction. Nat. Commun. 10, 4169. 10.1038/s41467-019-12054-3. [PubMed: 31519873]
110. Moy SS, Nadler JJ, Perez A, Barbaro RP, Johns JM, Magnuson TR, Piven J, and Crawley JN (2004). Sociability and preference for social novelty in five inbred strains: an approach to assess autistic-like behavior in mice. Genes Brain Behav. 3, 287–302. 10.1111/j.1601-1848.2004.00076.x. [PubMed: 15344922]
111. Molina J, Carmona-Mora P, Chrast J, Krall PM, Canales CP, Lupski JR, Reymond A, and Walz K (2008). Abnormal social behaviors and altered gene expression rates in a mouse model for Potocki-Lupski syndrome. Hum. Mol. Genet 17, 2486–2495. 10.1093/hmg/ddn148. [PubMed: 18469339]
112. Rein B, Ma K, and Yan Z (2020). A standardized social preference protocol for measuring social deficits in mouse models of autism. Nat. Protoc 15, 3464–3477. 10.1038/s41596-020-0382-9. [PubMed: 32895524]

113. Tournier JD, Smith R, Raffelt D, Tabbara R, Dhollander T, Pietsch M, Christiaens D, Jeurissen B, Yeh CH, and Connelly A (2019). MRtrix3: A fast, flexible and open software framework for medical image processing and visualisation. Neuroimage 202, 116137. 10.1016/j.neuroimage.2019.116137. [PubMed: 31473352]

114. Smith SM (2002). Fast robust automated brain extraction. Hum. Brain Mapp 17, 143–155. 10.1002/hbm.10062. [PubMed: 12391568]

115. Sievers F, Wilm A, Dineen D, Gibson TJ, Karplus K, Li W, Lopez R, McWilliam H, Remmert M, Söding J, et al. (2011). Fast, scalable generation of high-quality protein multiple sequence alignments using Clustal Omega. Mol. Syst. Biol 7, 539. 10.1038/msb.2011.75. [PubMed: 21988835]

116. Schindelin J, Arganda-Carreras I, Frise E, Kaynig V, Longair M, Pietzsch T, Preibisch S, Rueden C, Saalfeld S, Schmid B, et al. (2012). Fiji: an open-source platform for biological-image analysis. Nat. Methods 9, 676–682. 10.1038/nmeth.2019. [PubMed: 22743772]

Highlights

- Discovery of novel missense mutations in *RNF2* and *RING1* linked to NDDs
- $Rnf2^{R70H}$ disrupts the balance of Polycomb complexes co-occupancy at chromatin in ESCs
- $Rnf2^{R70H/R70H}$ mice are lethal, and $Rnf2^{WT/R70H}$ mice display brain architectural deficits
- Impaired social novelty preference and increased anxiety in $Rnf2^{WT/R70H}$ mice

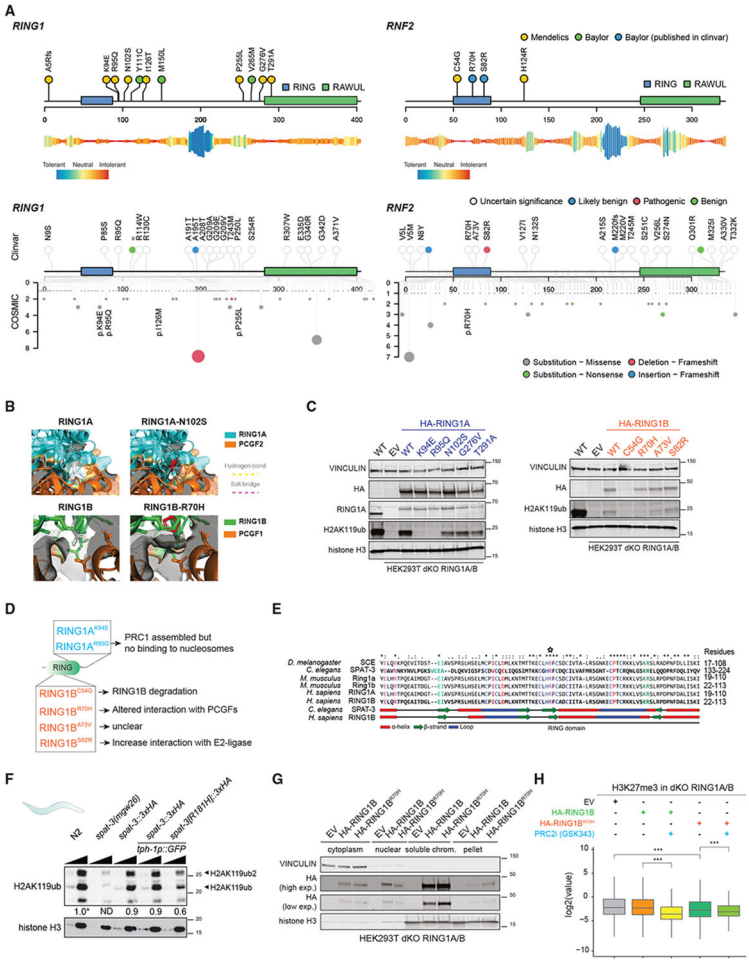

Figure 1. Missense mutations in *RING1* and *RNF2* in individuals with ID and their biochemical characterization

(A) *RING1* and *RNF2* variants (top). Reported variants in ClinVar and cancer-related somatic (COSMIC) mutations in *RING1* and *RNF2* genes (bottom). Metadome plots (middle) represent the level of predicted intolerance for amino acid change in RING1A and RING1B. For COSMIC, only positions of interest are shown as labels. Circle size represents the number of patients reported.

(B) ColabFold predictions of RING1A and RING1B variants in altering interaction with PCGF proteins.

(C) WBs of dKO-RING1A/B cells expressing HA-tagged WT and mutant RING1A and RING1B. Vinculin and histone H3 served as loading controls. $n = 3$ independent experimental replicates.

(D) Possible mechanisms of deleterious variants that result in a decrease or absence of H2AK119ub.

(E) Partial protein sequence alignments of a subset of RING1B homologs. The conserved RING1B-R70 residue corresponds to *C. elegans* R181 and is indicated by a star. Conserved zinc-coordinating residues, blue[45]; required for stabilizing the E2 enzyme-E3 ligase interaction in mammals, red[46]; required for binding to the nucleosome in mammals, green[46] predicted to be important for the RING1B:PCGF4 interaction, magenta 47; and predicted to

mediate β sheet interactions, cyan. * indicates identical residues, and : and. indicate residues with strongly and weakly similar physicochemical properties, respectively. The secondary structure of SPAT-3 and *H. sapiens* RING1B is shown below.

(F) WBs of H2AK119ub in the indicated genotypes. The dilution factor is 1:3. The *spat-3(mgw26)* allele is a full deletion of the *spat-3* coding region. Quantification of H2AK119ub and SPAT-3 isoform A is normalized to loading controls (histone H3/actin) and shown relative to the sample indicated by an asterisk. ND, not detectable.

(G) WBs in dKO-RING1A/B cells stably expressing HA-RING1B^{WT} or HA-RING1B^{R70H}. Vinculin and histone H2A and H3 served as fractionation controls. $n = 3$ independent experimental replicates.

(H) Normalized H3K27me3 Cut&Run signal (two independent experimental replicates) in cells treated with 1 μM of vehicle (DMSO) or GSK343 for 72 h. See also Figures S1 and S2.

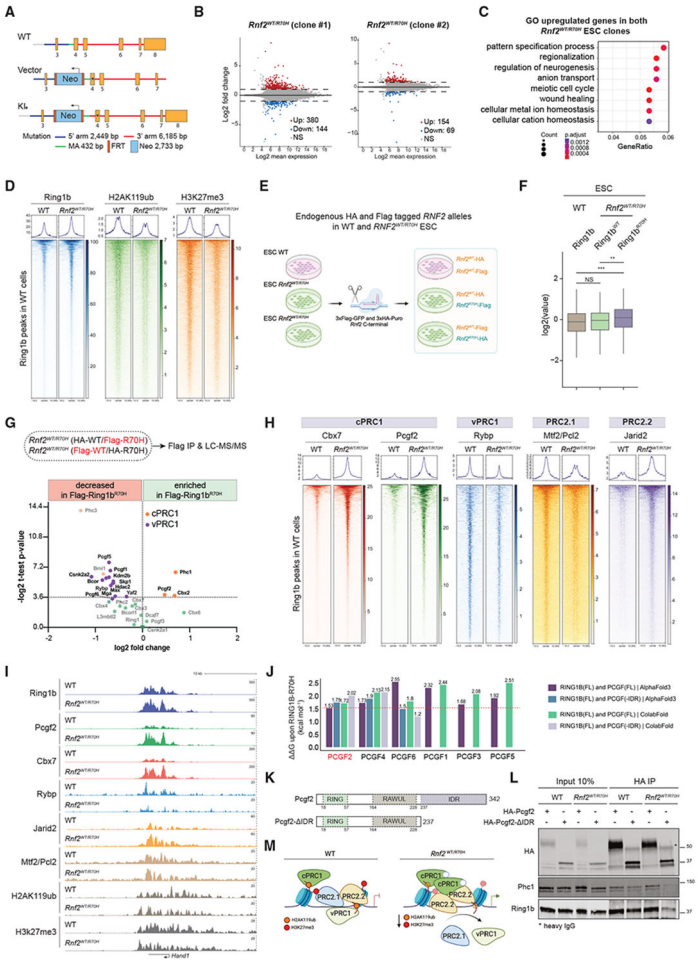

Figure 2. Transcriptome of *Rnf2*$^{WT/R70H}$ ESCs, allele-specific Ring1b interactome, and PRC1/2 complex occupancy

(A) Strategy to generate *Rnf2*$^{WT/R70H}$ ESCs by homologous recombination.

(B) DEG from WT and two clones of *Rnf2*$^{WT/R70H}$ ESCs ($\log_2$ fold > 2, $q < 0.01$). $n = 2$ independent experimental replicates.

(C) GO of upregulated genes in *Rnf2*$^{WT/R70H}$ ESCs.

(D) Heatmaps of Ring1b, H3K27me3, and H2AK119ub ChIP-seq (average signal of two independent experimental replicates) in WT and clone #1 of *Rnf2*$^{WT/R70H}$ ESCs.

(E) Strategy to generate HA and FLAG-tagged *Rnf2* alleles by CRISPR-Cas9 in WT and *Rnf2*$^{WT/R70H}$ ESCs.

(F) Normalized Ring1b^{WT} and Ring1b^{R70H} Cut&Run signals in WT and *Rnf2*$^{WT/R70H}$ ESCs. Signal was generated from two biological replicates from two independent WT and *Rnf2*$^{WT/R70H}$ clones. HA and FLAG Cut&Run signals were merged (average of 4 replicates) to avoid potential bias from the HA and FLAG antibodies' efficiency.

(G) Anti-FLAG IPs in *Rnf2*$^{HA\text{-}WT/FLAG\text{-}R70H}$ and *Rnf2*$^{FLAG\text{-}WT/HA\text{-}R70H}$ ESCs followed by LC-MS/MS in three independent experimental replicates. Results are normalized to IgG as a negative control. Volcano plot shows proteins enriched or weakened in FLAG-Ring1b^{R70H} compared with FLAG-Ring1b^{WT} from *Rnf2*$^{WT/R70H}$ ESCs.

(H) Heatmaps of Cbx7 and Pcgf2, Rybp, Mtf2/Pcl2, and Jarid2 ChIP-seq (average signal of two independent experimental replicates) in WT and clone #1 of *Rnf2*$^{WT/R70H}$ ESCs.
(I) Genome browser screenshots of ChIP-seq from (H).
(J) Mutabind2 scores upon the human RING1B^{R70H} variant vs. full length and lacking their IDR, PCGF1-6 using AlphaFold and ColabFold.
(K) Full-length Pcgf2 or lacking the IDR used in (L).
(L) Anti-HA IPs followed by WBs against HA, Phc1, and Ring1b in WT and *Rnf2*$^{WT/R70H}$ ESCs expressing HA-Pcgf2^{WT} or HA-Pcgf2$^{\Delta IDR}$.
(M) Model of PRC1/2 recruitment in *Rnf2*$^{WT/R70H}$ ESCs.
See also Figure S3.

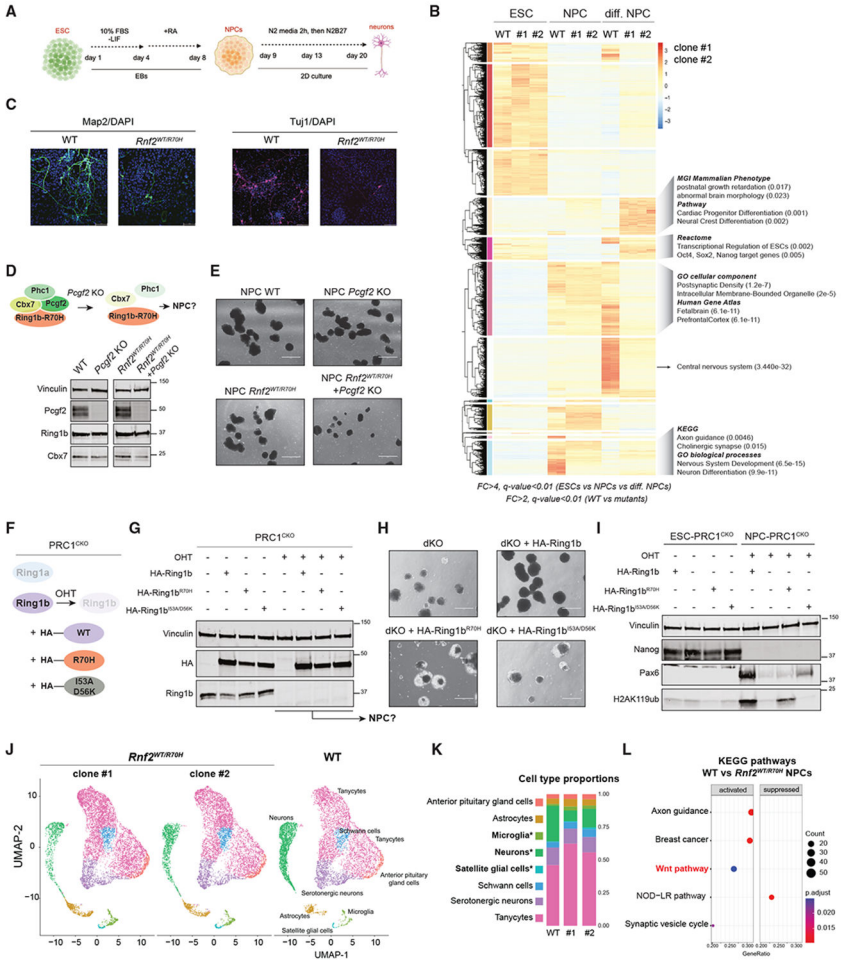

Figure 3. Cell fate change of *Rnf2*$^{WT/R70H}$ NPCs into glial and microglia cells

(A) Protocol to generate and differentiate NPCs.

(B) Heatmap of DEG from ESCs vs. NPCs vs. differentiated NPCs ($\log_2$fold > 4, q < 0.01) and between WT and two clones of *Rnf2*$^{WT/R70H}$ ESCs, NPCs, and 12-day-old differentiated NPCs ($\log_2$fold > 2, q < 0.01). n = 2 independent experimental replicates.

(C) IFs of neuronal markers in WT and *Rnf2*$^{WT/R70H}$ differentiated NPCs. n = 3 independent experimental replicates. Scale bar, 10 μm.

(D) WBs of PRC1 subunits from WT ESCs and *Pcgf2* KO and *Rnf2*$^{WT/R70H}$ with and without *Pcgf2*.

(E) Pictures of NPCs derived from cells in (D). n = 4 independent experimental replicates. Scale bar, 400 μm.

(F) Strategy to generate NPCs expressing Ring1b^{WT}, Ring1b^{R70H}, or Ring1b$^{I53A/D56K}$ in PRC1^{CKO} cells.

(G) WBs of HA and Ring1b in PRC1^{CKO} cells expressing Ring1b^{WT}, Ring1b^{R70H}, or Ring1b$^{I53A/D56K}$ in the presence and absence of OHT treatment for 48 h. Vinculin was used as a loading control.

(H) Pictures of NPCs derived from cells in (G) in a constant presence of OHT treatment. n = 2. Scale bar, 400 μm.

(I) WBs of Nanog, Pax6, and H2AK119ub in NPCs derived from $PRC1^{CKO}$ cells expressing $Ring1b^{WT}$, $Ring1b^{R70H}$, or $Ring1b^{I53A/D56K}$. Vinculin was used as a loading control.
(J) UMAP plots of scRNA-seq from 16-day-old WT and two clones of $Rnf2^{WT/R70H}$ differentiated NPCs. $n = 2$ independent experimental replicates.
(K) Cell type proportions of cells from (E). $*p < 0.05$. ANOVA test.
(L) KEGG pathway of WT and two clones of $Rnf2^{WT/R70H}$ NPCs.
See also Figure S4.

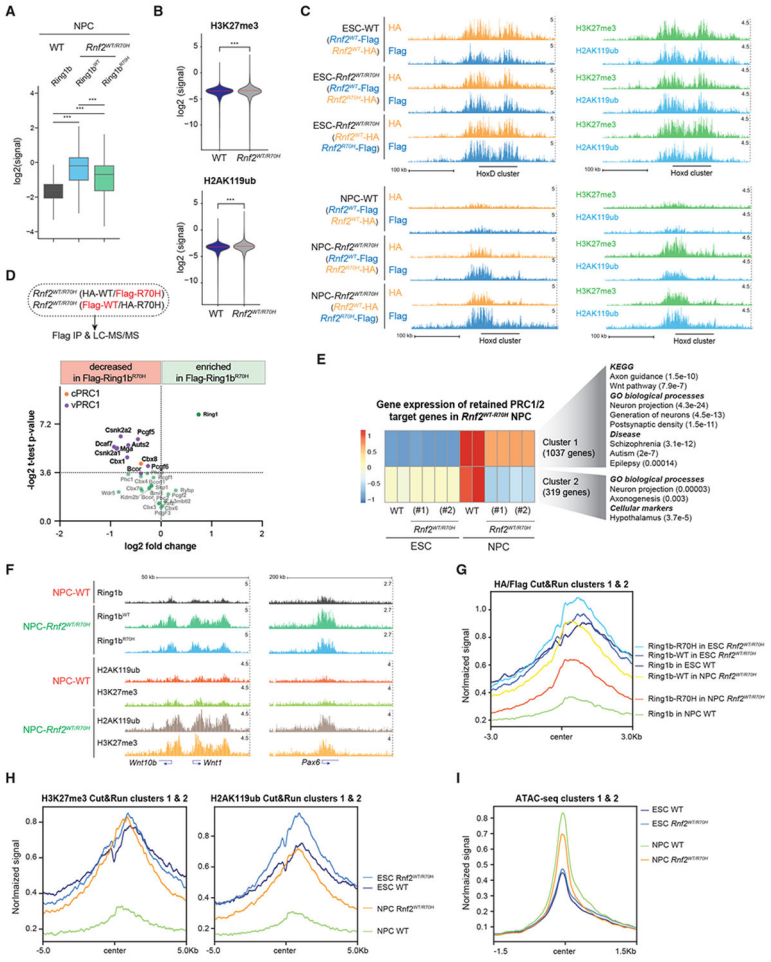

Figure 4. WT and mut-PRC1 and PRC2 are retained at key neurogenesis genes to repress them by chromatin compaction and their enzymatic activities

(A) Normalized Ring1b^{WT} and Ring1b^{R70H} Cut&Run signals in either WT or *Rnf2*$^{WT/R70H}$ NPCs in WT Ring1b peak regions. Two biological replicates from two independent clones. Wilcox test. ***$p < 0.001$.

(B) Normalized H3K27me3 and H2AK119ub Cut&Run signals in either WT or *Rnf2*$^{WT/R70H}$ NPCs over all genome. Signal was generated from two biological replicates from two independent clones. Wilcox test. ***$p < 0.001$.

(C) Genome browser screenshots of HA, FLAG, H3K27me3, and H2AK119ub Cut&Run (average signal between replicates) in the cells shown on the left.

(D) Anti-FLAG IPs in *Rnf2*$^{HA\text{-}WT/FLAG\text{-}R70H}$ and *Rnf2*$^{FLAG\text{-}WT/HA\text{-}R70H}$ NPCs followed by LC-MS/MS in three independent experimental replicates. Results are normalized to IgG as negative control. Volcano plot shows proteins enriched or weakened in FLAG-Ring1b^{R70H} compared with FLAG-Ring1b^{WT} from *Rnf2*$^{WT/R70H}$ NPCs.

(E) RNA-seq heatmap of PcG target genes in ESCs that are upregulated in WT NPCs but retained PRC1/2 and are repressed in *Rnf2*$^{WT/R70H}$ NPCs. #1 and #2 are two different *Rnf2*$^{WT/R70H}$ ESC clones. On the right, GO from each cluster. Deseq2; Wald test (FC > 4), $q < 0.05$.

(F) Simplified genome browser screenshots of Ring1b^{WT}, Ring1b^{R70H}, H3K27me3, and H2AK119ub Cut&Run in WT and *Rnf2*$^{WT/R70H}$ NPCs. Ring1b signal in WT NPCs and Ring1b^{WT} and Ring1b^{R70H} signals in *Rnf2*$^{WT/R70H}$ NPCs are from merging average signals HA and FLAG Cut&Run two replicates from two clones.
(G) Normalized signal of Ring1b^{WT} and Ring1b^{R70H} Cut&Run signals as in (F) around the transcription start site (TSS) of genes from (E).
(H) Normalized signal of H3K27me3 and H2AK119ub Cut&Run signals (average from two replicates) as in (F) around the TSS of genes from (E).
(I) Normalized ATAC-seq signal (average from two replicates) in WT and *Rnf2*$^{WT/R70H}$ ESCs and NPCs around the TSS of genes from (E).
See also Figure S5.

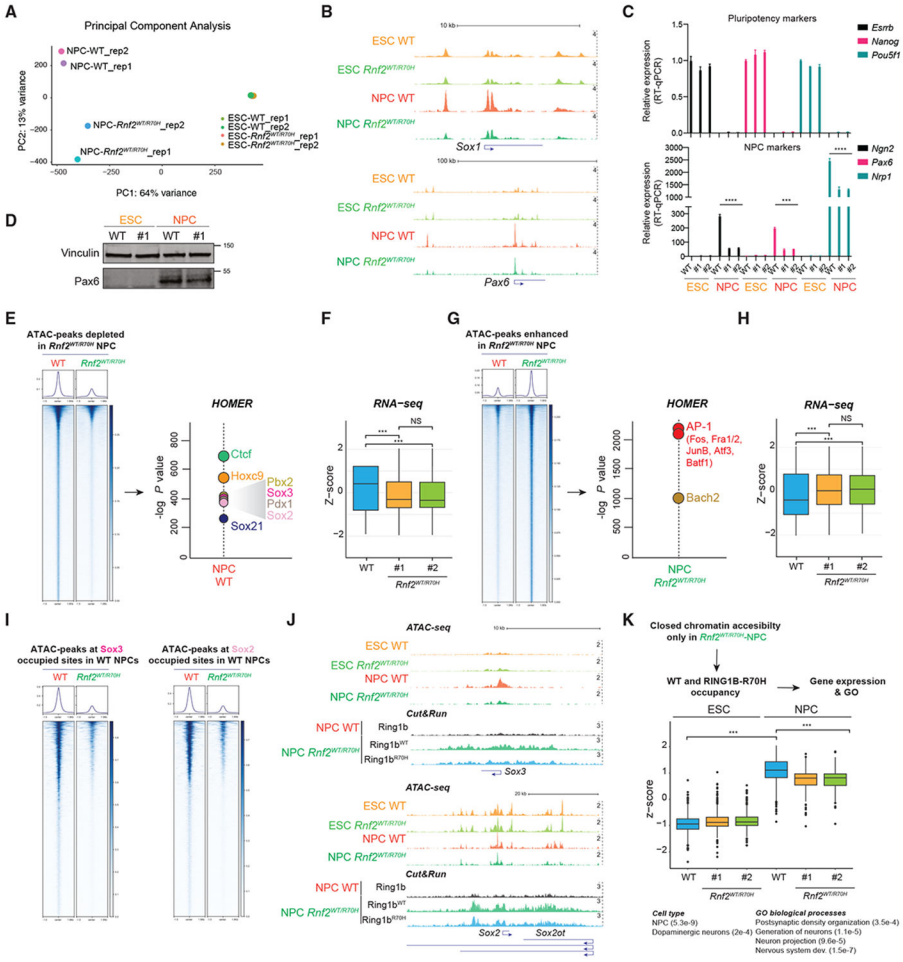

Figure 5. Ring1b^{R70H} impairs chromatin accessibility by repressing *Sox2* and *Sox3* expression

(A) PCA from ATAC-seq from two independent biological replicates of WT and *Rnf2*$^{WT/R70H}$ ESCs and NPCs.

(B) Genome browser of ATAC-seq signal (average of two replicates) from WT and *Rnf2*$^{WT/R70H}$ ESCs and NPCs.

(C) RT-qPCR of pluripotency genes and NPC markers in WT and *Rnf2*$^{WT/R70H}$ ESCs and NPCs. $n = 3$. #1 and #2 represent two clones of *Rnf2*$^{WT/R70H}$ ESCs. ***$p < 0.005$, ****$p < 0.001$ by ANOVA test.

(D) WB of Pax6 in WT and clone #1 of *Rnf2*$^{WT/R70H}$ ESCs and NPCs. Vinculin served as a loading control.

(E) ATAC-seq peaks reduced in *Rnf2*$^{WT/R70H}$ NPCs and HOMER analysis.

(F) Normalized expression of genes from (E) in WT and clones #1 and #2 of *Rnf2*$^{WT/R70H}$ NPCs. ***$p < 0.001$. NS, not significant. Wilcox test.

(G) ATAC-seq specific peaks in *Rnf2*$^{WT/R70H}$ NPCs and HOMER analysis.

(H) Normalized expression of genes from (G) in WT and clones #1 and #2 of *Rnf2*$^{WT/R70H}$ NPCs. ***$p < 0.001$. NS, not significant. Wilcox test.

(I) ATAC-seq signal in WT and *Rnf2*$^{WT/R70H}$ NPCs at Sox2- or Sox3-occupied sites in WT NPCs. Sox2 and Sox3 ChIP from Bergsland et al.[60]

(J) Genome browser of ATAC-seq signal from WT and *Rnf2*$^{WT/R70H}$ ESCs and NPCs as well as Ring1b^{WT} and Ring1b^{R70H} Cut&Run signal in WT and *Rnf2*$^{WT/R70H}$ NPCs.
(K) Normalized expression and GO of genes occupied by Ring1b^{WT} and Ring1b^{R70H} and compacted. ***$p < 0.001$. NS, not significant. Wilcox test.
See also Figure S6.

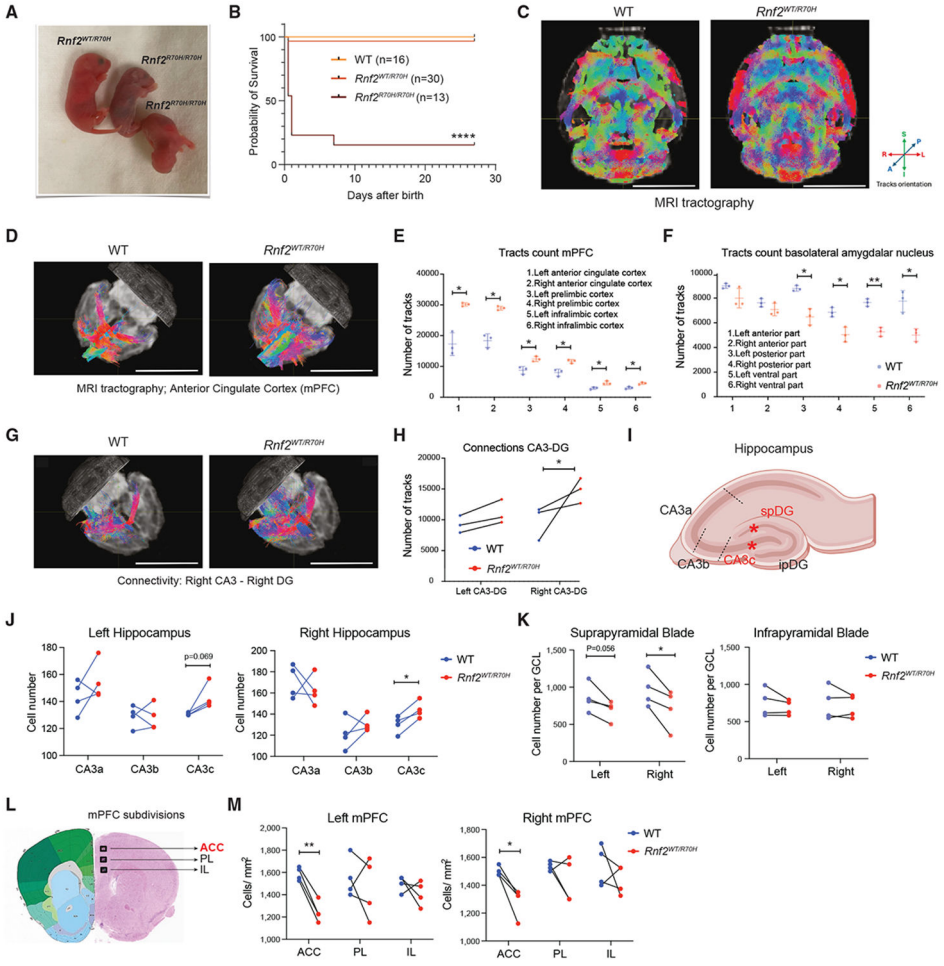

Figure 6. *Rnf2*$^{WT/R70H}$ mice display axonal disorganization and brain architecture deficits

(A) Representative pictures of *Rnf2*$^{WT/R70H}$ and *Rnf2*$^{R70H/R70H}$ mice.

(B) Probability of survival of *Rnf2*$^{WT/WT}$, *Rnf2*$^{WT/R70H}$, and *Rnf2*$^{R70H/R70H}$ mice. ****$p <$ 0.001. Log-rank Mantel-Cox test.

(C) Whole brain MRI tractography. Scale bar, 0.5 cm.

(D) Tractography of the mPFC. See Videos S1 and S2. Scale bar, 0.5 cm.

(E and F) Quantification of neuronal track projections from the subregions of the mPCF (E) and the basolateral amygdalar nucleus (F). *$p < 0.05$, **$p < 0.01$. Unpaired *t* test.

(G) Tractography of the connectivity between CA3 and DG. See Videos S5 and S6. Scale bar, 0.5 cm.

(H) Quantification of neuronal connections between CA3 and DG. *$p < 0.05$; paired *t* test.

(I) Model representing the connectivity defects in *Rnf2*$^{WT/R70H}$ mice. Asterisks represent changes in connectivity.

(J and K) Quantification of cells in the left and right CA3a-c regions of the hippocampus (J) and left and right suprapyramidal and infrapyramidal blades of the DG (K) . *$p < 0.05$; paired *t* test.

(L) Scheme of the mPFC subdivisions. AAC, anterior cingulate cortex; PL, prelimbic cortex; IL, infralimbic cortex.

(M) Quantification of cells in the left and right AAC, PL, and IL regions of the mPFC. *$p <$ 0.05, **$p < 0.01$. Paired t test. Results from (B) to (M) are from three $Rnf2^{WT/WT}$ and three $Rnf2^{WT/R70H}$ mice.

See also Figure S7, Tables S2 and S3, and Videos S1, S2, S3, S4, S5, and S6.

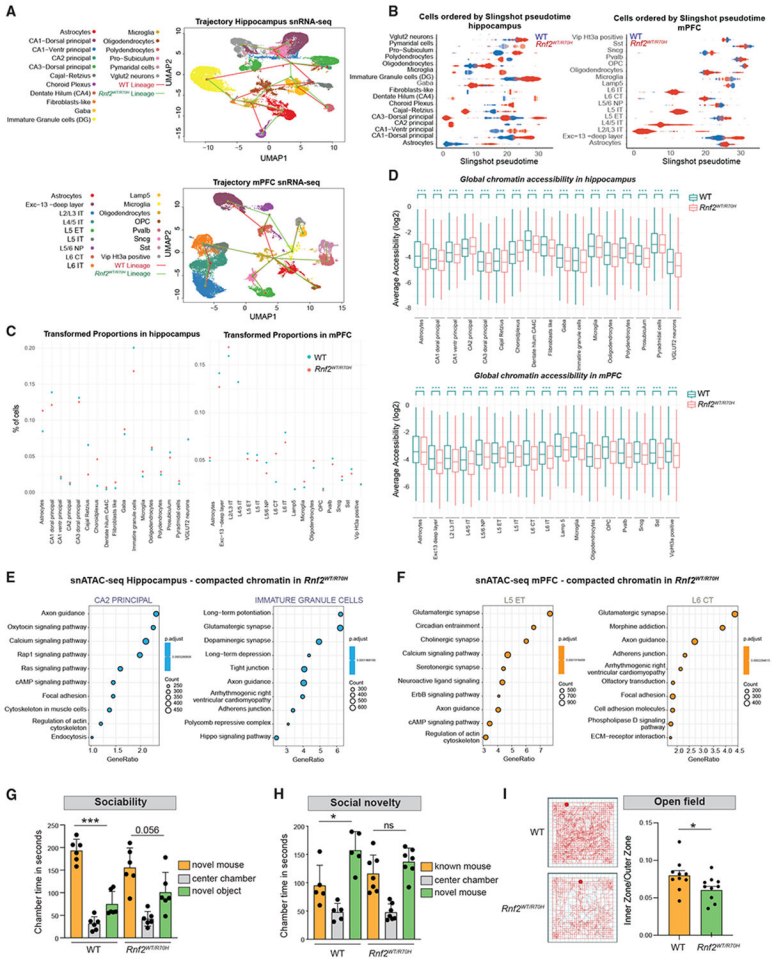

Figure 7. Ring1b^{R70H} imposes cell-type-selective chromatin compaction, stalls hippocampal and mPFC excitatory maturation, and impairs sociability with increased anxiety

(A) UMAP of snRNA-seq from hippocampus (top) and mPFC (bottom) colored by annotated cell types. Slingshot lineage curves are overlaid for each genotype to summarize inferred developmental flows across clusters.

(B) Distribution of cells from each annotated cell type along Slingshot pseudotime.

(C) Linearized and variance-stabilized proportions of clusters by logit transformation in WT and *Rnf2*$^{WT/R70H}$ hippocampus and mPFC.

(D) Global chromatin accessibility from each annotated cell type in WT and *Rnf2*$^{WT/R70H}$ hippocampus and mPFC by snATAC-seq.

(E and F) KEGG analysis inferred by changes in snATAC-seq between WT and *Rnf2*$^{WT/R70H}$ of selected cell types in hippocampus (E) and mPFC (F).

(G and H) Sociability (G) and social novelty (H) tests for WT and a *Rnf2*$^{WT/R70H}$. $*p < 0.05$, $***p < 0.01$. Bars represent mean ± SEM. $n = 7$.

(I) Open-field test. Individual measurements are depicted as black circles. Representative activity patterns (left) in the open-field test for WT and *Rnf2*$^{WT/R70H}$ mice. $*p < 0.05$. Bars represent mean ± SEM. $n = 10$.

See also Figure S8.

KEY RESOURCES TABLE

REAGENT or RESOURCE	SOURCE	IDENTIFIER
Antibodies		
H3K27me3 (ChIP-seq, CUT&RUN, WB)	Active Motif	Cat# 39155, RRID:AB_2461020
H2AK119ub (ChIP-seq, CUT&RUN, WB)	Thermo Fisher Scientific	Cat# 720148, RRID:AB_2605927
Ring1b (ChIP-seq)	Cell Signaling Technology	Cat# 5694, RRID:AB_10705604
CBX7 (ChIP-seq)	Abcam	Cat# ab21873, RRID:AB_726005
RYBP (ChIP-seq, WB)	EMD Millipore	Cat# AB3637, RRID:AB_2285466
MTF2 Polyclonal antibody (ChIP-seq)	PROTEINTECH	Cat# 16208-1-AP, RRID:AB_2147370
JARID2 (D6M9X) (ChIP-seq)	Cell Signaling Technology	Cat# 13594, RRID:AB_2798269
PHC1 (1F3F3) (WB)	Cell Signaling Technology	Cat# 13768, RRID:AB_2716803
Vinculin (WB)	Sigma-Aldrich	Cat# V9131, RRID:AB_477629
Ezh2 (WB)	Cell Signaling Technology	Cat# 16098, RRID:AB_3675772
HA-tag (WB)	Cell Signaling Technology	Cat# 3724, RRID:AB_1549585
H2A (WB)	Abcam	Cat# ab18255, RRID:AB_470265
H3 (WB)	Abcam	Cat# ab1791, RRID:AB_302613
RING1A (WB)	Cell Signaling Technology	Cat# 2820, RRID:AB_2177962
RING1B (WB)	MBL	Cat# D139-3, RRID:AB_592650
CBX4 (WB)	Cell Signaling	Cat# 30559, RRID:AB_2798991
Pcgf2 (WB)	Santa Cruz	Cat# sc-390868X
Oct3/4 (WB)	Santa Cruz	sc-5279, RRID:AB_628051
PAX6 (WB)	Thermo Fisher SCIENTIFIC	Cat# MA1-109, RRID:AB_2536820
Actin (WB)	Sigma-Aldrich	Cat# A2066
Secondary antibody_IRDye 800CW donkey anti-mouse IgG (WB)	LI-COR	Cat# 926-32212, RRID:AB_621847
Secondary antibody_IRDye 800CW donkey anti-rabbit IgG (WB)	LI-COR	Cat# 926-32213, RRID:AB_621848
Secondary antibody : HRP-conjugated goat anti-rabbit IgG	Cell Signaling Technology	Cat# 7074, RRID:AB_2099233
HA-Tag (CUT&RUN)	EpiCypher	Cat# 13-2010, RRID:AB_3094663
Flag (DYKDDDDK-Tag) (CUT&RUN)	EpiCypher	Cat# 13-2031
H3K27me3 (CUT&RUN)	EpiCypher	Cat# 13-0055, RRID:AB_3665059
IgG (CUT&RUN)	EpiCypher	Cat# 13-0042, RRID:AB_2923178
Iba1 (IF)	Invitrogen	Cat# GTX632426, RRID:AB_2888314
Map2 (IF)	Cell Signaling Technology	Cat# 8707, RRID:AB_2722660
secondary antibody (IF)	Invitrogen	Cat# A-11012
secondary antibody (IF)	Invitrogen	Cat# A-11001
Anti-FLAG® [M2] (IP)	Sigma-Aldrich	Cat# F3165, RRID:AB_259529
Bacterial and virus strains		
Stellar™ Competent Cells	Takara	636766
Chemicals, peptides, and recombinant proteins		
(Z)-4-Hydroxytamoxifen-5mg	Sigma-Aldrich	H7904
Puromycin 1μg/ml	Biogems	5855822

REAGENT or RESOURCE	SOURCE	IDENTIFIER
Penicillin/Streptomycin (10,000 U/ml)	Thermo Fisher Scientific	15140-122
PureFection-Transfection Reagent	System Biosciences, SBI	LV750A-5
0.1% gelatin	Millipore	ES-006-B
DMP Dimethyl pimelimidate dihydrochloride	Sigma-Aldrich	SIALD8388-250MG
Dynabeads™ Protein G for Immunoprecipitation	Thermo Fisher SCIENTIFIC	10004D
ESGRO® Recombinant Mouse LIF Protein	Sigma-Aldrich	ESG1107
Mirdametinib (PD0325901)	Sigma-Aldrich	HY-10254
CHIR99021	Selleckchem	5mg -S1263
ChIP Cross Link Gold	Diagenode	C01019027
B-27™ Supplement (50X), serum free	Thermo Fisher SCIENTIFIC	17504044
B27 minus insulin	Gibco	A1895601
MEM Non-Essential Amino Acids Solution (100X)	Thermo Fisher SCIENTIFIC	11140050
Human/Mouse Recombinant Activin A, ACF	STEMCELL Technologies	78132.1
2-Mercaptoethanol, 99%, pure	Thermo Fisher SCIENTIFIC	125470100
Protease Inhibitors	Thermo Fisher SCIENTIFIC	A32965 #ZC4200412
GSK343 (PRC2 inhibitor)	Sigma-Aldrich	SML0766
ERCC spike-in Mix 1	Thermo Fisher	4456740
TRIzol reagent	Thermo Fisher SCIENTIFIC	15596018
Bradford	Bio-Rad	5000006
Critical commercial assays		
CUTANA™ ChIC/CUT&RUN Kit - 48 Reactions	EpiCypher	14-1048
CUTANA™ CUT&RUN Library Prep Kit - 48 Reactions (Primer Set 1)	EpiCypher	14-1001
NEBNext® Ultra™ II DNA Library Prep Kit for Illumina®	NEB	E7645L
NEBNext® Multiplex Oligos for Illumina® (96 Unique Dual Index Primer Pairs Set 4)	NEB	E6446S NEB
HiScribe® T7 Quick High Yield RNA Synthesis Kit	NEB	E2050L
QIAquick PCR Purification Kit (50)	Qiagen	28106
Illumina TruSeq Stranded Total RNA Library Prep Gold	Illumina	20020598
TruSeq RNA UD Indexes	Illumina	20022371
Rna Miniprep Kit Direct-Zol 50preps	ZYMO RESEARCH	76020-642
RevertAid First Strand cDNA Synthesis Kit	Thermo Fisher SCIENTIFIC	K1622
iTaq Universal SYBR Greeen Supermix	BIO-RAD LABORATORIES, INC	1725124
Vector Red Substrate Kit, Alkaline Phosphatase	Vector Laboratories, Inc.	SK-5100
Deposited data		
RNA-seq	This paper	GSE286287
ChIP seq	This paper	GSE286289
ATAC seq	This paper	GSE286288
Cut&RUN	This paper	GSE286290
scRNA-seq	This paper	GSE286294
10x Multiome	This paper	GSE286294
Mass spectrometry	This paper	PXD059191

REAGENT or RESOURCE	SOURCE	IDENTIFIER
Experimental models: Cell lines		
HEK293T	ATCC	CRL-3216
HEK293T dKO RING1A/B	Laboratory of Dr. Moazed	N/A
Ring1A−/−; Ring1B fl/fl; Rosa26::CreERT2	Laboratory of Haruhiko Koseki	N/A
Ring1A−/−; Ring1B fl/fl; Rosa26::CreERT2 + Ring1b WT	This paper	N/A
Ring1A−/−; Ring1B fl/fl; Rosa26::CreERT2 + Ring1b R70H	This paper	N/A
Ring1A−/−; Ring1B fl/fl; Rosa26::CreERT2 + Ring1b I54A/D56K	This paper	N/A
ESC-Rnf2$^{WT/WT}$	This paper. Ingenious Targeting Laboratory	N/A
ESC-Rnf2$^{WT/R70H}$	This paper. Ingenious Targeting Laboratory	N/A
ESC/NPC-Rnf2$^{WT/WT}$ Pcgf2-WT and Pcgf2-KO	This paper	N/A
ESC/NPC-Rnf2$^{WT/R70H}$ Pcgf2-WT and Pcgf2-KO	This paper	N/A
ESC-Rnf2$^{WT/R70H}$_HA-Pcgf2-WT and HA-Pcgf2-ΔIDR	This paper	N/A
LP 129/SvEv x C57BL/6 hybrid embryonic stem cells (HF4)	Ingenious Targeting Laboratory	N/A
Rnf2HA-WT/FLAG-WT -Clone1_ WT allele1-3xHA/ WT allele2-3xFLAG	This paper	N/A
Rnf2HA-WT/FLAG-WT -Clone2_ WT allele1-3xHA/ WT allele2-3xFLAG	This paper	N/A
Rnf2WT/R70H _Clone 1_ mutant allele1-3xHA/ WT allele2-3xFLAG	This paper	N/A
Rnf2WT/R70H _Clone 2_ mutant allele1-3xHA/ WT allele2-3xFLAG	This paper	N/A
Experimental models: Organisms/strains		
C57BL/6N mice	Ingenious Targeting Laboratory	N/A
C. elegans strain: N2 var. Bristol: N2_WT	Stem Cells and Regenerative Medicine Center	CGC
C. elegans strain: SBP74: spat-3(mgw26)	Stem Cells and Regenerative Medicine Center	CGC
C. elegans strain: SK4013: tph-1p::GFP	Stem Cells and Regenerative Medicine Center	CGC
C. elegans strain: ALS668: spat-3::3xHA	Stem Cells and Regenerative Medicine Center	This study; CRISPR editing of N2 to insert C- terminal 2xTEV, AID,Bio, and 3xHA tags. The last intron is replaced with a synthetic intron containing a loxP site.
C. elegans strain: ALS759: tph-1p::GFP; spat-3::3xHA	Stem Cells and Regenerative Medicine Center	Mating of SK4013 (CGC) with ALS668
C. elegans strain: ALS841: tph-1p::GFP; spat-3 [R181H] ::3xHA	Stem Cells and Regenerative Medicine Center	This study; Co-CRISPR editing of ALS759
Oligonucleotides		
Pou5f1_FWD_5'-GAGGAGTCCCAGGACATGAA-3'	Sigma-Aldrich	N/A
Pou5f1-REV_5'-AGATGGTGGTCTGGCTGAAC-3'	Sigma-Aldrich	N/A
Nanog_FWD_5'-AGGCTGATTTGGTTGGTGTC-3'	Sigma-Aldrich	N/A
Nanog _REV_5'-CCAGGAAGACCCACACTCAT-3'	Sigma-Aldrich	N/A
GATA4_FWD_5'-CACAAGATGAACGGCATCAACC-3'	Sigma-Aldrich	N/A
GATA4_REV_5'-CAGCGTGGTGGTGGTAGTCTG-3'	Sigma-Aldrich	N/A

REAGENT or RESOURCE	SOURCE	IDENTIFIER
GATA6_FWD_5'-GAACGTACCACCACCACCAT-3'	Sigma-Aldrich	N/A
GATA6_REV_5'-CCATGTAGGGCGAGTAGGTC-3'	Sigma-Aldrich	N/A
Sox17_FWD_5'- CCGAGATGGGTCTTCCCTAC-3'	Sigma-Aldrich	N/A
Sox17_REV_5'-CGTCAAATGTCGGGGTAGTT-3'	Sigma-Aldrich	N/A
Esrrb_FWD_5'-GGCGTTCTTCAAGAGAACCA-3'	Sigma-Aldrich	N/A
Esrrb_REV_5'-TCCGTTTGGTGATCTCACAT-3'	Sigma-Aldrich	N/A
foxa2_FWD_5'-GACATACCGACGCAGCTACA -3′	Sigma-Aldrich	N/A
foxa2_REV_5'-GGCACCTTGAGAAAGCAGTC-3'	Sigma-Aldrich	N/A
nrp1_FWD_5'-GGAGCTACTGGGCTGTGAAG-3'	Sigma-Aldrich	N/A
nrp1_REV_5'-ACCGTATGTCGGGAACTCTG-3'	Sigma-Aldrich	N/A
Pax6_FWD_5'- CTGAGGAACCAGAGAAGACAGG-3'	Sigma-Aldrich	N/A
Pax6_REV_5'- CATGGAACCTGATGTGAAGGAGG-3'	Sigma-Aldrich	N/A
Tubb3-FWD_5'- CATCAGCGATGAGCACGGCATA-3'	Sigma-Aldrich	N/A
Tubb3-REV_5'- GGTTCCAAGTCCACCAGAATGG-3'	Sigma-Aldrich	N/A
Map2-FWD_5'- GCTGTAGCAGTCCTGAAAGGTG-3'	Sigma-Aldrich	N/A
Map2-REV_5'- CTTCCTCCACTGTGGCTGTTTG-3'	Sigma-Aldrich	N/A
Chat1-FWD_5'-GCTTGAATGGAGCGAATCGTTGG-3'	Sigma-Aldrich	N/A
Chat1-REV_5'-CACCAGGACGATGCCATCAAAAG-3'	Sigma-Aldrich	N/A
Ncam1-FWD_5'-GGTTCCGAGATGGTCAGTTGCT-3'	Sigma-Aldrich	N/A
Ncam1-REV_5'-CAAGGACTCCTGTCCAATACGG-3'	Sigma-Aldrich	N/A
DCX-FWD_5'-CTGACTCAGGTAACGACCAAGAC-3'	Sigma-Aldrich	N/A
DCX-REV_5'-TTCCAGGGCTTGTGGGTGTAGA-3'	Sigma-Aldrich	N/A
NeuN-FWD_5'-GAGGAGTGGCCCGTTCTG-3'	Sigma-Aldrich	N/A
NeuN-REV_5'-AGGCGGAGGAGGGTACTG-3'	Sigma-Aldrich	N/A
Ngn2_FWD_5'-TCAGGAGGGAGGATTGCTT-3'	Sigma-Aldrich	N/A
Ngn2_REV_5'- GAAACACGTGTGTGGCTGA-3'	Sigma-Aldrich	N/A
qA1_5′ -GAGGTCTCTCTGGTCTGCTCTAGC-3′	Sigma-Aldrich	N/A
RNEOGT_5′ GAAAGTATAGGAACTTCGCGACACGGAC-3′	Sigma-Aldrich	N/A
NEOGT_5′ -GTCCGTGTCGCGAAGTTCCTATACTTTC-3′	Sigma-Aldrich	N/A
SQ1_5′ -GACAGGTAGGACACTCTTTGTTGC-3′	Sigma-Aldrich	N/A
SC1_5′ -TGAACATGGCGACTTGGGTG-3′	Sigma-Aldrich	N/A
sgPCGF2_FW1_5'CACCGCACCTCATGTGTG-3'	Azenta Life Sciences	N/A
sgPCGF2_REV1_5'AAACCAGAGGGCACACATGAGGTGC-3'	Azenta Life Sciences	N/A
sgPCGF2_FW1_5'CACCGCTCCGTGATTTTAATCCGTG-3'	Azenta Life Sciences	N/A
sgPCGF2_REV2_5'AAACCACGGATTAAAATCACGGAGC-3'	Azenta Life Sciences	N/A
spat3-sgRNA-intron18_ TTCTAATACGACTCACTATAGTGGAATTCAATTGAT GTGTCGTTTTAGAGCTAGAAATAG (protospacer in bold)	Stem Cells and Regenerative Medicine Center	N/A
spat3-sgRNA-UTR_ TTCTAATACGACTCACTATAGCACCTCATAATTCACA TAAGGTTTTAGAGCTAGAAATAG (protospacer in bold)	Stem Cells and Regenerative Medicine Center	N/A

REAGENT or RESOURCE	SOURCE	IDENTIFIER
sgRNA-universal- reverse-primer_ AAAAGCACCGACTCG	Stem Cells and Regenerative Medicine Center	N/A
SPAT-3exon4sgRNA-FWD_ TTCTAATACGACTCACTATAGTAAACGCCACAAGAATA CACGTTTTAGAGCTAGAAATAG (protospacer in bold)	Stem Cells and Regenerative Medicine Center	N/A
dpy-10sgRNA-forward- primer_ TTCTAATACGACTCACTATAGGCTACCATAGGCACCAC GAGGTTTTAGAGCTAGAAATAG (protospacer in bold)	Stem Cells and Regenerative Medicine Center	N/A
Rnf2-FWD: 5'-CTGTGCAGACAAATGGAACT-3'	Sigma-Aldrich	N/A
Puro-RVS: 5'-GCGCGCTCGGCCGCCTCCAC-3'	Sigma-Aldrich	N/A
EGFP-RVS: 5'-TCGTCCATGCCGAGAGTGATC-3'	Sigma-Aldrich	N/A
Recombinant DNA		
pPB[Exp]-EF1A>EGFP/Puro_RING1B_WT	This paper	VectorBuilder
pPB[Exp]-EF1A>EGFP/Puro_RING1B_R70H	This paper	VectorBuilder
pPB[Exp]-EF1A>EGFP/Puro_RING1B_I53A/D56K	This paper	VectorBuilder
pPB[Exp]-EF1A>EGFP/Puro CTRL	This paper	VectorBuilder
pPB[Exp]-EF1A> CAG>EGFP:T2A:Puro_mPcgf2	This paper	VectorBuilder
pPB[Exp]-EF1A> CAG>EGFP:T2A:Puro_mPcgf2(1-239aa)	This paper	VectorBuilder
lentiCRISPR v2	Addgene	#52961
PB-MSCV-MCS-EF1α-GreenPuro cDNA	System Biosciences, SBI	PB713B-1
PX458-Rnf2-sgRNA (ACTTTATTATGCACCCACCA)	This paper	N/A
pU6::klp-12_sgRNA plasmid	Addgene	4617096
pBluescript II-3X FLAG-EGFP	GenScript Biotech	N/A
pBluescript II-3X HA-Puromycin	GenScript Biotech	N/A
PiggyBac transposase vector	System Biosciences, SBI	PB210PA-1
Software and algorithms		
AlphaFold2	Jumper et al.[83]	https://alphafold.ebi.ac.uk/download
AlphaFold3	Abramson et al.[84]	https://alphafold.ebi.ac.uk/download
ColabFold	Mirdita et al.[85]	https://github.com/sokrypton/ColabFold
MutaBind2	Zhang et al.[86]	https://mutabind.org/
nf-core Pipelines	Ewels et al.[87]	https://nf-co.re
R	N/A	www.r-project.org
Rstudio server	Posit	https://posit.co/products/open-source/rstudio-server/
GNU parallel	Free Software Foundation	https://www.gnu.org/software/parallel/
deepTools	Ramírez et al.[88]	https://deeptools.readthedocs.io
Encode Pipelines	N/A	https://www.encodeproject.org/
SAMtools	Li et al.[89]	https://www.htslib.org/
PyMol	PyMOL by Schrödinger	https://www.pymol.org/
MultiQC	Ewels et al.[90]	https://github.com/MultiQC/MultiQC
FASTQC	N/A	https://www.bioinformatics.babraham.ac.uk/projects/fastqc/

REAGENT or RESOURCE	SOURCE	IDENTIFIER
Bowtie2	Langmead et al.[91]	https://bowtie-bio.sourceforge.net/bowtie2/index.shtml
Kent tools	UCSC	https://github.com/ucscGenomeBrowser/kent
Ggsignif	N/A	https://const-ae.github.io/ggsignif/
Ggprism	N/A	https://csdaw.github.io/ggprism/
HOMER	N/A	http://homer.ucsd.edu/homer/motif/
ClusterProfiler	Xu et al.[92]	https://bioconductor.org/packages/release/bioc/html/clusterProfiler.html
Pheatmap	N/A	https://cran.r-project.org/web/packages/pheatmap/pheatmap.pdf
Ggplot2	N/A	https://ggplot2.tidyverse.org/
bedtools	Quinlan and Hall.[93]	https://bedtools.readthedocs.io/en/latest/
Seurat	Satija et al.[94]	https://satijalab.org/seurat/
Signac	Stuart et al.[95]	https://stuartlab.org/signac/
BioRender	BioRender	https://www.biorender.com/